ABSTRACT

Title of Document: MODELING AND OPTIMIZATION OF
                            MICROGRID ENERGY SYSTEM FOR SHIP
                            APPLICATIONS

                            Tao Cao, Doctor of Philosophy, 2016

Directed by: Reinhard Radermacher, Professor
                            Department of Mechanical Engineering

Microgrid energy systems are widely used in remote communities and off-grid sites, where primary energy supplies are dominated by fuels. Limited attentions have been paid to ship applications, which require thorough and in-depth research to address their unique challenges and increasing pressure on reducing fuel consumptions. This dissertation presents comprehensive microgrid system studies for ship applications in four aspects: component modeling and study, dynamic system modeling on novel designs, novel optimization based system design framework development and investigations on two enhancement options: integrating with separate sensible and latent cooling systems, maximizing heat recovery through pinch analysis.

Comprehensive component studies consist of new component models addressing unique features of ship applications. Desiccant wheels with new materials were investigated experimentally, especially under high humidity conditions for ship applications. Dynamic system modeling was conducted on several novel solar energy and waste heat powered systems, with a focus on their capabilities to reduce fuel consumptions and CO_2 emissions. Results were validated against experimental data. Payload and economic studies were conducted to evaluate feasibilities of applying the designs to ship applications. A novel optimization based design framework was then

developed. The framework is capable of conducting both system configuration and control strategy optimization under transient weather and load profiles, differentiating itself with current control strategy focused energy system optimization studies (Jradi and Riffat, 2014). It also extends Buoro et al. (2012)'s study on system configuration optimization to complete design from scratch with comprehensive equipment selections and integrating options. The design framework was demonstrated through a case study on container ships. Optimized systems and control strategies were found from three different scenarios: single-objective optimization, bi-objective optimization and optimization under uncertainty. Finally, two previously listed options were investigated to enhance microgrid system performance regarding thermal comfort and fuel savings.

This research fills current research gaps on microgrid energy system for ship applications. It also serves as the basis for advanced microgrid system analysis framework for any applications. The dynamic system modeling platform, optimization based design framework and enhancement methods can help engineers develop and evaluate ultra-high efficiency designs, aiming to reduce energy consumptions and CO_2 emissions.

MODELING AND OPTIMIZATION OF MICROGRID ENERGY SYSTEM FOR SHIP APPLICATIONS

By

Tao Cao

Dissertation submitted to the Faculty of the Graduate School of the
University of Maryland, College Park, in partial fulfillment
of the requirements for the degree of
Doctor of Philosophy
2016

Advisory Committee:
 Dr. Reinhard Radermacher (Chair/Advisor)
 Dr. Peter Sunderland
 Dr. Jelena Srebric
 Dr. Steven Gabriel
 Dr. Marino diMarzo
 Dr. Yunho Hwang

Acknowledgements

At the end, I would like to thank my parents and brother for their encouragements and tender care during my Ph.D. study. This thesis would not be completed without their generous love and patience.

Table of Contents

List of Figures

List of Tables

1 Introduction

1.1 Background and Motivation

Microgrid system refers to energy system capable of balancing captive supply and demands resources to maintain stable service within a defined boundary. Microgrid systems are defined by their functions, rather than sizes. Applications of microgrid systems cover off-grid applications such as islands and ships, community micro-grids such as universities and military bases and nano-grids such as buildings. Typically, microgrid systems need independent power generation units as supplement electricity suppliers other than the grid. For off-grid applications, power generator units are the only electricity suppliers. Traditionally these power generation units are fossil fuels powered, which bring cost and environmental concerns. There have been increasing research efforts to address high fossil fuel dependence of microgrid systems. The most popular approach is to utilize onsite renewable energy (mostly solar energy) or waste heat energy.

One microgrid system application area that hasn't receive enough attentions are ship applications. Unlike power plants and buildings which are mainly recent research focuses, ship applications have several unique features as follows:

- No grid electricity supply

- Weather conditions vary along sea routes and are usually in extremely high humidity conditions

- Free sea water as "cooling source"

- Constant waste heat supply from main engine

- Constraints on system weight and volume imposed by ship payload

- Various energy demands for different ships

- Loading and unloading of containers

- Fresh water demands and availability

The typical onboard power generation system consists of two sub-systems. One is a diesel engine for propulsion and the other is a diesel generator for other electricity usage. These diesel combustion systems have caused both economic and environmental concerns. The diesel combustion could produce a large amount of pollutants like SO_x and NO_x. Moreover, diesel fuels used in ships – the so called "bunker fuel" produces more SO_x than the road diesel fuel during combustion process [1]. Strict laws and regulations have been imposed to address the emission issue, both globally and regionally. The International Maritime Organization (IMO) is the major global organization working on ship emission regulations. The International Convention for the Prevention of Pollution from Ships (MARPOL) is the main internal convention covering prevention of pollution of the marine environment by ships from operational or accidental causes [2]. The European Union has implemented regional level regulations in the form of SO_x emission control areas (SECAs), where the maximum sulfur level in marine fuels is set to be at 1.5%, about one third of the maximum level stipulated by MARPOL. However, the global warming emission issue in marine sector has not been addressed in regulations yet. According to the IMO report [3], shipping contributed 3.3% of global CO_2 emission. If no further actions are taken, it is estimated that shipping greenhouse gas emissions could increase by up to 250% by 2050. Besides, with decreasing availability and increasing prices of fossil fuels, the economic

concern rises. Therefore, reducing the onboard fuel consumption and emission become priority research objectives in ship applications. The propulsion is the largest onboard energy consumer. Although the diesel engine efficiency, which typically ranges from 48 to 51%, has been improved significantly over the past decades, it has reached a mature stage and further improvements are hard to achieve [4].

1.2 Literature Review

1.2.1 Energy Conversion Options

Microgrid systems consist of various equipment to meet different energy demands, mostly cooling, heating and power. For traditional system designs, such equipment is usually electricity powered. However, the waste heat or renewable energy is mostly in the form of thermal energy rather than electricity. Therefore, it is necessary to have an overview on various thermally activated energy cycles.

Figure 1-1 compares thermally activated power cycles with applicable temperature range, cycle efficiency and development status. As the waste heat and renewable energy usually have various temperature levels, one may choose cycles corresponding to input temperatures. For low temperature heat inputs (<500°C), piezoelectric generation, organic Rankine cycle, trilateral flash cycle and Kalina cycle are available options. For medium temperature heat inputs (500-700°C), steam Rankine cycle and thermal electric generations are available. When heat inputs have temperatures higher than 700°C, thermal photovoltaic generation or thermionics are applicable. For most utilizable waste heat and solar heat, temperatures usually do not exceed 700°C. Indeed, thermionics or thermal photovoltaic

3

generations are mostly used in space applications, rather than ground heat conversion cycles.

For low temperature applications, piezoelectric generation is still under laboratory prototype development and has rather low efficiency (<10%). The trilateral flash cycle is still under concept development, though claimed with a higher efficiency than organic Rankine cycle. Organic Rankine cycle and Kalina cycle are successfully demonstrated with low temperature heat inputs. Medium temperature could be reached either by thermoelectric or steam Rankine cycle. The steam Rankine cycle is more developed and has higher efficiency.
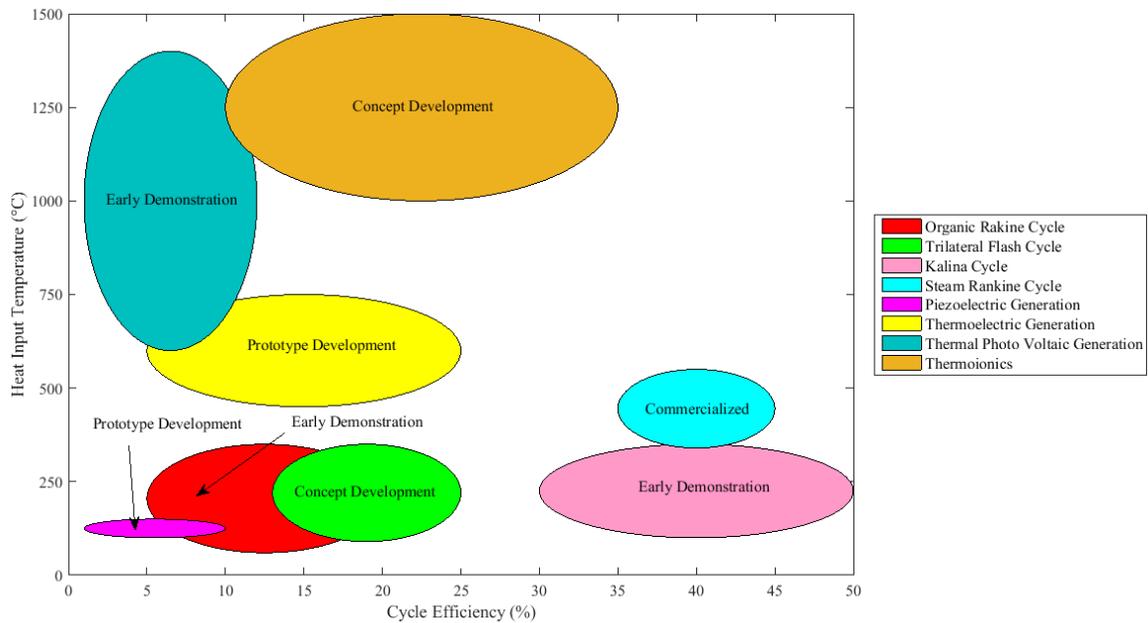
Figure 1-1: Comparison of thermally activated power cycles

Figure 1-2 compares thermally activated cooling cycles with required heat input temperatures, cooling output temperatures and COP ranges. It is observed that NH_3/H_2O absorption cycles are suitable for deep refrigeration demands, while $H_2O/LiBr$ absorption, adsorption and ejector cooling systems are applicable for space cooling. Liquid and solid

desiccant systems are designed for air dehumidification and they are usually coupled with other cooling systems for better dehumidification and cooling. Another interesting point is that most of the cooling cycles has a COP less than 1, with exceptions for multi-effect absorption cycles. However, multi-effect cycles are rarely seen in real applications due to their complexities and cost. One may also note that most of thermally activated cooling cycles listed here are able to utilize low temperature heat inputs, ranging from 60 to 220°C. Such temperature range is even lower than heat input requirements for some low temperature heat power cycles. Hence it is possible to use the same heat for power cycles first and then cooling cycles. Cascaded usage of heat allows better heat recovery efficiency.
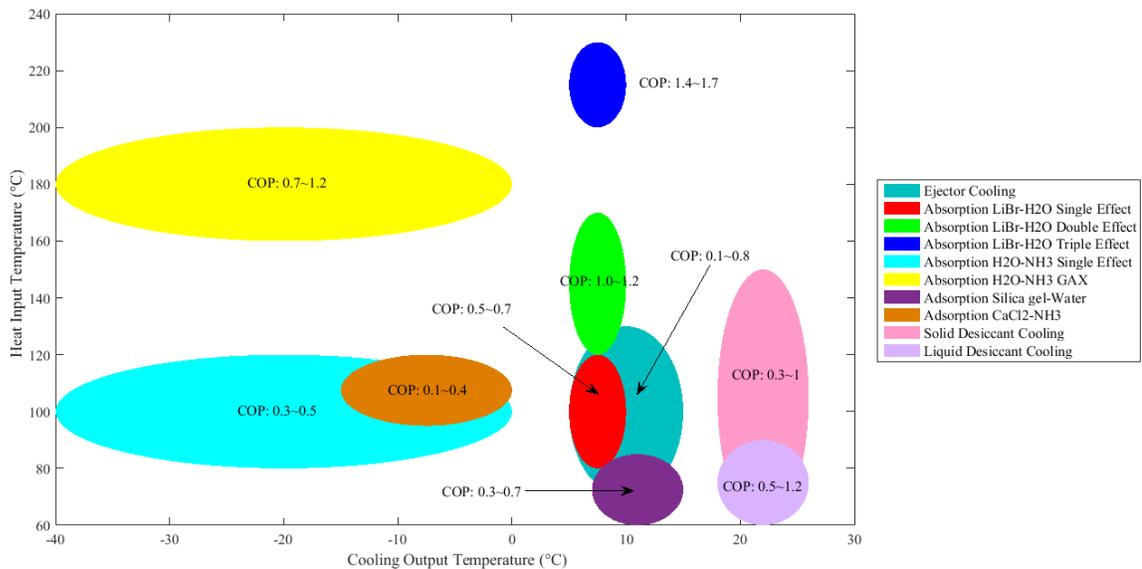
Figure 1-2: Comparison of thermally activated cooling cycles

Thermally activated heating systems are rather straightforward in theory, as compared with thermally activated cooling and power systems. Usually thermal energy can be used for space heating or water heating directly through various economizers. Alternatively, thermal energy can be upgraded to higher temperatures for industrial process

heating or space and water heating through heat pumps. It is necessary to note that different heat pumps have limitations on maximum sink temperatures and temperature lifts as summarized in Table 1-1.

Table 1-1: Comparison of heat pump temperature lifts and sink temperatures

Heat Pump Type	Maximum Sink Temperature (°C)	Maximum Temperature Lift (°C)
Electric Motor Closed Compression Cycle	120	80
Diesel Motor Closed Compression Cycle	130	90
Mechanical Vapor Recompression	190	90
Thermal Vapor Recompression	150	40
Absorption Cycle (Type I, Heat Pump)	100	50
Absorption Cycle (Type II, Heat Transformer)	150	60

1.2.2 Recent Studies on Microgrid Systems

The heating, ventilation and air conditioning (HVAC) system is usually the second largest power consumer for ship applications. Traditionally the power supply for cooling systems relies on electricity from diesel generators. There has been growing research interest in innovating the shipboard cooling system to reduce the electricity demands. A valuable and popular approach is to capture and reclaim the waste heat source, which could be used to power up shipboard cooling, heating and power systems. The onboard waste heat sources usually come with large quantities and constant supplies [5], thereby provides a substantial amount of energy. Study shows for a typical two-stroke diesel engine used in ship applications, 50.7% of energy in the fuel is wasted in the form of low and medium grade heat [6]. The recoverable waste heat sources (47.2%) are usually from the air cooler (130 to 150°C), exhaust gas (250 to 500°C), and jacket water (70 to 120°C) [4].

The waste heat could be used for fuel/air processing, power generation, desalination and HVAC systems [7]. Especially for space cooling systems, Fernandez et al. (1998)

6

proposed and simulated a gas-to-thermal fluid heat recovery system from engine exhausts in a trawler chiller fishing vessel to power an absorption plant for onboard cooling production [8]. Optimum thermal operating conditions were determined based on modeling results. Wang et al. (2004) conducted experimental study of an onboard adsorption ice maker [9]. Three adsorbents were tested and compared. The best COP was reported as 0.125. Little and Garimella (2011) compared two cooling approaches powered by waste heat – absorption and vapor compression [7]. The authors concluded that absorption cooling may be preferred, especially when liquid coupling can be used. Garimella et al. (2011) proposed a waste heat driven absorption/vapor compression cascade refrigeration system for navy ships [10]. The system was modeled with Engineering Equation Solver (EES). The system had a reported COP of 0.6 and consumes 31% less electricity compared with an equivalent two-stage VCC. Liang et al. (2013) simulated an electricity-cooling cogeneration system with EES [11]. The system is a combination of Rankine cycle and absorption cycle. It was reported the useful output of the whole system was increased by 9% by adding the absorption cycle. Quadha and El-Gotni (2013) studied an ammonia/water absorption refrigeration system with marine diesel engine [12]. All components were analyzed with the first law of thermodynamics. There also have been studies on shipboard cooling generations using waste heat from fuel cells, solar energy and power cycles [13 – 21].

Table 1-2 summarizes the recent studies on innovative shipboard cooling systems. The review focuses on engine waste heat powered shipboard space cooling systems. Most of the recent studies are limited to steady-state simulations, while the ambient conditions and cooling demands are transient in real operation. In addition, most studies are restricted

to simple model simulations. The control logic and detailed system design are not introduced.

Table 1-2: Summary of recent studies on innovative cooling systems

Researcher (Year)	Waste Heat Powered	Ship Application	Cooling System (Working Pair)	Approach
Little and Garimella (2011) [7]	Yes (Engine)	No	Absorption (NH_3/H_2O); VCC	Steady-state simulation
Fernandez-Seara et al. (1998) [8]	Yes (Engine)	Yes	Absorption (NH_3/H_2O)	Steady-state simulation
Wang et al. (2004) [9]	Yes (Engine)	Yes	Adsorption	Experiment
Garimella et al. (2011) [10]	Yes (Engine)	Yes	Absorption ($H_2O/LiBr$); VCC (CO_2)	Steady-state simulation
Liang et al. (2013) [11]	Yes (Engine)	Yes	Absorption (NH_3/H_2O)	Steady-state simulation
Quadha and El-Gotni (2013) [12]	Yes (Engine)	Yes	Absorption (NH_3/H_2O)	Steady-state simulation
Khan et al. (2010) [13]	Yes (Power Cycle)	No	Absorption (NH_3/H_2O)	Optimization
Mortazavi et al. (2010) [14]	Yes (Power Cycle)	No	Absorption ($H_2O/LiBr$)	Steady-state simulation
Tse et al. (2011) [15]	Yes (Fuel Cell)	Yes	Absorption ($H_2O/LiBr$ and NH_3/H_2O)	Steady-state simulation
Ghirardo et al. (2011) [16]	Yes (Fuel Cell)	Yes	Absorption ($H_2O/LiBr$ and NH_3/H_2O)	Steady-state simulation
Arsalis (2012) [17]	Yes (Fuel Cell)	Yes	Absorption ($H_2O/LiBr$ and NH_3/H_2O)	Steady-state simulation
Seyfouri and Ameri (2012) [18]	Yes (Power Cycle)	No	Absorption ($H_2O/LiBr$); VCC (R22)	Steady-state simulation
Gommed and Grossman (2012) [19]	Yes (Solar)	No	Liquid desiccant	Experiment
Calise et al. (2012) [20]	Yes (Solar)	No	Absorption ($H_2O/LiBr$)	Transient Simulation
Mohammadi and Ameri (2014) [21]	Yes (Power Cycle)	No	Absorption ($H_2O/LiBr$); VCC (R22)	Steady-state simulation

8

Reefer containers used in container ships have large refrigeration demands, which are usually implemented by integrated vapor compression cycle (VCC) reefer units. VCC reefer units consume large amount of electricity and cannot be replaced with heat activated cooling equipment as they are attached to each reefer container. An alternative solution is a cascaded absorption-compression cooling system. The chilled water generated from the absorption cycle (ABC) is employed as cooling sources for condensers of VCC reefer units. As such, the operating pressure of the VCC reefer unit condenser is much lower than using high temperature ambient air as heat sink. Lower condenser pressure leads to less electricity consumption of reefer units.

A number of studies on the cascaded cooling cycle have been conducted recently. Garimella et al. (2011) conducted theoretical analysis on a cascaded absorption-compression cycle for naval ship applications [22]. The cycle is combined of single effect H_2O/LiBr absorption cycle and a subcritical CO_2 VCC. The cycle can save up to 31% electricity compared to an equivalent vapor compression system. Seyfouri and Ameri (2012) investigated various cascaded configurations of a compression chiller and an absorption chiller powered by a micro turbine [23]. The most energy saving configuration is found to be the system using two-stage compression chiller with an intercooler between two compressors and a subcooler at condenser outlet. Mohammadi and Ameri (2014) compared different cooling strategies in a cascaded cooling cycle [24]. They found the system with water cooled chillers has the highest second law efficiency and water consumption. Jain et al. (2013) analyzed effects of various operating parameters on the performance of a cascaded cooling system [25]. They concluded that condenser and evaporator temperatures should be given special considerations to improve the system

performance. Horvath et al. (2014) conducted steady and transient simulations on a cascaded cooling system for off-grid applications [26]. The system showed a fuel saving of 34-37% as compared with combined heat and power only configuration. Sun (2008) conducted an experimental study on a cascaded cooling system [27]. The cooling capacity is about 596 kW and primary energy ratio (PER) reaches 1.84 at air-conditioning rated conditions. Cimsit and Ozturk (2012) studied the performance of a cascaded absorption-compression cycle with various working fluids [28]. They concluded the H_2O/LiBr pair improves the coefficient of performance (COP) by 33% as compared to the NH_3/H_2O pair. Kairouani and Nehdi (2006) analyzed a cascaded refrigeration system powered by geothermal energy [29]. The system improves the COP by 37-54% compared with a single stage refrigeration system. Fernandez et al. (2006) investigated a combined compression and absorption refrigeration system [30]. They focused on the adaptability between the power requirements of the refrigeration system and the power supplied by the cogeneration system. Wang et al. (2012) studied a solar assisted cascaded refrigeration system [31]. They found the COP of the cascade system increases as sunlight becomes intense.

Table 1-3 summarizes recent studies on cascaded absorption-compression cooling system. There are limited studies for the refrigerated container ship application, which requires low temperature refrigeration and space cooling at the same time. Also, most of the simulation studies are limited to steady state simulations. Besides, the unique feature of integrated VCC reefer units presents challenges for the cascaded system layout, as is discussed later.

Table 1-3: Recent studies on cascaded absorption-compression cooling systems

Researcher (Year)	Ship application	ABC working pair	VCC working pair	Integration	Study approach	Cooling effects
Garimella et al. (2011) [22]	Yes	H_2O/LiBr	CO_2	Evaporator-Condenser	Steady-state simulation	Space cooling; Electronics
Seyfouri and Ameri (2012) [23]	No	H_2O/LiBr	R22	Evaporator-Condenser; Subcooler; Intercooler	Steady-state simulation	Refrigeration
Mohammadi and Ameri (2014) [24]	No	H_2O/LiBr	R22	Evaporator-Evaporator	Steady-state simulation	Space cooling
Jain et al. (2013) [25]	No	H_2O/LiBr	R410A, R407C, R134a	Evaporator-Condenser	Steady-state simulation	Refrigeration
Horvath et al. (2014) [26]	No	H_2O/LiBr	R134a	Evaporator-Condenser	Transient simulation	Space cooling
Sun (2008) [27]	No	H_2O/LiBr	N/A	Evaporator-Evaporator	Experimental	Space cooling
Cimsit and Ozturk (2012) [28]	No	H_2O/LiBr; NH_3/H_2O	R134a, R410A, R717	Evaporator-Condenser	Steady-state simulation	Refrigeration
Kairouani and Nehdi (2006) [29]	No	NH_3/H_2O	R717, R22, R134a	Evaporator-Condenser	Steady-state simulation	Refrigeration
Fernandez et al. (2006) [30]	No	NH_3/H_2O	CO_2, R717	Evaporator-Condenser	Steady-state simulation	Refrigeration
Wang et al. (2012) [31]	No	H_2O/LiBr	R134a	Evaporator-Condenser	Steady-state simulation	Refrigeration

Energy system optimization is needed from design and operation points of view. From the design point of view, the optimized system configuration, as well as component capacities need to be determined. Once the system configuration and component capacities are finalized, optimized control strategies need to be found. There have been considerable optimization studies on energy systems, as listed in Table 1-4.

Usually energy system optimization problem involves discrete and nonlinear terms due to nonlinear equipment performance behaviors and on-off control signals. As such, the

problem usually belongs to mixed integer nonlinear programming (MINLP). Some complex problems may be even nonconvex. Evolutionary algorithms are proven to be one of the popular approaches to MINLP due to their applicability to any type of problems, particularly for nonconvex problems. Vikrant [32] conducted comprehensive design optimization of novel heat exchangers based on single and multi-response adaptive design of experiments. Manolas et al. [33] solved an optimization problem regarding energy supplies in process plants using genetic algorithm. The author focused on tuning genetic algorithm parameters to obtain optimal solutions. Wang et al. [34] conducted an optimization study on building cooling, heating and power systems using particle swarm algorithm, with a focus on maximizing energetic, economical and environmental benefits. Liu et al. [35] used enumeration algorithm to determine the optimal power generation unit capacity in a combined cooling, heating and power system.

Regarding optimization variables, most studies focused on optimizations of control strategies or equipment capacities with pre-defined system configurations. Only Buoro et al. [36] considered system configuration optimization. However, the study is limited to heating and power generations only. Besides, the author treated each combined heat and power system as an integrated unit. In practical design, the combined heat and power system still consists of many sub-components and has a variety of possible configurations.

Energy system optimization studies involve extensive cycle modeling. Cycle models could be thermodynamic based or correlation based. Thermodynamic based component models are usually quite complicated for comprehensive energy system optimizations. Therefore, they are limited to simple or well-studied system configurations, as those investigated by Sayyaadi [37] and Ghobeity et al. [38]. In contrast, correlation

12

based cycle models allow complex system optimizations though sacrificing accuracies, as studies conducted by Rong and Lahdelma [39].

Most studies were focused on cooling, heating and power generations in power plants and building applications. Recently advanced cycles in other applications have been considered. Esfahani and Yoo [40] conducted optimization studies on combined gas turbine power plants and reverse osmosis desalination systems. Wu et al. [41] investigated multi-stage flash and reverse osmosis desalination systems in an optimization study on water and power cogeneration in power plants. Table 1-4 summarizes recent optimization studies on energy systems.

Table 1-4: Optimization studies on microgrid energy systems

Author (Year)	Optimization Variable	Optimization Approach	Cycle Model Approach	Application
Manolas et al. (1997) [42]	Operation	Genetic algorithm	Thermodynamic model	Power plants
Toral et al. (2000) [43]	Operation	Sequential quadratic programming	Thermodynamic model	Power plants
Rong and Lahdelma (2005) [39]	Operation	Mixed integer linear programming	Correlations	Buildings
Mago and Chamra (2009) [44]	Operation	Mixed integer linear programming	Correlations	Buildings
Sayyaadi (2009) [37]	Operation	Multi-objective evolutionary algorithms	Thermodynamic model	Power plants
Wille-Haussmann (2010) [45]	Operation	Mixed integer linear programming	Correlations	Power plants
Wang et al. (2010) [46]	Operation; Sizing	Genetic algorithm	Correlations	Buildings
Wang et al. (2010) [47]	Operation; Sizing	Particle swarm optimization algorithm	Correlations	Buildings
Sayyaadi et al. (2011) [48]	Operation	Particle swarm optimization algorithm	Thermodynamic model	Power plants
Ghobeity et al. (2011) [38]	Operation	Sequential quadratic programming	Thermodynamic model	Power plants
Ortiga et al. (2011) [49]	Operation	Mixed integer linear programming	Correlations	Buildings
Wang et al. (2011) [50]	Operation	Genetic algorithm	Correlations	Buildings
Liu et al. (2012) [35]	Operation	Enumeration algorithm	Correlations	Buildings
Wu et al. (2012) [51]	Operation	Mixed integer nonlinear programming	Correlations	Power plants & buildings
Zare et al. (2012) [52]	Operation	Genetic algorithm	Thermodynamic model	Power plants
Esfahani (2013) [40]	Operation	Genetic algorithm	Thermodynamic model	Power plants & desalination
Liu et al. (2013) [53]	Operation	Sequential quadratic programming	Matrix model	Buildings
Wu et al. (2013) [41]	Operation	Mixed integer nonlinear programming	Correlations	Power plants & desalination
Wakui et al. (2014) [54]	Operation	Mixed integer linear programming	Correlations	Buildings
Soltani et al. (2014) [55]	Operation	Genetic algorithm	Thermodynamic model	Power plants
Wakui and Yokoyama (2014) [56]	Operation	Mixed integer linear programming	Correlations	Buildings
Buoro et al. (2014) [36]	Operation; Configuration	Mixed integer linear programming	Correlations	Industrial factories
Karaali and Ozturk (2015) [57]	Operation	Nonlinear simplex direct search method	Thermodynamic model	Power plants

1.3 Summary

Review of studies on microgrid systems reveals that there has been limited focus on ship applications. Particularly unique ship application features have not been addressed in a comprehensive microgrid system study. Previous studies are limited to preliminary level modeling. A dynamic and comprehensive microgrid system modeling work is able to address such unique features while enhance understandings of approaches to reduce system fuel consumptions through novel configuration designs.

Regarding microgrid system optimization, there lacks an optimization based design framework from scratch – optimizing both system configuration and control strategy. The configuration optimization consists of optimizing system layout and equipment sizing. The system layout optimization involves equipment selections based on available energy source and energy demands, as well as integration ways among all equipment. Optimizations on layout are perquisites for equipment sizing and control strategy optimizations. Unfortunately, it hasn't been fully studied in combination with control strategy optimizations. Most recent optimization studies focus on control strategies only.

Lastly, a couple of systems can be promising when integrated with current microgrid systems to enhance its performance and functionality for ship applications. For instance, integrating the separate sensible and latent cooling system to enhance thermal comfort control and fuel savings and maximizing internal heat recovery through pinch analysis. There hasn't been detailed evaluations on integrating these systems with current shipboard microgrid systems.

2 Research Objectives

2.1 Objectives

This research aims to provide a comprehensive investigation on microgrid energy systems for ship applications with four major objectives. The first objective focuses on component studies and developing detailed component models for universal ship applications:

- Develop energy conversion equipment models, addressing ship application features such as energy supply and design constraints

- Set up detailed ship models including main engines, living spaces and refrigerated containers (reefers)

- Develop a novel sea route weather model capable of modeling any sea route weather climates

- Investigate desiccant wheels with new materials experimentally, particularly under high humidity conditions for ship applications

The second objective focuses on dynamic system modeling. In particular, studies were focused on novel solar energy and waste heat energy powered microgrid systems:

- Propose novel solar and waste heat powered microgrid systems for different types of ships

- Perform dynamic modeling of proposed systems using developed component models under various sea route climates

- Validate dynamic modeling results with experimental data

- Conduct comprehensive control strategy and performance analysis regarding fuel consumption and CO_2 emission reductions

- Address unique features of ship applications through payload and economic study

The third objective focuses on developing an optimization based design framework to find optimal system configuration and control strategy for any given load and weather profiles:

- Develop comprehensive correlation based cycle models, including cascaded cycle configurations

- Develop a design framework for combined system configuration and control strategy optimization

- Conduct optimizations for three different scenarios: single-objective optimization, bi-objective optimization and optimization under uncertainty

The fourth objective is investigating two microgrid system enhancement options for ship applications:

- Investigate separate sensible and latent cooling systems regarding thermal comfort and fuel saving enhancement under high humidity climates

- Investigate internal heat recovery methods and potentials through pinch analysis

2.2 Thesis Structure

The thesis is organized in following ways to present overall work clearly.

Chapter three presents component modeling and study. It divides into three sections: energy conversion cycle modeling as first section, including absorption cycle and vapor compression cycle modeling; energy source and demands modeling as second section, including engine, waste heat recovery, thermal zone and sea route weather models; experimental and modeling studies on desiccant wheels are the last section.

Chapter four presents dynamic system modeling based on component models introduced in Chapter three. Two scenarios were considered: solar energy powered and waste heat powered systems. Two different applications, cruise ships and container ships were considered. Limitations and challenges on real system designs were also discussed.

Chapter five presents the microgrid energy system optimization based design framework. The general framework is introduced first, followed by a case study in three different optimization scenarios: single-objective optimization, bi-objective optimization and optimization under uncertainty.

Chapter six presents microgrid energy system enhancement methods in two ways: integrating the separate sensible and latent cooling system and exploring internal heat recovery methods through pinch analysis.

Finally, major contributions, list of publications and future work are summarized in Chapter seven.

3 Microgrid System Component Study and Modeling

3.1 Energy Conversion Cycle Modeling

3.1.1 Absorption Cycle

Figure 3-1 presents the schematic diagram of a single effect absorption cycle (ABC). Detailed discussion on the ABC working principle can be found at [58]. There are two common working fluids for absorption cycle – NH_3/H_2O and $H_2O/LiBr$. NH_3/H_2O is more suitable for low temperature applications, while $H_2O/LiBr$ is more applicable for space cooling applications. In this study, the absorption cycle is primarily used for space cooling so that $H_2O/LiBr$ was selected as the working fluid. The single effect ABC was selected due to its compactness and easy maintenance, which is preferred for ship applications. The ABC is driven by hot water and cooled by sea water.
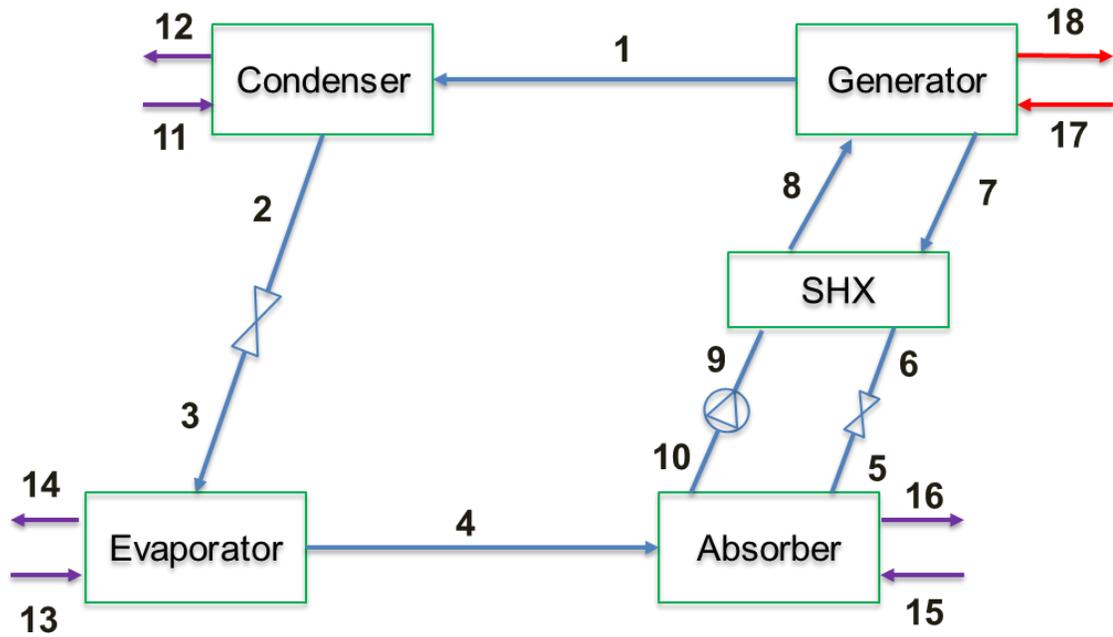
Figure 3-1: Schematic of single effect absorption cycle

Following assumptions were used to simplify modeling:

- Pressure drops and heat losses in connecting pipes and heat exchangers are neglected;

- The refrigerant leaving the evaporator is saturated vapor;

- The refrigerant leaving the condenser is saturated liquid;

- The solutions leaving the generator and absorber are both saturated;

- Throttling processes of refrigerant and solution are isenthalpic;

- The refrigerant and solutions leaving the generator are in thermal equilibrium.

Mass and energy balance analysis were conducted for each component based on [58].

The solution circulation ratio is defined in Equation (3-1).

$$f = \frac{M_{sp}}{M_r} \qquad (3\text{-}1)$$

The COP of the ABC is defined in Equation (3-2).

$$COP_{ABC} = \frac{Q_e}{Q_g + W_{sp}} \qquad (3\text{-}2)$$

Where Q_e is the cooling capacity of the evaporator, Q_g is the heat input to the generator and W_{sp} is the solution pump power consumption.

Approach Temperature (AT) was introduced to the heat exchanger (HX) model. The AT is the minimum temperature difference between two fluid streams in the HX. The AT of the generator is the difference between the inlet driving source temperature and the outlet strong solution temperature. The AT of the absorber is the difference between the inlet coolant temperature and the outlet weak solution temperature. The AT of the evaporator is the difference between the outlet chilled water temperature and the evaporation temperature. Table 3-1 shows the definition equations of AT. By introducing the AT, the temperature of the solution/refrigerant flows could be easily obtained.

Table 3-1: Definition equations of approach temperatures

Component	Approach temperatures
Generator	$AT_g = T_{17} - T_7$
Absorber	$AT_a = T_{10} - T_{15}$
Evaporator	$AT_e = T_{14} - T_3$

A computer program was developed for the ABC model based on AT method by using FORTRAN programming language [59].

Figure 3-2 shows the flow chart of the ABC modeling program. The model requires specifying the chilled water flow rate, return chilled water temperature and set chilled water temperature as inputs. These three inputs essentially determine the cooling demands. Then the program starts with an initial guess value of circulation ratio. Combined with other inputs, based on mass and energy balance equations, the state properties could be calculated. Hence the cooling capacity is obtained. It is then compared with the cooling demands. If the differences are with 0.1% of the higher values of the cooling demands and cooling capacities, the mass and energy balances of the ABC are considered to be reached. Otherwise, the circulation ratio is assigned with a new value and the iteration process is continued. That being said, the circulation ratio is the only parameter adjusted to match the cooling demands. When cooling demands increase, so does the refrigerant (H_2O) flow rate. The generator capacity also increases and leads to lower outlet hot water temperatures. Before heading to the final outputs, the calculated state properties need to be checked against operation constraints. Sometimes it may not be able to operate physically although the program is mathematically solvable. If there are constraints violated, the evaporator capacity and COP are presented as zero, along with warning signals of violated constraints.

If no constraints are violated, performance metrics including COP and HX duties are presented as outputs.

```
                    ┌──────────────────┐
                    │      Start        │
                    └──────────────────┘
                              │
                    ╱──────────────────╲
                    │    Inputs and      │
                    │    constraints     │
                    ╲──────────────────╱
                              │
                    ┌──────────────────┐
          ┌────────▶│ Assume circulation│
          │         │      ratio f      │
          │         └──────────────────┘
          │                   │
    No    │         ┌──────────────────┐
          │         │  Calculate state  │
          │         │    properties     │
          │         └──────────────────┘
          │                   │
          │         ◇───────────────────◇
          └─────────  Abs(Qein−Qeout)/Max(Qein,Qeout) < 0.001?
                    ◇───────────────────◇
                              │ Yes
                    ◇───────────────────◇
                    │ Violate operational │──────────┐
                    │     constrains?     │   Yes    │
                    ◇───────────────────◇           │
                              │ No                    │
                    ┌──────────────────┐   ┌──────────────────┐
                    │Calculate performance│  │Output: Warning signal│
                    │      metrics       │   │    and COP=0       │
                    └──────────────────┘   └──────────────────┘
                              │                        │
                    ┌──────────────────┐◀─────────────┘
                    │       End         │
                    └──────────────────┘
```

$$\frac{Abs(Q_{ein} - Q_{eout})}{Max(Q_{ein}, Q_{eout})} < 0.001?$$
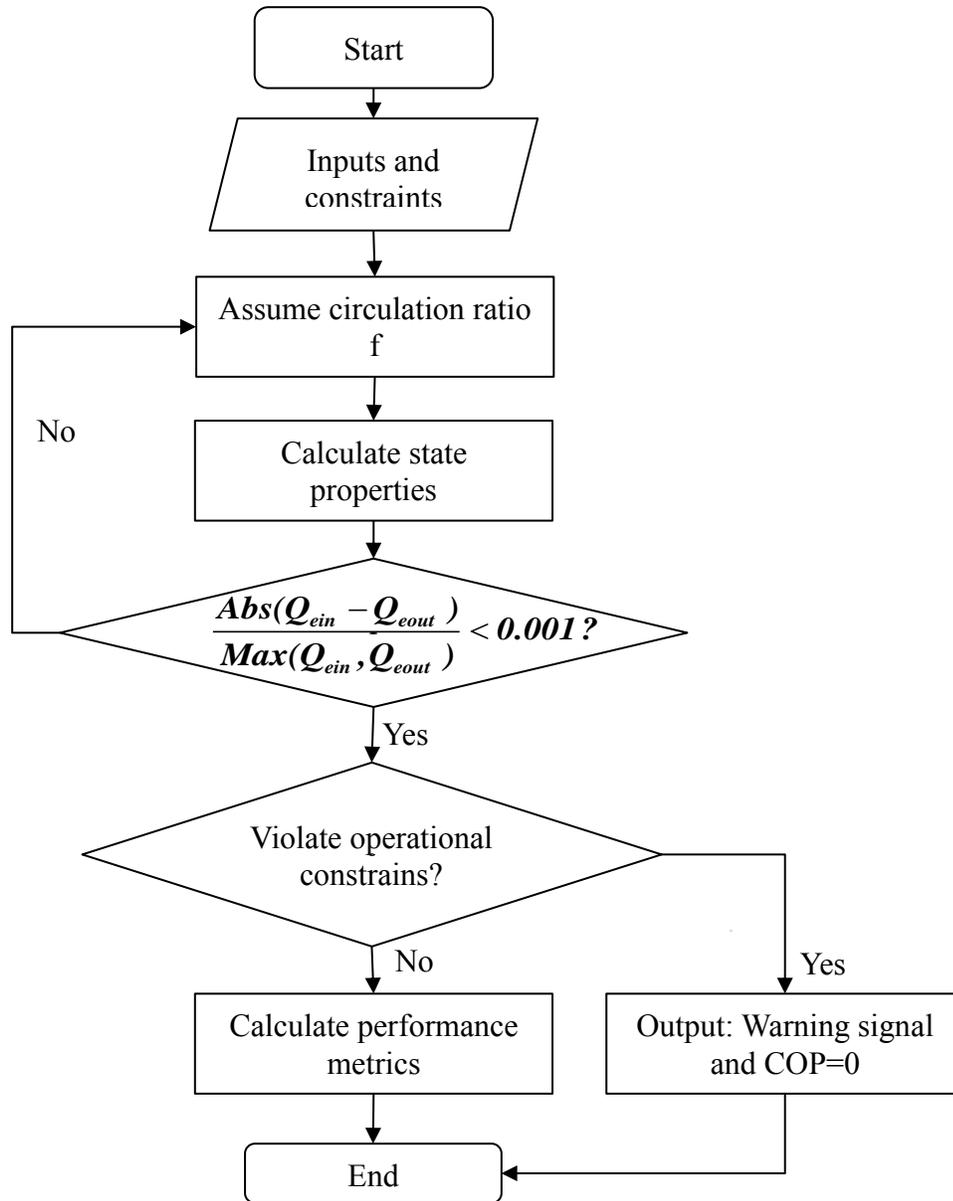
Figure 3-2: Flow chart of absorption cycle model with approach temperature method

Three main constraints were considered: crystallization, low evaporator temperature and property routine calls out of application range. Crystallization is the foremost operating issue of the H_2O/LiBr absorption cycle [58]. A polynomial equation of

23

crystallization criterion was developed and is shown in Figure 3-3. The data was obtained from American Society of Heating, Refrigerating and Air-Conditioning Engineers (ASHRAE) handbook [60]. The state properties of strong solution in absorber inlet (state 5) are compared with the polynomial equation. When the states are located above the line, crystallization happens. Note the application range of the crystallization equation is from 45 to 103°C. Low evaporator temperature criteria indicates that the refrigerant – H_2O in the evaporator cannot be below 0°C, otherwise freezing issue happens.

The plot shows Concentration (%) on the y-axis (64 to 71) versus Solution Temperature (°C) on the x-axis (40 to 120). The fitted curve equation is:

$$y = 0.0008x^2 - 0.0287x + 64.579$$
$$R^2 = 0.9984$$

with label "Crystallization Happens!" and a red arrow.
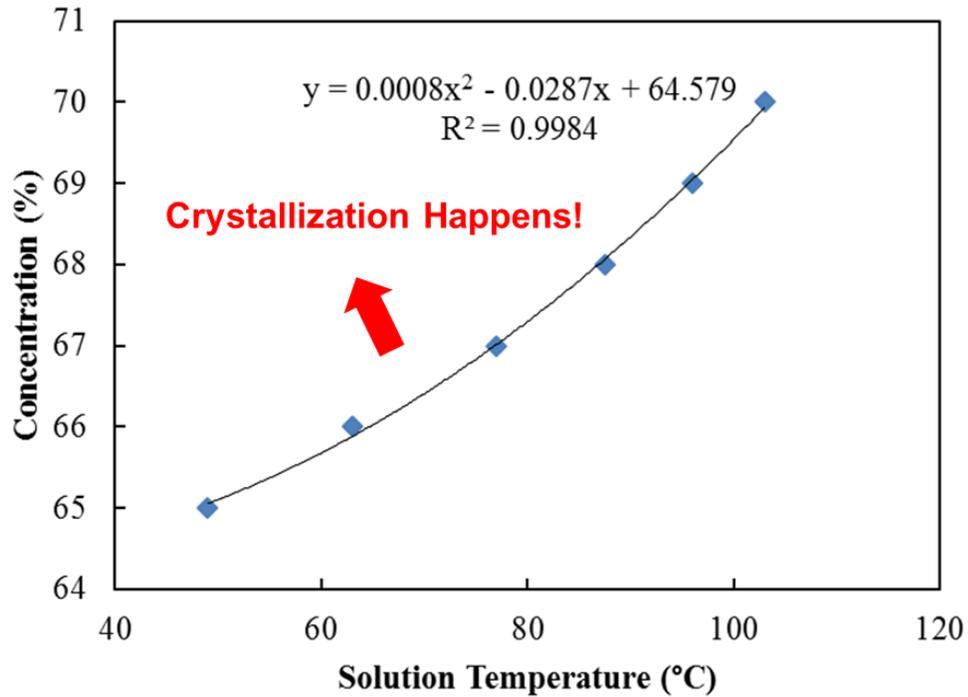
Figure 3-3: Crystallization criterion of H_2O/LiBr

Since there are no built-in property routines of H_2O/LiBr, correlations from the open literature were adopted and built in the program. For H_2O/LiBr solution, correlations from [61] were used. For H_2O, correlations from [62] were used. Such correlations come with application ranges. To make sure the results are valid, the property routine calls during the simulation were always checked against application ranges.

24

The simulation results were validated against data from [58]. Table 3-2 shows the comparison between the simulation results and data from open literature. As can be seen, the deviations are within 1%. Therefore, the model yields satisfying accuracy.

Table 3-2: Validation of absorption cycle model based on approach temperature method

Metrics	Open literature	Fortran Model	Deviation (%)
Q_e (kW)	10.57	10.68	0.98
Q_a (kW)	14.04	14.16	0.83
Q_c (kW)	11.21	11.27	0.49
Q_{shx} (kW)	3.060	3.058	-0.07
Q_g (kW)	14.68	14.75	0.46
COP (-)	0.720	0.724	0.57
x_w (-)	0.5670	0.5667	-0.05
x_s (-)	0.6240	0.6237	-0.05
p_e (kPa)	0.679	0.682	0.44
p_c (kPa)	7.347	7.352	0.07

3.1.2   Vapor Compression Cycle

VCC reefer units aim to condition reefer containers usually below 0°C and even down to -25°C in some cases. Typically, a reefer container is in either standard twenty-foot equivalent unit (TEU) or forty-foot equivalent unit (FEU). In this study, a meta-model of the VCC reefer unit was developed for the standard FEU. Figure 3-4 shows the flow chart of VCC reefer unit modeling.
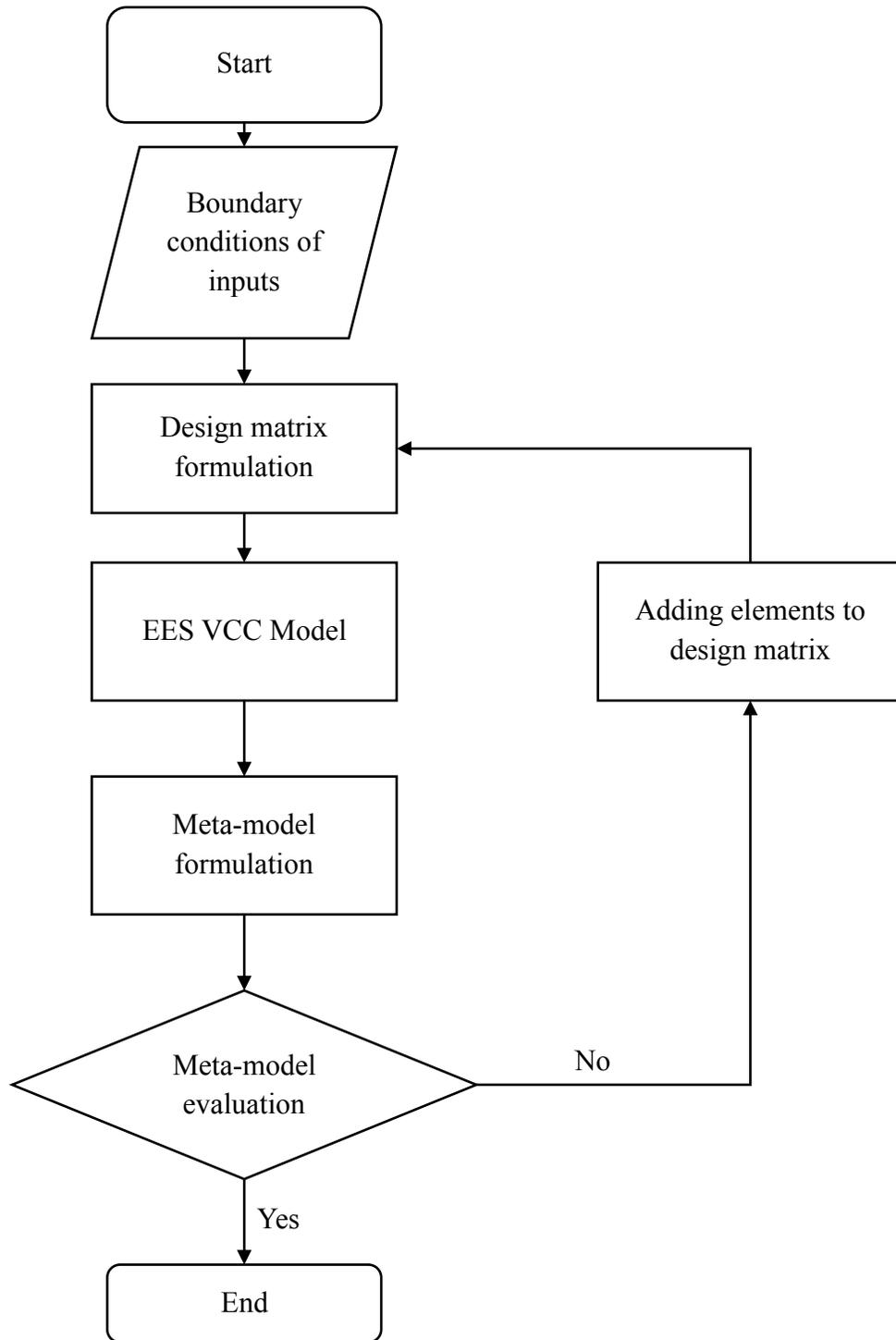
Figure 3-4: Flow chart of VCC reefer unit modeling

Boundary conditions of inputs were defined first to generate the design matrix. The

design matrix is the input for Engineering Equation Solver (EES) model. The EES model

conducts VCC modeling based on UA-LMTD heat exchanger model. UA values of condensers and evaporators were obtained by simulating the system under design condition. Simulation results from EES were then used to formulate the meta-model. The meta-model was validated against the empirical correlation. Until good accuracy is observed, more elements are added to the design matrix.

Two categories of the VCC (working fluid: R-404A) were modeled, the baseline and cascaded configurations. The difference lies in the condenser cooling source. The baseline VCC model is cooled by ambient air, while the cascaded VCC model is cooled by low temperature air, which is cooled by chilled water produced in the ABC. The condenser of the cascaded VCC model is operated in lower pressure than that of the baseline. If evaporators of both models work under same condition, the cascaded VCC model has smaller compressor power consumption due to lower pressure ratio.

To further clarify power saving of the cascaded system, a specific design point was investigated as an example. Both the baseline and cascaded system have evaporation temperatures of -20°C. The baseline VCC condenser is cooled by 30°C ambient air, while the cascaded VCC condenser is cooled by 7°C cooled air. Two cycles are plotted on P-h diagram, as shown in Figure 3-5. It is observed that the condensing pressure of the cascade system is much lower than that of the baseline system. The modeling results reveal a 52% compressor power reduction.
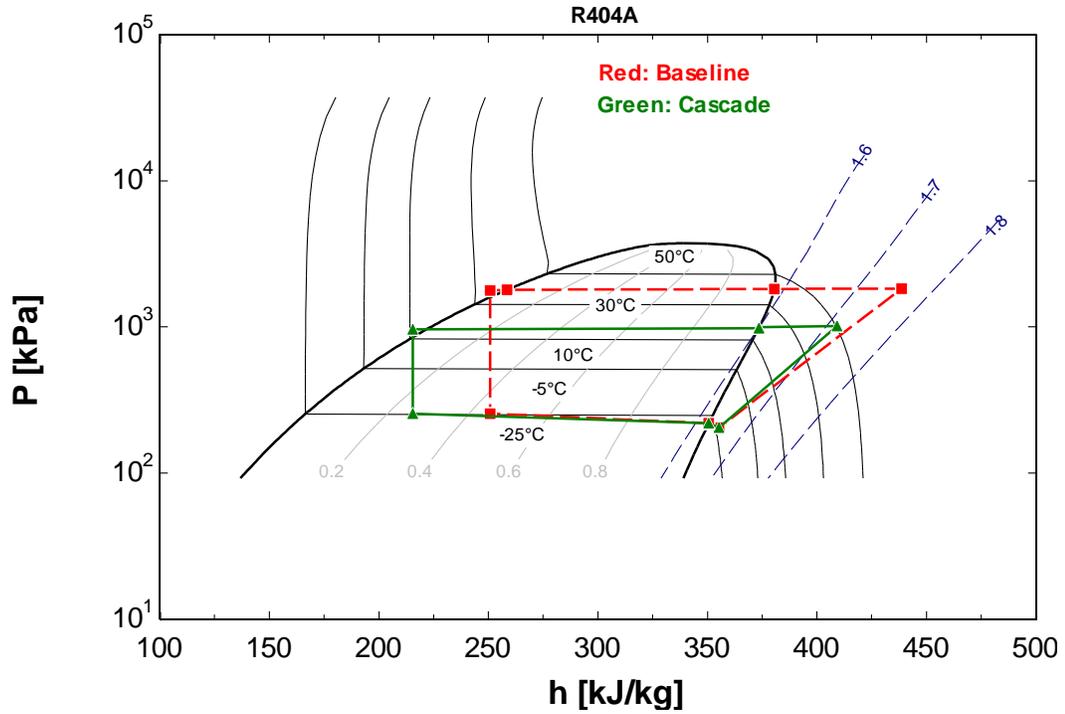
Figure 3-5: Comparison of VCC reefer unit performance under design conditions

Temperature settings of reefer containers range from 0 to -25°C. To simplify the problem, three temperature settings were considered: -5, -15 and -25°C. The capacity of a single VCC reefer unit was validated against the empirical correlation from Samsung Heavy Industry, shown in Equation (3-3).

$$\dot{Q} = (T_{air} + 35) \times 0.1165 \qquad (3\text{-}3)$$

$\dot{Q}$ is a single reefer unit capacity under -25°C temperature setting. Figure 3-6 shows validation results under a two-day temperature profile. The deviations are less than 2%, indicating a satisfying accuracy of the meta-model.
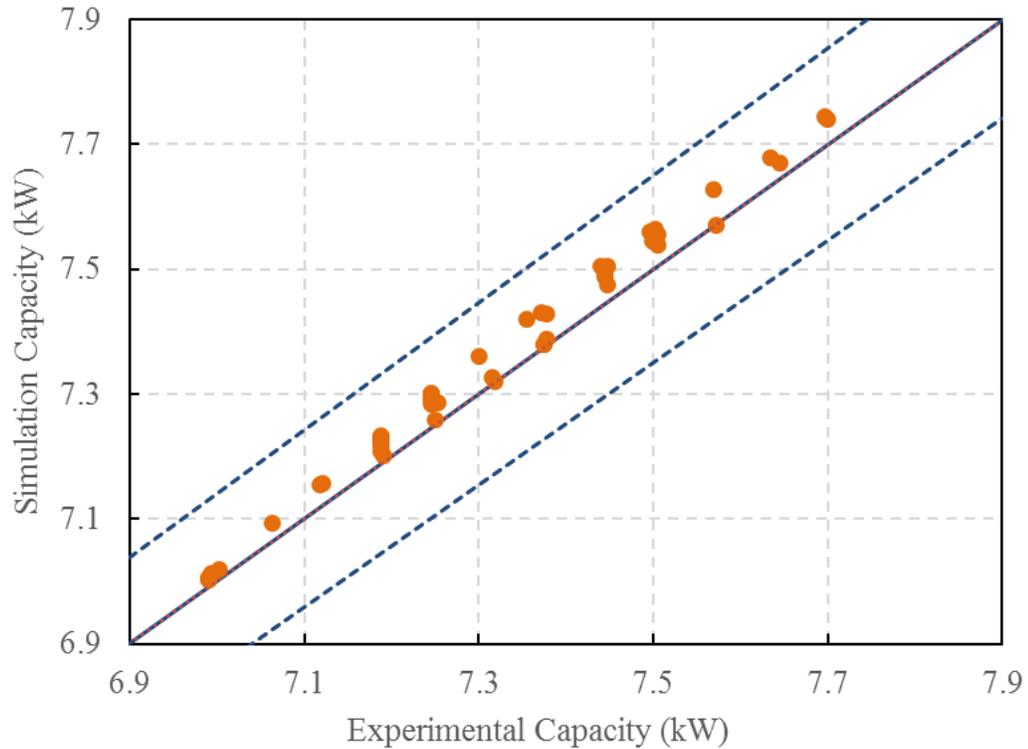
Figure 3-6: VCC reefer unit capacity validation

3.2 Energy Source and Demands Modeling

3.2.1 Main Engine and Waste Heat Recovery

Performance maps of the main engine were established based on engine manual data (Engine model: WARTSILA 8RT-flex68-D; Rated capacity: 25,040 kW) from Samsung Heavy Industry. The main engine was modeled for two purposes – getting to know energy flows of the main engine and exhaust gas indices. Energy flows of the main engine consist of propulsion and various heat losses. Capacities of propulsion and heat losses vary with main engine power ratio.

Two waste heat recovery systems – an exhaust waste gate (economizer) and an engine cooling system (scavenge air cooler, engine jacket, and oil cooler) were set up in transient systems simulation program TRNSYS [63] based on engine configurations. The exhaust waste gate aims to recover energy in exhaust gas, while the engine cooling system recovers energy from scavenge air, engine, and lubricant oil. Each waste heat source has a dedicated heat recovery HX, where waste heat source flows through the HX and transfers energy to cooling water/air. Standard pump (Type 741) and HX (Type 5b) components from TRNSYS were used in modeling. The UA values of HXs were defined based on engine specifications. Waste heat source flow rates and inlet temperatures were defined based on engine performance data, which vary with power ratios. The cooling water/air flow rates and inlet temperatures were defined as inputs. As the power ratio changes, outlet temperatures of waste heat source and cooling water/air are changed. Consequently, waste heat capacities vary.

The simulation system was validated against experimental data from Samsung Heavy Industry. Table 3-3 presents the four categories of waste heat sources on a cargo ship, along with the temperature range, recovery device and simulated HX capacities under 100% power ratio. The heat capacities show less than 3% deviation, hence the simulation program yields good accuracy. It should be noted that the capacity from the exhaust gas is the capacity of the economizer, which is used to generate service steam. A current economizer design could only cool the outlet exhaust gas temperature down to 170°C. However, it can be furthered cooled down to 140-150°C without interrupting engine operations.

Table 3-3: Classification of waste heat source on a cargo ship

Waste heat source	Temperature (°C)	Heat Exchanger	Capacity: simulation results (kW)	Capacity: experimental results (kW)	Deviation (%)
Exhaust gas	250 to 350	Economizer	6,894	6,804	1.33
Scavenge air	130 to 150	Scavenge air cooler	9,847	9,951	-1.04
Engine	70 to 120	Engine jacket	3,402	3,280	3.73
Lubricant oil	Up to 200	Oil cooler	2,111	2,125	-0.67

As exhaust gas has highest temperature ranges, which indicates huge amount of available energy, this study focuses on it. The exhaust gas is used to heat up water, which powers up the absorption cycle. Two important parameters, exhaust gas flow rate and temperature, are needed. They are dependent on power ratios and ambient air temperatures, as shown in Figure 3-7 and Figure 3-8, respectively.
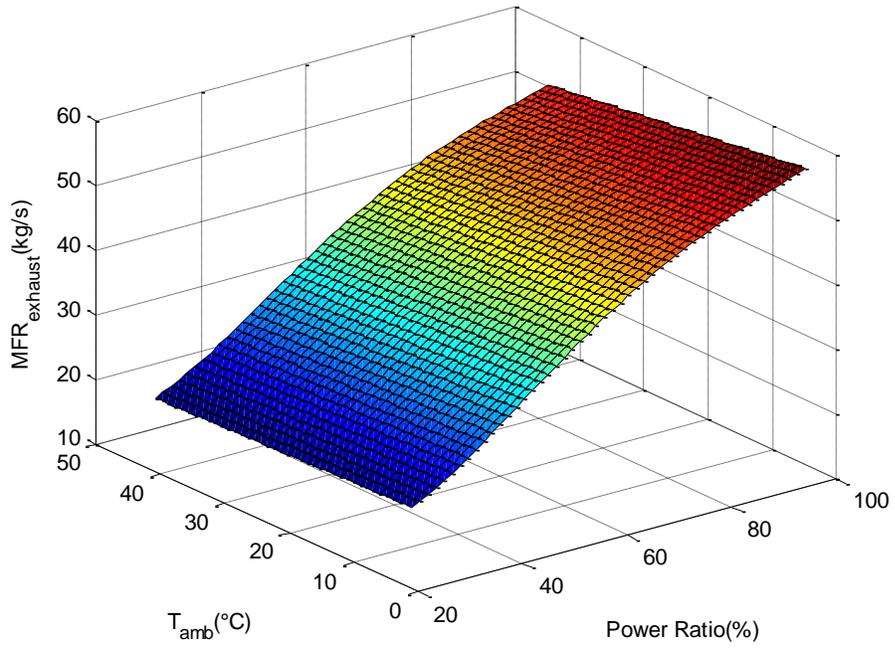
Figure 3-7: Engine exhaust gas flow rate performance map
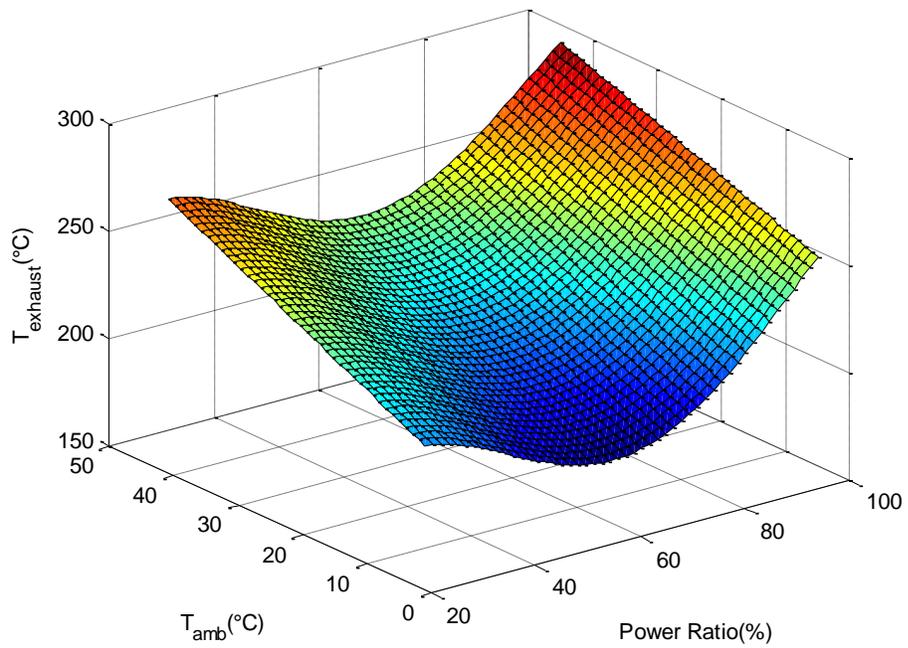
Figure 3-8: Engine exhaust gas temperature performance map

32

3.2.2   *Thermal Zone*

One of the advantages of TRNSYS is the capability of the detailed building modeling. The ship structure was developed in Google SketchUp first [64]. Then the structure was exported to TRNBuild [65], in which the weather data, internal heating loads, ventilation and heating/cooling information could be integrated with TRNSYS. The TRNSYS conducted all calculations and provides outputs, including psychometric conditions at each time step.

Figure 3-9 shows the cargo ship structure created by SketchUp, based on the manufacture specifications. Total 140 cabins were created for living spaces and refrigeration containers. Specifically, 16 cabins need space cooling.
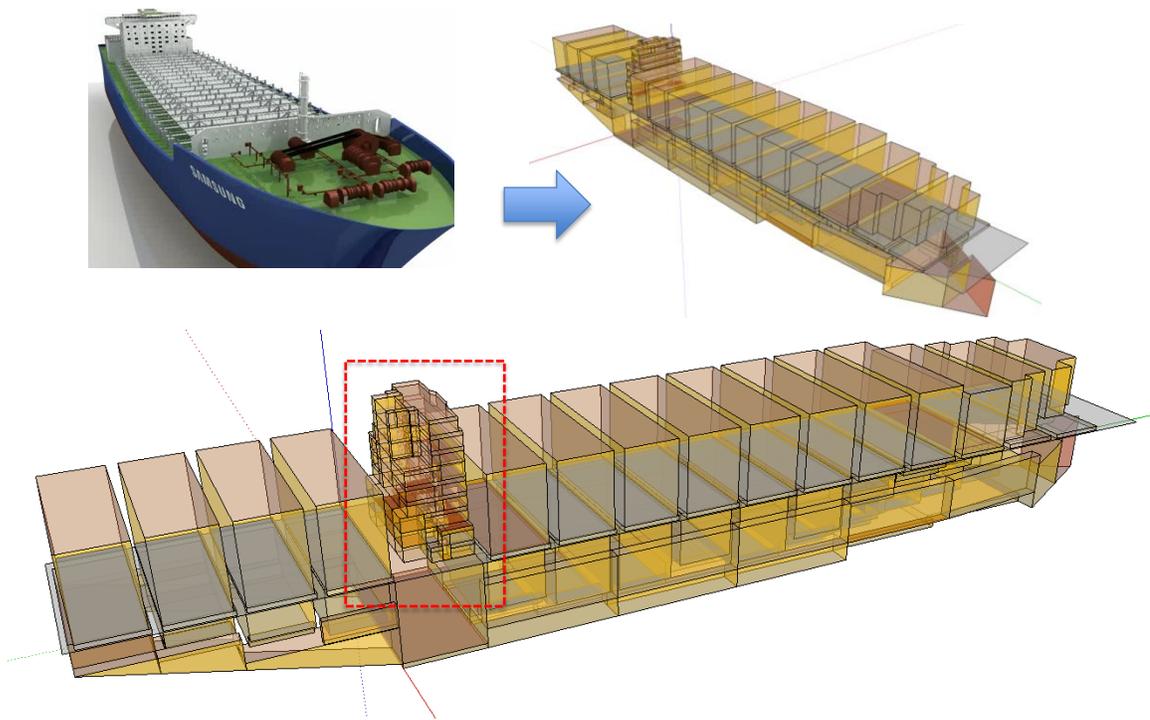
Figure 3-9: Cargo ship structure development

Table 3-4 shows the details of 16 living spaces, including cabin categories, details about occupants and internal heat loads. The cabin insulations were also specified for

different types of walls. The materials, thicknesses and U values are summarized in Table

3-5.

Table 3-4: Conditioned space specifications

Cabin (Floor-Room No.)	Cabin category	Cabin floor area (m²)	Peak occupants	Miscellaneous heat gains (W)
A2	Office space	55.49	8	243
A3	Bedroom/living room	16.15	6	435
A5	Bedroom/living room	8.59	3	412
C3	Bedroom/living room	40.88	11	779
C4	Office space	32.29	13	681
D1	Bedroom/living room	24.22	2	185
D2	Health facility	24.22	4	628
D3	Bedroom/living room	62.54	4	1188
D5	Health club	24.73	4	175
D6	Health club	28.26	4	775
E1	Bedroom/living room	110.99	8	746
E3	Health club	48.28	9	591
F2	Office space	97.55	6	461
F4	Health club	48.28	9	624
G1	Office space	110.99	10	966
H1	Office space	110.99	12	1148

Table 3-5: Wall material details of conditioned spaces

Wall Type	Layer	Thickness (m)	U value $(W \cdot (m^2 * k)^{-1})$
Adjacent Wall	Fiberglass + Steel	0.074	0.549
Interior Ceiling	Steel	0.081	5.701
Interior Floor	Steel	0.008	0.04
Interior Wall	Steel	0.008	5.864
Exterior Floor	Timber + Steel	0.038	0.039
Exterior Roof	Plasterboard + Fiberglass + Steel	0.149	0.316
Exterior Wall	Fiberglass + Plasterboard + Wood + Steel	0.095	0.51
Ground Floor	Steel + Fiberglass	0.074	0.037

Solar radiation from TRNSYS weather data (TMY2) were used. One unique feature about this study is that the sea route is almost straight line as it is relatively short from Miami to Bahama. Therefore, within a sailing period (about 8 hours), the ship cabins are remained in fixed orientations. However, the solar angle does change over time based on TMY2 weather data. That being said, the ship cabins were set up according to its initial position in Miami port, with shapes, shading and orientations specified. TRNSYS then handles the effects of solar radiation on cabin cooling loads. Solar radiation impacts cooling loads in two major ways: direct radiation interactions with external living cabins (the ones located on the top floor and have external walls) and effects on air temperature fluctuations (between day and night time). The former one increases the cooling loads of the exterior cabins in the daytime significantly, while the second factor impacts all cabins in an obvious way that daytime cooling loads are always higher than that of nighttime. While TRNSYS takes care of the effects of solar radiation and ambient conditions on living space, the internal heat loads have to be carefully defined by users. In this study, they were divided into three categories: lighting, occupants and other miscellaneous loads. The

heating gain due to lighting was assumed to be 5 $W \cdot m^{-2}$. The sensible and latent heating gains due to occupants were defined according to standard ISO 7730 [66]. Other miscellaneous heat gains such as electronic equipment were based on experimental data.

3.2.3 *Sea Route Weather*

Shipboard energy conversion equipment performance heavily relies on weather conditions, in particular air and sea water temperature. In addition, air humidity information is needed for living space thermal comfort analysis. All these weather data along a sailing route can only be recorded by ship operators. Unfortunately, such data is usually not available to the public. There may also be some missing periods due to maintenance or severe weather conditions. As a result, a sea route weather module was developed based on open database – International Comprehensive Ocean-Atmosphere Data Set (ICOADS) from National Oceanic and Atmospheric Administration (NOAA) [67]. Table 3-6 summarizes weather data information provided by ICOADS.

Table 3-6: Overview of ICOADS datasets

Resolution	1° * 1°
Time interval	Monthly
Sea surface temperature	°C
Air temperature	°C
Air relative humidity	%
Wind speed	$m \cdot s^{-1}$

ICOADS provides weather data for each location on monthly basis. The weather data consists of monthly average values and standard deviations. The standard deviations are usually less than 5% of average values [67], indicating mean values are able to represent any hourly weather data within the month while not degrading the accuracy greatly. As the

simulation program needs weather data for each location on hourly basis, average values of the same month with the sailing period were employed to represent the hourly data for each location along the route.

In this study, two sea routes were selected. One is from Pusan, South Korea to Karachi, Pakistan, which lasts about 1,000 hours. The other is from Tokyo, Japan to San Francisco, U.S.A, which lasts about 300 hours. Both route sailing times are in August. The weather data for the first route is available from ship owners. Hence only the weather module from Tokyo to San Francisco was developed. Figure 3-10 shows the air and sea water temperatures along the sea route from Tokyo to San Francisco. Figure 3-11 presents air temperature and humidity on a psychrometric chart.
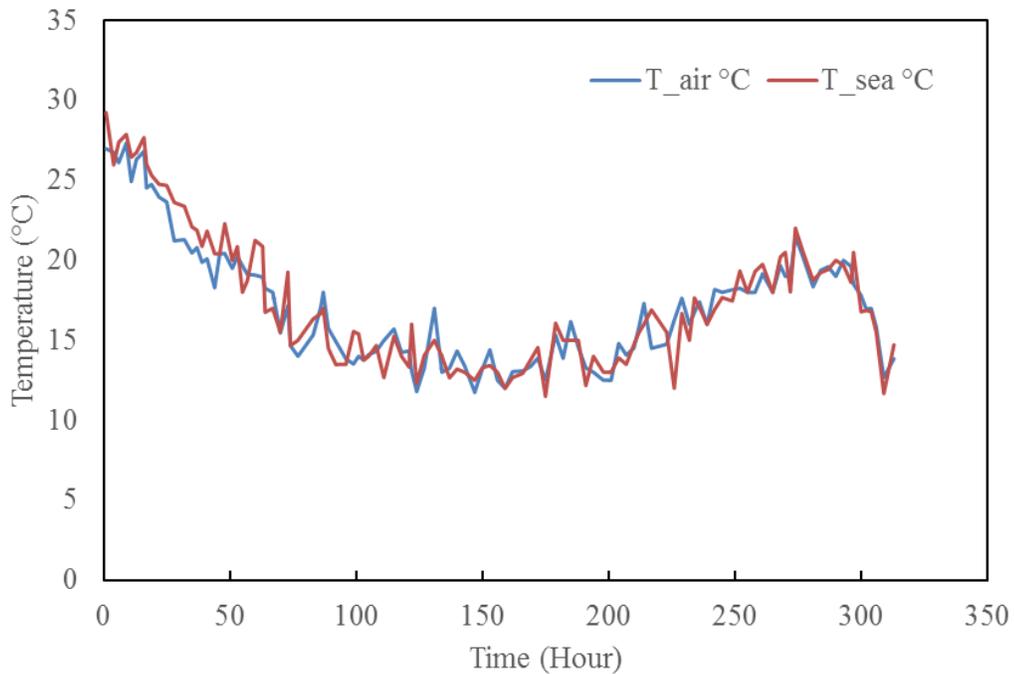
Figure 3-10: Temperature profiles along sea route from Tokyo to San Francisco
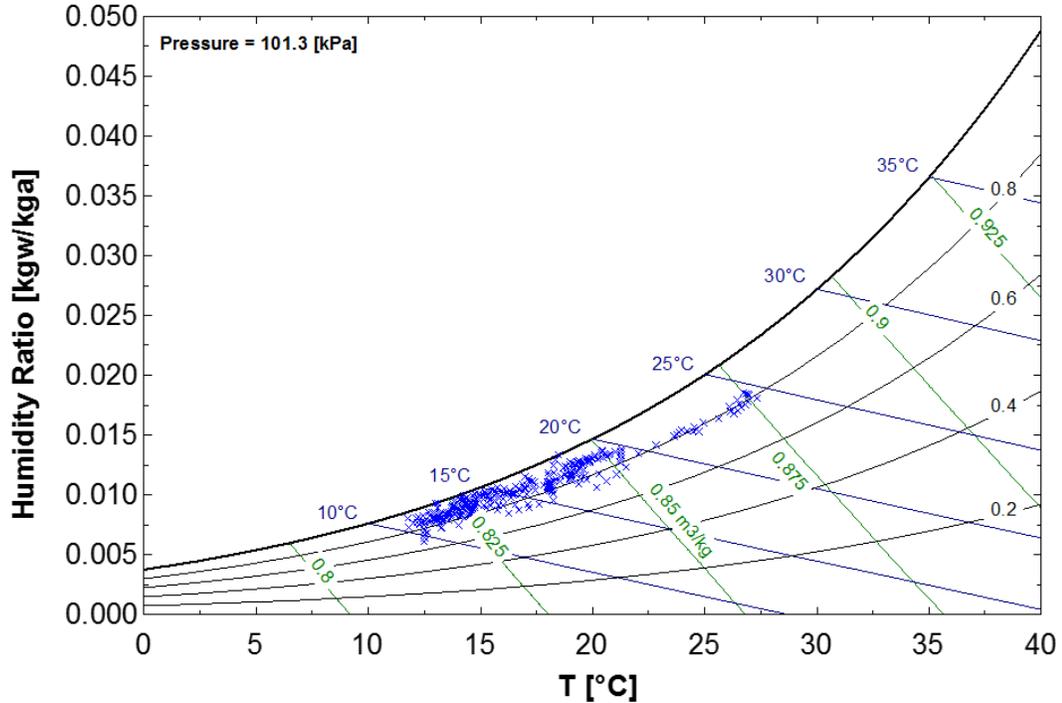
Figure 3-11: Air properties along sea route from Tokyo to San Francisco

3.3 Desiccant Wheel Study

3.3.1 Background and Literature Review

In hot and humid regions, removing moisture from the air accounts for a considerable portion of the air conditioning load. Most air conditioning systems have to lower the air temperature below its dew point to accomplish dehumidification. Solid desiccant cooling has been proposed as an alternative to vapor compression refrigeration for space cooling. It is an environmentally beneficial solution since no ozone depleting refrigerants are needed. Instead, low temperature heat sources, like waste heat from engine or solar heat, can be used to operate the system. Desiccant wheels (DW) are used for dehumidification of the humid air. While silica gel is the most commonly used desiccant material, new materials have been developed and tested. Jia et al. [68] compared two DW

38

materials which were silica gel and a newly developed composite material (mixture of silica gel and lithium chloride). They reported that the newly developed composite desiccant wheel performed better than the conventional one, and could remove 50 percent more moisture. White et al. [69] studied two materials (zeolite and a superabsorbent polymer) and compared them with silica gel. They found that these two materials were more effective in dehumidification than silica gel at low regeneration temperature (50°C) and high relative humidity (higher than 60 percent). Lee [70] tested a newly developed desiccant material – a superabsorbent polymer and found that it had two to three times higher sorption capacity. Qian et al. [71] conducted an experimental investigation on the performance of an adsorption chiller with zeolite, which works well at a low regeneration temperature and is also one of commonly used desiccant materials.

Lots of experimental studies have been conducted to investigate the performance of DWs. Ahmed et al. [72] conducted the evaluation and optimization of a solar DW performance. A numerical model was developed and validated with experimental data. Moreover, parametric studies were conducted to investigate the effects of the design parameters such as rotational speed, regeneration to adsorption area ratio, and the operating parameters such as air flow rate, inlet air humidity ratio, and regeneration air temperature on the wheel performance. Enteria et al. [73] evaluated the desiccant wheel based on its moisture removal capacity (MRC) and moisture removal regeneration (MRR). Eicker et al. [74] investigated several commercially available desiccant wheels, and determined the best rotational speeds for different DWs. Angrisani et al. [75] conducted an experimental analysis of the DW, which focused on the variations of the performance as a function of the process and regeneration air flow rates. The desiccant material was regenerated by low

temperature thermal energy from a micro co-generator. Angrisani et al. [76] also conducted experimental tests on a silica gel DW to highlight the effect of rotational speed on its performance. Narayanan [77] designed a non-adiabatic DW and examined its performance through mathematical models and experimental testing. The new design could increase the dehumidification level by around 45 to 53 percent.

Mathematical models of DW have been developed to effectively predict DW performance in a reasonable computation time. There have been multiple modeling studies on DW in recent years. Wrobel et al. [78] validated a simplified model based on the results of the physical model for a DW. Yamaguchi and Saito [79] established mathematical model to predict silica gel DW performances. Their predicted results were similar to their measured results. The recorded differences were 3.3% for humidity ratio and 10.8% for temperature. Antonellis et al. [80] developed a one dimensional model to solve heat and mass transfer within a DW. The model supported a wide range of working conditions and sorption wheel configurations. The performance criteria were also introduced and discussed based on simulation results. Ghiaus et al. [81] proposed a state space model for a DW control with two approaches – black box and gray box. The gray box has fewer requirements for parameter identification than black box approach. Chung and Lee [82] optimized the performance of a DW by using an unsteady one-dimensional numerical model. The optimum condition was determined by maximizing MRC under different regeneration temperatures (50 to150°C) and desiccant isotherm shapes. Aprile et al. [83] carried out gray-box modeling of a silica gel desiccant wheel for a full-scale desiccant evaporative cooling system. An accurate response model including inlet temperature and rotational speed, was proposed and tested in a wide range of operating conditions. Ruivo

et al. [84] applied the effectiveness method to predict the influence of inlet conditions on the behavior of DW. Several interpolation approaches were evaluated and compared with a numerical model. Chung et al. [85] optimized the rotational speed and regeneration to process area ratio for a range of regeneration temperatures on the basis of maximum MRC. Ali et al. [86] presented a model to predict a DW performance under transient conditions. The model was capable of estimating the optimal rotational speed and pressure drop of the DW. The simulation results of the model corresponded to the published data. Wang et al. [87] proposed a model to control indoor air humidity with a DW. This experiment was conducted to illustrate the applications of the model's predictive control strategy. Goldsworthy et al. [88] developed a numerical model to investigate the influence of the desiccant equilibrium adsorption isotherms on the overall wheel performance. They found the extent of dehumidification was limited primarily by thermal affects caused by both the exothermic adsorption process and the carryover of heat from the regeneration stream. Panaras et al. [89] investigated a simplified approach for DW modeling. The experimental analysis covered a wide range of operating conditions including flow rate, temperature and humidity.

The desiccant wheel has been widely used and investigated in various hybrid cooling systems. Models and experimental studies on the system's performance are necessary for improving the system design and commercialization. Subramanyam et al. [90] discussed integrating a desiccant in an air-conditioner to decrease humidity. The supply air was dehumidified by the desiccant wheel, and the return air from the space was used to regenerate the DW. Enteria et al. [91] evaluated the solar-desiccant cooling system performance with a new desiccant material (titanium dioxide) at different climates in East-

Asia. Finocchiaro et al. [92] investigated an innovative desiccant cooling cycle using wet heat exchangers. A temperature ranging from 21 to 22°C could be achieved by the optimization of the indirect cooling process. The electricity consumption was also greatly reduced compared to the previous prototype. Chung et al. [93] analyzed the effect of eleven design parameters on the performance of a desiccant cooling system under two different system configurations. They found that the regenerative temperature was the most dominant factor. Sheng et al. [94] proposed a high temperature heat pump, a DW system, and an air condition unit to meet space cooling and heating demands. The COP of the whole system was 2.08.

Table 3-7 shows a summary of the recent experimental studies on desiccant wheels, and lists the regeneration temperature, desiccant materials and dimensions. The literature review showed that most experimental studies were conducted with silica gel at high regeneration temperatures. Also, most DWs are thicker than 100 mm, with large diameters. There are currently limited researches conducted with DWs thinner than 100 mm. In order to have compact system packaging, a thin DW is required. Although Eicker [74] and Yamguchi [79] experimented with thin DWs, they only focused on high regeneration temperature (80°C). No other study on the potential of thin DWs has been found. In order to respond to this research gap, we investigated the performance of thin polymer DWs at low regeneration temperatures (40, 50 and 60°C). In this study, effects of inlet air temperature, humidity ratio, regeneration temperature and rotational speed on the DW performance were evaluated. Moreover, the performances of thin DWs (30 mm, 50 mm and 70 mm) were compared with that of the typical thickness DW (150 mm thickness), and

then the potential of the thin DWs in compact cooling and dehumidification systems was discussed.

Table 3-7: Distinguished features of literature on DW studies

Author (year)	Regeneration temperature (°C)	Material	Dimensions (diameter/thickness) (mm)
Subramanyam et al. (2004)	Lower than 30	Metal silicate synthesized on inorganic fiber substrate	450/200
Ahmed et al. (2005)	60 – 90	Galvanized iron	700/200
Jia et al. (2006)	60-120	Silica gel Silica gel and lithium chloride	400/200
Enteria et al. (2010)	60, 70, 80	Silica-gel	300/100
White et al. (2011)	50, 80	Zeolite and superabsorbent polymer	300, 360
Enteria et al. (2012)	60-80	Silica-gel, Titanium dioxide	-
Eicker et al. (2012)	45-90	Titanium silicate Lithium chloride Silica gel Silica gel and lithium chloride	870/140 895/250 260/16.6,100 260/16.6,100
Angrisani et al. (2012)	65	Silica-gel	700/200
Angrisani et al. (2013)	60-70	Silica-gel	700/200
Wrobel et al. (2013)	45-50	Lithium chloride (LiCl)	650/200
Yamaguchi and Saito (2013)	50-80	Glass fiber	350/20, 60, 100, 200, 400

3.3.2   Experimental Setup

Figure 3-12 shows the schematic diagram of the experimental setup. A counter flow design was applied between the two air streams across the desiccant wheel. Two wind tunnels were constructed with polypropylene boards to simulate regeneration air and process air streams. Two variable speed fan motors were installed in the downstream of both tunnels to regulate the air flow rates. The desiccant wheel used was a cylindrical shape

with honeycomb-shaped cells, which slowly rotates as it continuously dehumidifies the incoming process airstream. The test facility was placed in an environmental chamber where the inlet temperature and relative humidity could be controlled.
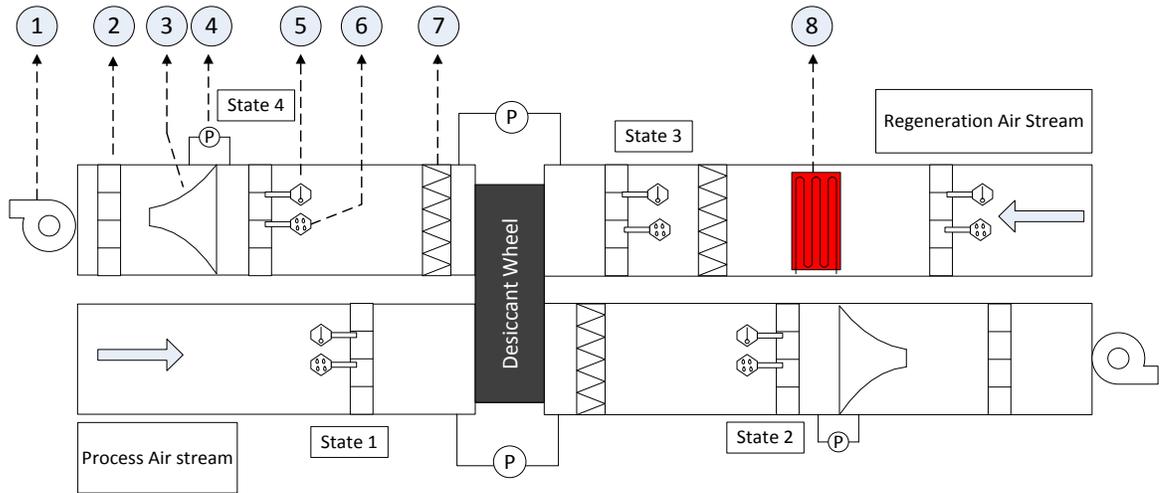
Figure 3-12: Schematic for polymer desiccant wheel testing system

(① fans; ② straightener; ③ nozzles; ④ differential pressure transducers; ⑤ thermocouple grids; ⑥ humidity sensors; ⑦ air mixers; ⑧ electric heaters)

For the process air stream, a relatively high humid air enters the DW and moisture is adsorbed by the desiccant. The air then passes through the nozzle to measure the air flow rate and exits the tunnel. The temperatures and humidity of both inlet and outlet air streams, and pressure drop across the nozzles and the DW were measured. For the regeneration air stream, an electric heater was used to simulate the regeneration heat source and control the regeneration air stream to the target temperature. The high temperature, low humidity air then enters the DW and moisture is released from the desiccant. The air exiting the DW passes through the nozzle and exits the tunnel, similarly to the process air stream. The testing facility was designed according to ANSI/ASHRAE 41.2-1987 (RA 92) – standard methods for laboratory air flow measurement [95].

An effort was made to minimize the air leakage between the process and regeneration air streams, which can degrade the desiccant DW's performance by increasing process air outlet temperature. Air leakage can also decrease the accuracy of test results. The DW case contained two aluminum frame plates, four layers of sealing gaskets (two are silicone foam and the other two are glass fiber), three steel threaded rods, three springs and six nuts. The DW was located in the middle. Two layers of glass fiber gaskets were attached to both surfaces of the DW. They can provide a smooth surface, allowing the DW to rotate with a minimum friction. The silicone foam gaskets were used next to the glass fiber gaskets. The aluminum frame plates were then attached to the silicone foam gaskets. Three steel threaded rods were used to hold the DW and gaskets. Two nuts were used in both ends of each bolt rod to lock them into place. The springs were used to apply pressure force on the plates against the DW.

T-type thermocouples were used for temperature measurement in all state points. In addition, resistance temperature detectors (RTD) and relative humidity (RH) sensors were also used to measure air stream temperatures and RHs. For the thermocouples, a nine-point grid system was used, which contained nine evenly distributed thermocouples. The average values of the nine thermocouples were taken as a final temperature reading. The readings of thermocouple grids and RTDs were compared, and the temperature differences were within 0.2°C. The RH sensors were installed in the center of air flow stream, next to thermocouple grids. All properties obtained such as temperatures and RHs were used to evaluate the psychometric properties including humidity ratio and enthalpy. Differential pressure (DP) transducers were employed to obtain the mass flow rates of two air streams, and to quantify the pressure drop across the DW. The power consumption of the electric

heater was measured with digital watt meters. With known temperatures before and after the heater, the mass flow rate of regeneration air upstream could be obtained. Specifications of sensors are provided in Table 3-8. The RH, DP sensors, and air flow rate were calibrated under testing conditions.

Table 3-8: Specifications of sensors

Sensors	Manufacturer	Model No.	Measurement range	Systematic Error
Thermocouple	Omega	T type	-185 ~ 300 °C	± 0.5 °C
DP transducer	Setra	264	623 Pa	± 1.0% FS
RH sensor	Vaisala	HMT313	0 ~ 100 % RH	± (1.0 + 0.008 × reading) % RH
RTD	Vaisala	HMT313	-20 ~ 80 °C	± 0.25 °C
Watt meter	Ohio Semitronics	GH-019D	0 ~ 4 kW	± (0.2% reading + 0.05% FS)

The data acquisition system (DAQ) was established with LabVIEW, which can control the relative humidity, temperature and mass flow rate of all four state points. Table 3-9 shows the specifications of the four DWs tested. All DWs were made of polymer material and had the same diameter, except for the 150 mm thick DW. The thicknesses varied from 30 to 150 mm. The first three were considered as thin DWs as they were thinner than 100 mm. The test matrix is provided in Table 3-10. For each condition, seven different rotational speeds were used. Initially, the chamber was turned on and set to the desired temperature and humidity conditions. After that, both fan motors and DW motor were turned on. Once the desired air conditions were reached, the electric heater was turned on to obtain the desired regeneration temperature. After steady state conditions reached, data were recorded for 30 minutes with a one-second time interval.

Table 3-9: Specifications of desiccant wheels

No.	Material	Diameter (mm)	Thickness (mm)
1	Polymer	300	30
2	Polymer	300	50
3	Polymer	300	70
4	Polymer	350	150

Table 3-10: Test matrix

No.	T_{p_in}	w_{p_in}	w_{r_in}	Volume flow rate		T_{gen}	R_{speed}	Test duration
	°C	gw·kga⁻¹	gw·kga⁻¹	m³·s	m³·hr⁻¹	°C	RPH	min
1	25	15	15	0.10	360	60		30
2	30	15	15	0.10	360	60	10 to 70 with 10 as interval	30
3	35	15	15	0.10	360	60		30
4	30	10	10	0.10	360	60		30
5	30	20	20	0.10	360	60		30
6	30	15	15	0.10	360	50		30
7	30	15	15	0.10	360	40		30

3.3.3 Methodology

The moisture removal capacity quantifies the amount of moisture removed from the processing stream as it passes through the DW, given by Equation (3-4).

$$MRC = \dot{m}_p \left(\omega_{p\_in} - \omega_{p\_out} \right) \tag{3-4}$$

The latent coefficient of performance (COP$_{latent}$) relates the changes in latent energy along the processing stream to the energy input required to regenerate the desiccant, given by Equation (3-5). The W$_{in}$ is the power consumption of electric heater.

$$COP_{latent} = \frac{\dot{m}_p h_{fg} \left(\omega_{p\_in} - \omega_{p\_out} \right)}{W_{in}} \tag{3-5}$$

The MRC and COP$_{latent}$ are the most commonly used indicators when evaluating the performances of a DW. The values of MRC and COP$_{latent}$ increase as the

47

dehumidification capacity increases at a given heat input, making it a more efficient system. However, the MRC and COP$_{latent}$ usually reach their maximum under different testing conditions, which is discussed in the experiment results section.

The sensible energy ratio (SER) is also used when evaluating the DWs. During the dehumidification of process air, heat is released from the desiccant wheel as a result of the adsorption process, as well as the unintentional heat transfer from the regeneration air stream to the process air stream due to the temperature differences between the two. Therefore, the SER can quantify this additional sensible load to be handled by some additional cooling mechanism at the downstream such as an evaporative cooling or a vapor compression cycle. Lower values of SER mean that the DW is creating a lower sensible cooling load, which indicates better performance of the DW. The SER is given by Equation (3-6).

$$SER = \frac{\dot{m}_p \left(T_{p\_in} - T_{p\_out} \right)}{\dot{m}_r \left(T_{p\_in} - T_{gen} \right)} \tag{3-6}$$

In this study, the performance of four DWs was evaluated with different thickness: 30, 50, 70 and 150 mm. The DW with 150 mm thickness had a larger diameter (350 mm) than the other three DWs (300 mm). Since the air flow rate was maintained at constant throughout all tests, the face velocity of 150 mm DW was lower (2.0 m/s) than the other three DWs (2.8 m/s). To ensure thickness was the only variable, we converted the MRC test data of the 350 mm diameter DW to that of the 300 mm diameter DW, while maintaining the same face velocity with the other three DWs. An example of MRC conversion equation is given in Equation (3-7).

$$MRC_{new} = MRC_{old} \frac{300^2}{350^2} \times \frac{2.8}{2} \tag{3-7}$$

The experimental error can be classified into two broad categories: systematic error and random error, which typically accounts for the uncertainty of the acquired data. The systematic error is associated with the various instrumentation precisions, manifested in temperature, pressure, and relative humidity measurements. The random error pertains to the acquired data deviation from the mean value. Performance indices, or dependent variables, are correlated with the error propagation of the individual measurement uncertainties. The general error propagation is given by Equation (3-8). Here u is a function of x, y and z. Δu is the uncertainty of u, similar to Δx, Δy and Δz.

$$\Delta u = \sqrt{\left(\frac{\partial u}{\partial x}\right)^2 \cdot (\Delta x)^2 + \left(\frac{\partial u}{\partial y}\right)^2 \cdot (\Delta y)^2 + \left(\frac{\partial u}{\partial z}\right)^2 \cdot (\Delta z)^2} \tag{3-8}$$

An example for the propagated error, pertaining to MRC is given below by Equation (3-9).

$$\Delta MRC = \sqrt{\left(w_{p\_in} - w_{p\_out}\right)^2 \cdot \left(\Delta \dot{m}_p\right)^2 + \left(\dot{m}_p \cdot w_{p\_out}\right)^2 \cdot \left(\Delta w_{p\_in}\right)^2 + \left(\dot{m}_p \cdot w_{p\_in}\right)^2 \cdot \left(\Delta w_{p\_out}\right)^2}$$

$$(3-9)$$

3.3.4 Experimental Results

Although all DWs were tested with varying process air inlet temperatures, inlet humidity ratios, and regeneration temperatures, only the results of the 50 mm thickness

DW were discussed in detail since the DWs showed similar trends with these three factors. In the last section, effects of DW thicknesses (30, 50, 70 and 150 mm) were examined.

The effects of the process air inlet temperature was investigated (test 1, 2 and 3) and shown in Figure 3-13. The process air inlet temperature was varied, while the inlet humidity ratio and regeneration temperature remained constant. The relative humidity of regeneration air after heater also remained constant (12 percent). As the process air inlet temperature increases, the MRC decreases as shown in Figure 3-13 (a). At a rotational speed of 50 RPH, the MRC decreases from 0.488 g·s^{-1} to 0.353 g·s^{-1}, while inlet temperature increases from 25°C to 35°C. When the humidity ratio is fixed, the vapor pressure in the process air remains constant. Higher dry bulb temperature increases the saturated vapor pressure of the desiccant. The saturated vapor pressure is the driving force for moisture transfer. Higher values of saturated vapor pressure indicate lower tendency for water vapor to condense and be adsorbed by desiccant material. Therefore, warmer air results in a reduced adsorption rate, removes less air and leads to lower MRC when the humidity ratio is fixed. Generally, there is an optimum RPH of the DW maximizing the MRC. If the rotational speed is too low, the desiccant wheel may not perform at its maximum capacity as adsorption and desorption processes already saturated before the process and regeneration areas switch. Alternatively, if the rotational speed is too high, the desiccant material cannot fully adsorb or desorb water vapor due to the short process time. As shown in Figure 3-13 (b), the COP$_{latent}$ acts similarly to MRC as rotational speed increases, but is less sensitive to inlet temperature.

As for the SER, it increases with rotational speed. This is due to the increased sensible heat transfer between the regeneration and process air streams. When the

temperature difference between the regeneration and process air streams is fixed, the sensible heat flux, which is defined as the sensible heat transfer rate per unit area, is fixed. The sensible heat transfer rate is the heat transferred per unit time, and is proportional to the product of the sensible heat flux and rotational speed. Higher rotational speed increases the sensible heat transfer rate as it increases the heat transfer areas per unit time. In other words, the high rotational speed increases the process air outlet temperature. There is no significant variation in SER with process air inlet temperatures.

The error bars are also shown for all data points. It is found that the MRC and COP have high relative uncertainties, ranging from 25 to 40 percent. The major contribution (80 to 90 percent) comes from the measurement error of relative humidity. SER only involves temperature measurement, so the relative errors are roughly 10 percent.
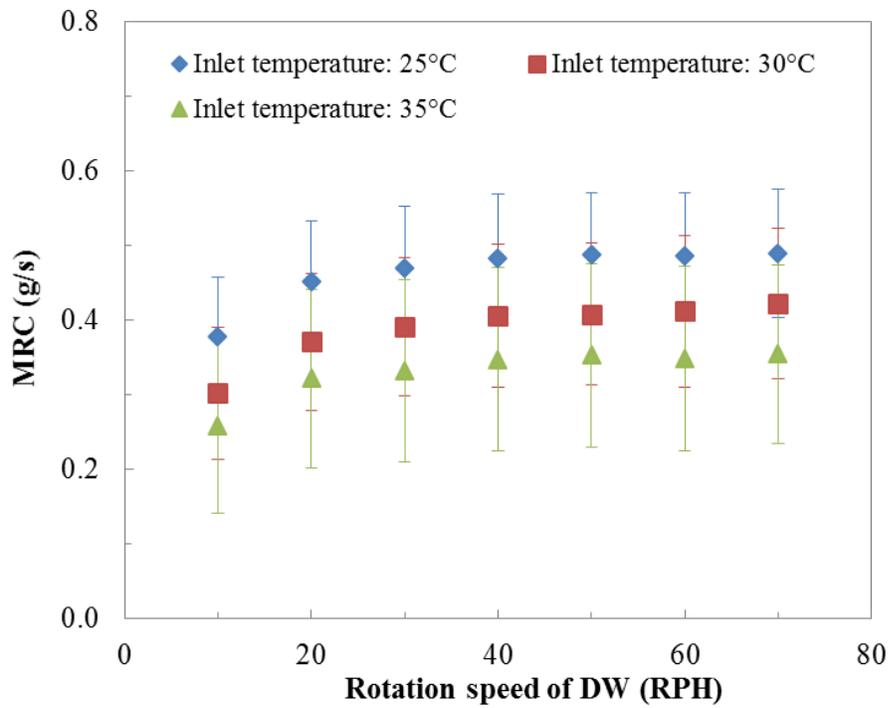
(a) Effects of inlet temperature on MRC
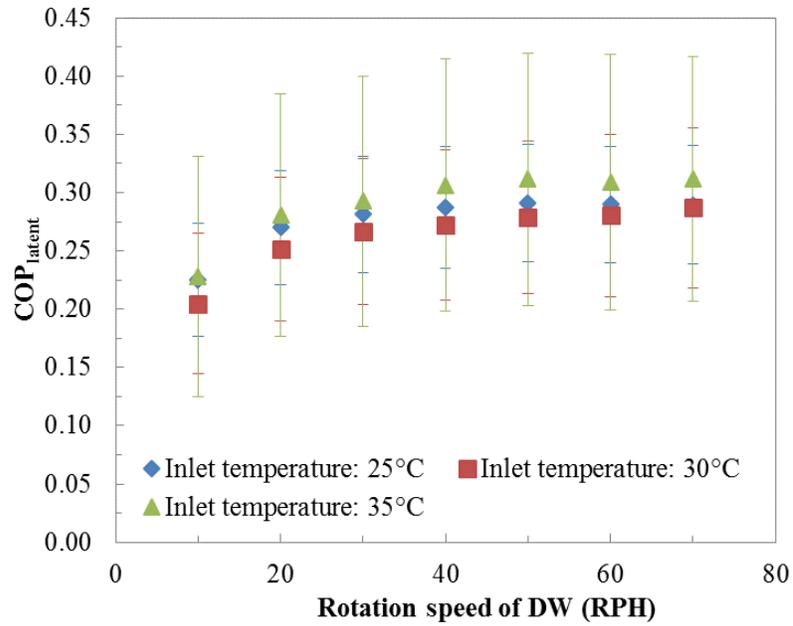
(b) Effects of inlet temperature on COP$_{latent}$
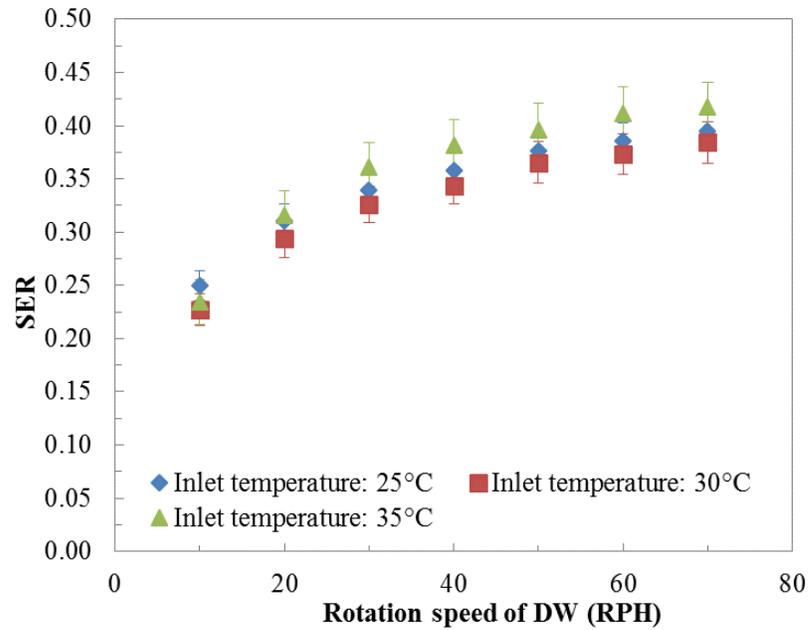
(c) Effects of inlet temperature on SER

Figure 3-13: Effects of inlet temperature and rotation speed on 50 mm DW

performance

The effect of the process air inlet humidity was investigated (tests 2, 4 and 5) as shown in Figure 3-14. The process air inlet humidity ratio varied while the inlet and regeneration temperatures were fixed at 30°C and 60°C, respectively. The relative humidity of regeneration air after it has been heated increases from 8 percent to 15 percent with increasing inlet humidity ratios. As the humidity ratio increased, the MRC increases as shown in Figure 3-14 (a). Increased humidity ratio indicates higher partial pressure of water vapor, which means higher tendency for water to condense and be adsorbed by the desiccant material, thus larger driving force for adsorption. MRC displayed similar trends with increasing rotation speeds, as discussed in Chapter 4.1. Similar to MRC, a higher latent performance is achieved at higher inlet humidity ratio. For instance, the MRC and COP_{latent} increased by 68 and 74 percent, respectively, at a rotational speed of 40 RPH when the humidity ratio increased from 10 gw·kga^{-1} to 20 gw·kga^{-1}. The SER slightly increased with rotational speed.
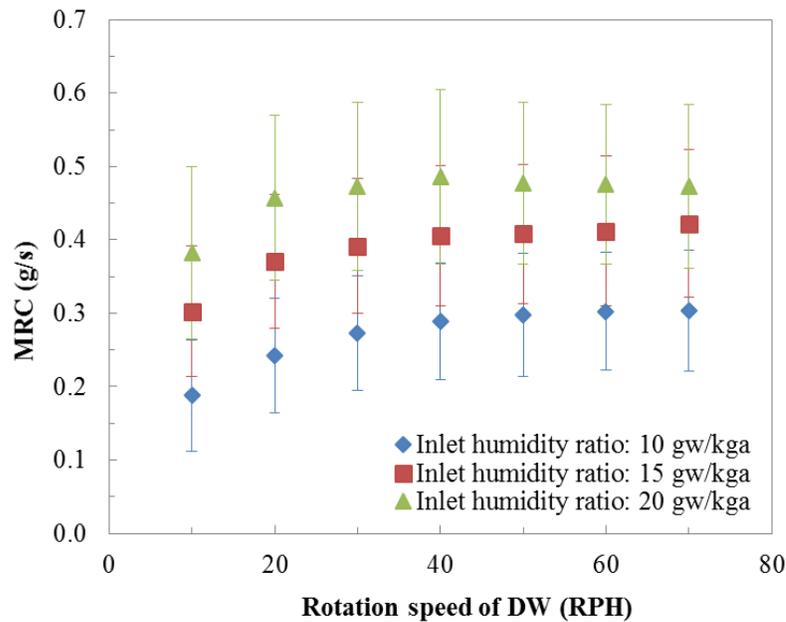
(a) Effects of inlet humidity ratio on MRC

53
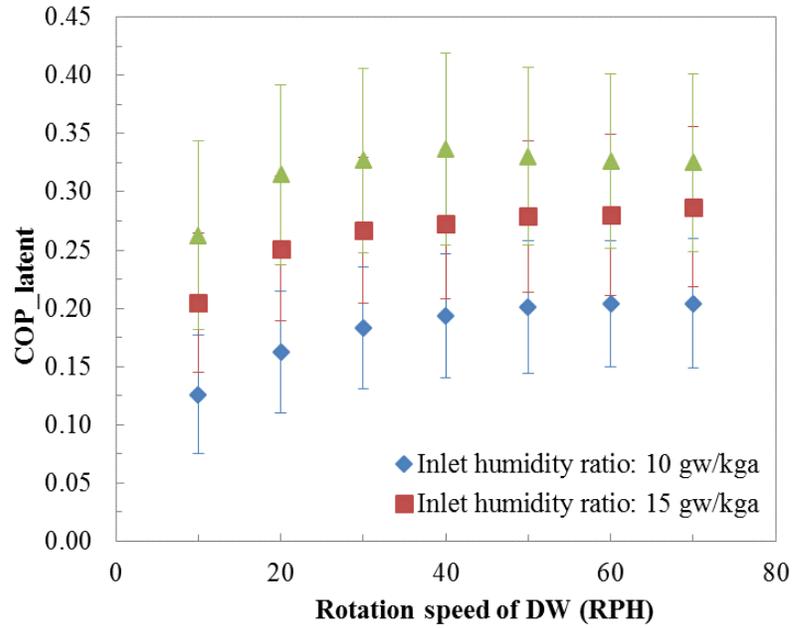
(b) Effects of inlet humidity ratio on COP_{latent}
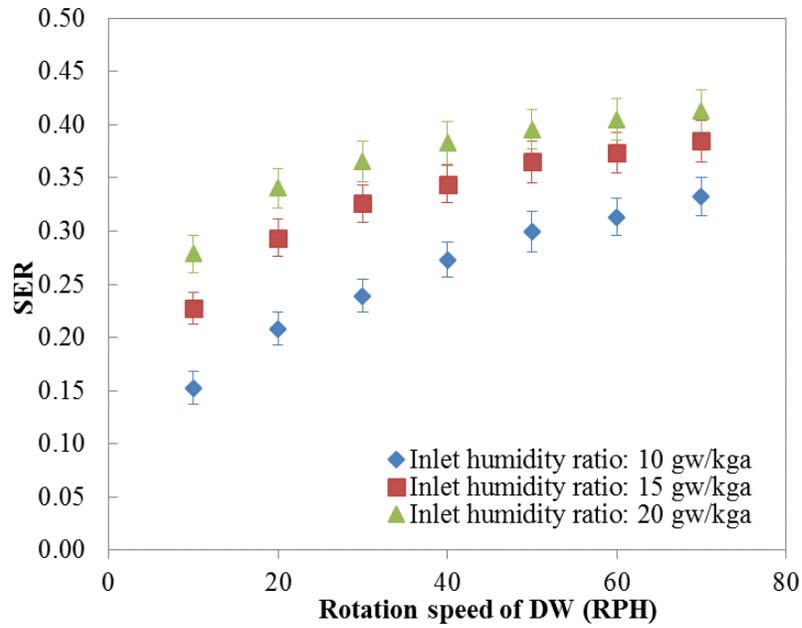
(c) Effects of inlet humidity ratio on SER

Figure 3-14: Effects of inlet humidity ratio and rotation speed on 50 mm DW

performance

The effect of the regeneration air inlet temperature was investigated (tests 2, 6 and 7) as shown in Figure 3-15. The regeneration air inlet temperature varied while the temperature and humidity ratio of inlet air remained constant. As the regeneration temperature increases, the MRC increases. Also, MRC increase slows down at higher regeneration temperature. As an example, at 10 RPH, MRC increase from 50°C to 60°C is only about 60 percent of that from 40°C to 50°C. For the COP_{latent}, as the regeneration temperature decreases, the desiccant latent performance increases because the MRC increases at a rate lower than that of the regeneration temperature.

The sensible effectiveness decreases with regeneration temperature. Although higher regeneration temperature results in higher process outlet air temperature, the SER decreases due to larger difference between regeneration and process inlet temperatures. The SER reaches its saturated state at a low regeneration temperature and a high rotational speed since heat transfer through adsorption and desorption processes reach its maximum rates.

As discussed before, higher regeneration temperature resulted in higher MRC but lower COP_{latent}. A high regeneration temperature resulted in a reduced marginal benefit, with respect to the latent performance. In the testing, a 50°C regeneration temperature is the optimum working condition because it can provide good MRC and COP_{latent} simultaneously. A 50°C heat source can be obtained through a solar thermal collector or waste heat from an engine and considered as low degrade heat.
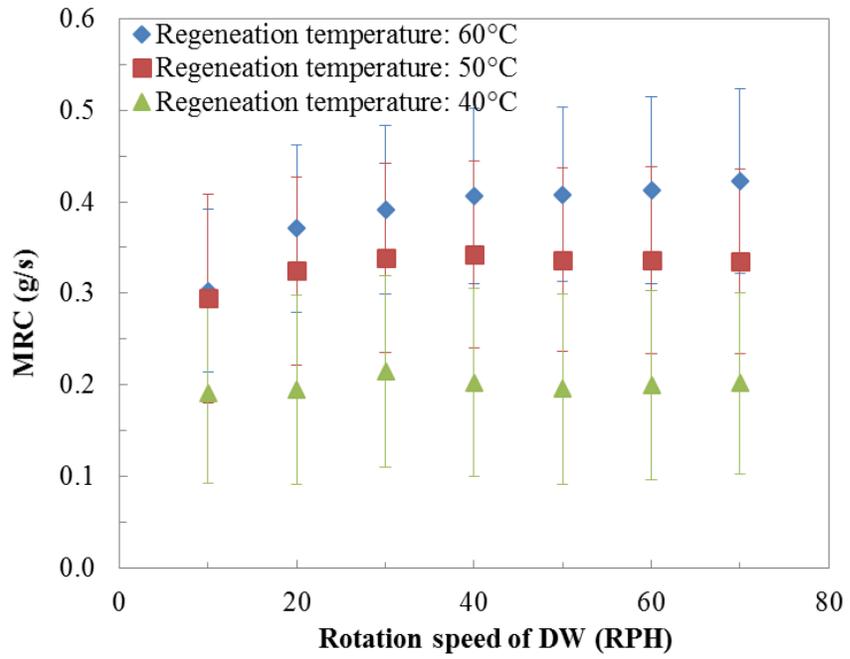
(a) Effects of regeneration temperature on MRC
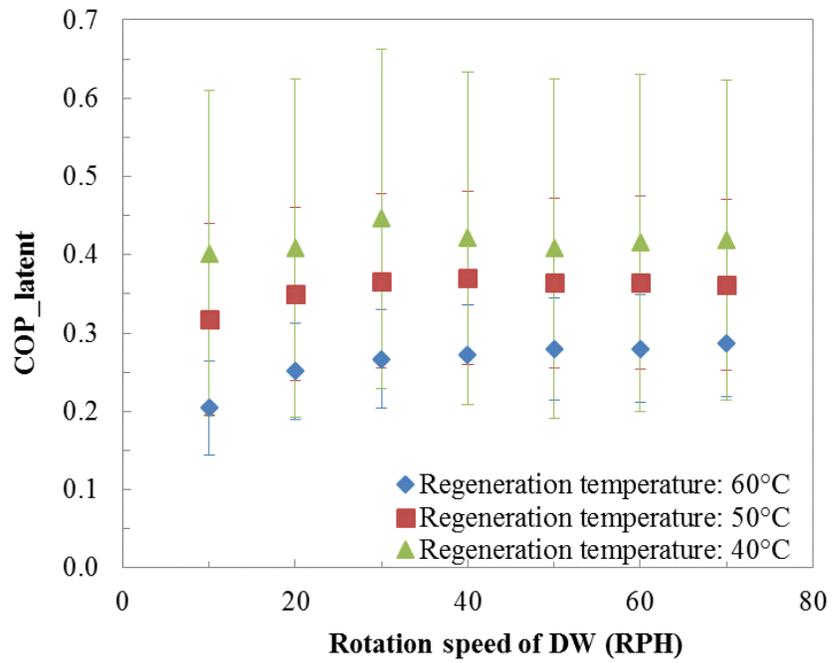
(b) Effects of regeneration temperature on COP$_{latent}$
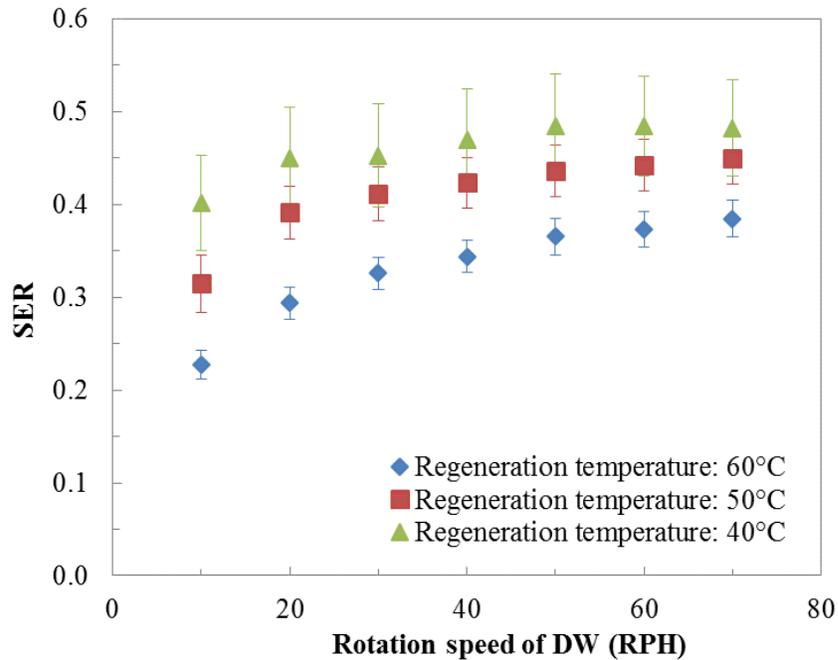
(c) Effects of regeneration temperature on SER

Figure 3-15: Effects of regeneration temperature and rotation speed on 50 mm DW performance

In this section, the focus is the effect of different DW thickness. Test 5 condition (process air inlet temperature 30°C, inlet humidity ratio 20 gw·kga^{-1}, regeneration temperature 60°C) was selected for all DWs. As the DW thickness increased, the MRC can be expected to increase. In order to reach full potential in capacity, the DW has to rotate slowly enough to provide a sufficient amount of time for adsorption and desorption processes, which are essential for moisture transfer from the process air to the regeneration air. This explains why DWs peak earlier in MRC with increasing thicknesses, as shown in Figure 3-16 (a). For instance, 150 mm MRC peaks at 10 RPH, while 30 mm peaks at 70 RPH. The COP$_{latent}$ displays similar trends with rotational speed for each desiccant wheel and with increased thicknesses, as shown in Figure 3-16 (b). Increased thickness means the

DW can hold more heat from the regeneration air, thus allows more heat transfer between

the process and the regeneration air streams. Therefore, the SER increases with thicknesses.
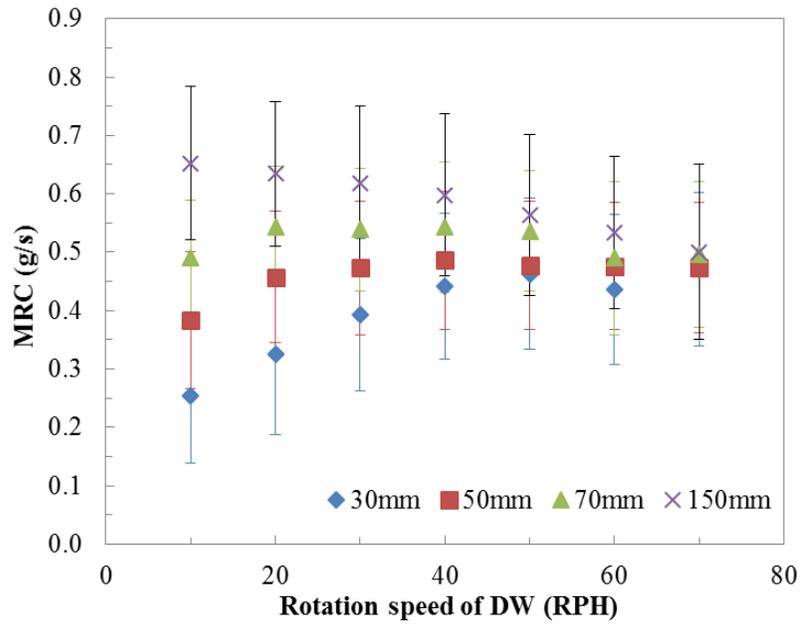
(a) Effects of thickness on MRC
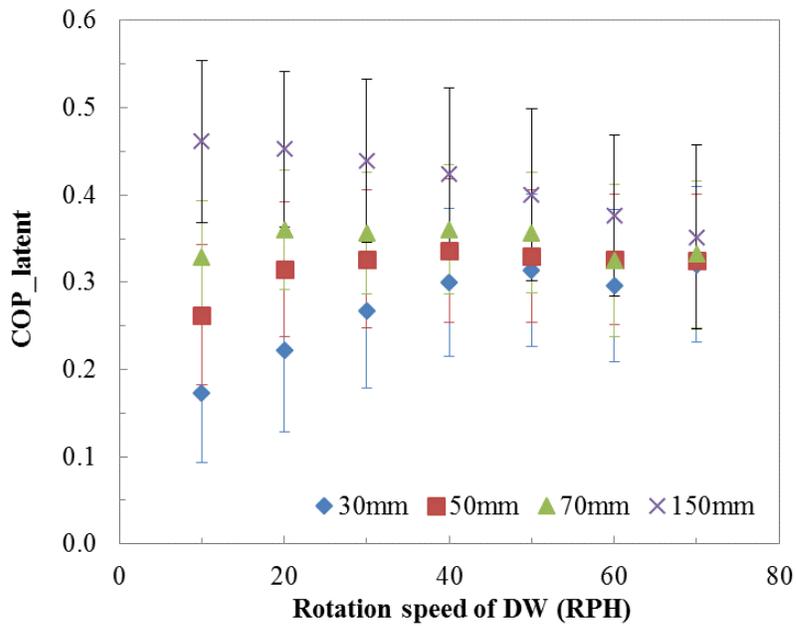
(b) Effects of thickness on COP$_{latent}$

58
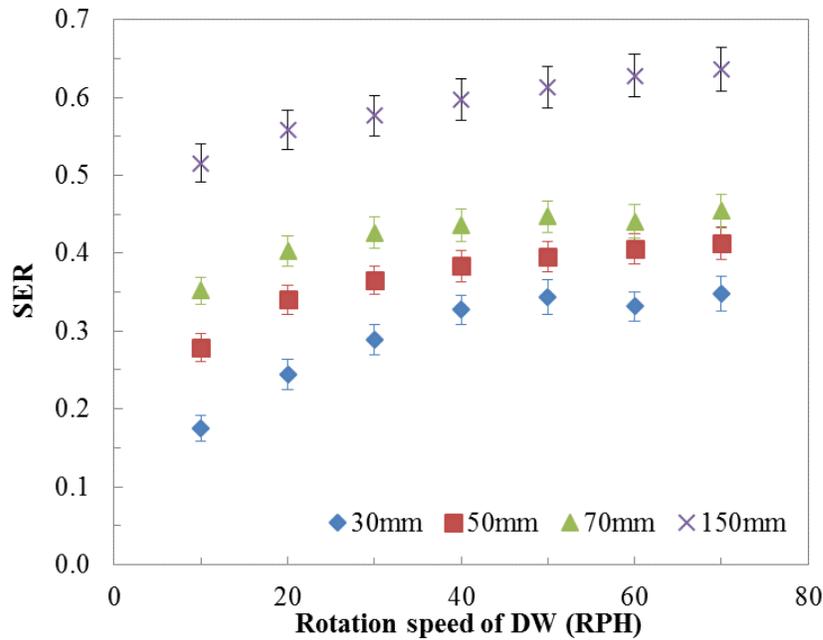
(c) Effects of thickness on SER

Figure 3-16: Effects of thickness and rotation speed on DW performance

Table 3-11 shows the maximum MRC, COP_{latent}, minimum SER and pressure drop across DW for all four DWs. The corresponding conditions are also listed in the order of rotational speed, process air inlet temperature, humidity ratio and regeneration temperature. As discussed before, the maximum MRC and COP_{latent} increase with thicknesses. The SER also increases rapidly with thickness. While this is not the major concern for the DW operation, it could be one of the main issues in integrated cooling and dehumidification system design. When the process inlet and regeneration temperature are fixed, higher SER leads to higher process outlet temperature. Thus higher sensible cooling load is added by the DW in the dehumidification process. The DW is typically used in the hybrid cooling system to handle the latent cooling load. As a result, the device located in the downstream of DW, which is usually a vapor compression chiller, can be used to handle only sensible

cooling load. The extra sensible cooling load created by the DW is not desired and increases the amount of the workloads for vapor compression chiller. Thus the whole system requires more power input. Moreover, increasing thickness means a significant pressure drop across the DW, thus an increased demand for the fan power. The air-side pressure of 150 mm DW was twice of 50 mm DW.

Table 3-11: Maximum MRC and COP for all DWs

Indices	30mm DW	50mm DW	70mm DW	150mm DW
MRC_{max} (g·s^{-1})	0.474 (at 70RPH, 25°C, 15 gw·kga^{-1}, 60°C)	0.490 (at 70RPH, 25°C, 15 gw·kga^{-1}, 60°C)	0.544 (at 20RPH, 30°C, 20 gw·kga^{-1}, 60°C)	0.664 (at 20RPH, 25°C, 15 gw·kga^{-1}, 60°C)
MRC_{max}/Volume (g· s^{-1}·m^{-3})	224	139	110	63
COP_{latent_max}	0.381 (at 70RPH, 30°C, 15 gw·kga^{-1}, 40°C)	0.446 (at 30RPH, 30°C, 15 gw·kga^{-1}, 40°C)	0.482 (at 30RPH, 30°C, 15 gw·kga^{-1}, 40°C)	0.591 (at 10RPH, 30°C, 15 gw·kga^{-1}, 40°C)
SER_{min}	0.079 (at 10RPH, 30°C, 10 gw·kga^{-1}, 60°C)	0.153 (at 10RPH, 30°C, 10 gw·kga^{-1}, 60°C)	0.211 (at 10RPH, 30°C, 10 gw·kga^{-1}, 60°C)	0.388 (at 10RPH, 30°C, 10 gw·kga^{-1}, 60°C)
Pressure drop across DW (Pa)	59	70	100	140

Overall, the thin DWs have the potential to be used in compact dehumidification and cooling systems while satisfying COP_{latent} with lower SER and pressure drop. For example, maximum COP_{latent} for 50 and 70 mm DWs are 0.446 and 0.482, respectively while the expected COP_{latent} of DW system is 0.5. Furthermore, 50 and 70 mm DWs can reduce the pressure drop by 50 and 30 percent, respectively. When viewed on the specific volume basis, the thin DWs outperform the thick DW. For instance, the maximum MRC based on the specific volume of the 50 mm DW is 1.2 times higher than that of 150 mm DW. The reason is that the relative humidity decreases along the DW, thus the dehumidification capacity of the desiccant becomes lower. In other words, for a thick DW, the downstream part of the thick DW does not perform well as the upstream part.

For each DW, the MRC and COP usually reach their respective maximum points at different working conditions as indicated in Table 3-11. For instance, the 50 mm DW has maximum MRC at 25°C process inlet temperature, 15 $gw \cdot kga^{-1}$ inlet humidity ratio and 60°C regeneration temperature, while the maximum COP is obtained at 30°C process inlet temperature, 15 $gw \cdot kga^{-1}$ inlet humidity ratio and 40°C regeneration temperature. This means that when designing a desiccant wheel system, one should be cautious about the optimum working conditions, and a balance between the MRC and COP should be considered.

3.3.5   *High Humidity Performance Investigation*

Dehumidification is most needed under high humidity conditions, which is common weather conditions for sea routes. Therefore, it is interesting to investigate the desiccant wheel performance under high humidity conditions. Table 3-12 shows the test matrix under high humidity conditions. The inlet air relative humidity was set to be 0.9. Only 70mm desiccant wheel was selected as it is enough to show the impacts of high humidity on the desiccant wheel performance. Impacts of flow rate were also studied with two different flow rates.

Table 3-12: Test matrix for high humidity conditions

No	Desiccant wheel mm	T_{in} °C	W_{pin} gw·kga^{-1}	W_{rin} gw·kga^{-1}	Volume flow rate m^3·hr^{-1}	T_{gen} °C	R_{speed} RPH	Run min
1		25	18	18		40		30
2	70	25	18	18	200	50	10 to 70 with 10 of step	30
3		25	18	18		60		30
4		25	18	18	350	60		30

Figure 3-17 (a), (b) and (c) show impacts of regeneration temperature on MRC, COP$_{latent}$ and SER under high humidity condition, respectively. Same trends are observed with increasing regeneration temperatures and rotation speeds, as discussed in previous chapter. Highlights are that under high humidity conditions, the maximum MRC has increased to 0.6 g/s from 0.54 g/s from previous tests. The maximum COP$_{latent}$ has increased from 0.482 to 1, which is well above most common desiccant wheel performances as 0.5. Therefore, a general conclusion is that performances of desiccant wheels are greatly improved under extremely high humidity conditions. For thin desiccant wheel whose performance is worse than thick ones under mild humidity conditions, its performance could be well above standard levels. Thus it may be promising to be used for ship applications. Effects of flow rate is not shown here as it is clear that higher flow rate leads to high moisture removal capacities, though it is the same on per unit mass flow rate basis.
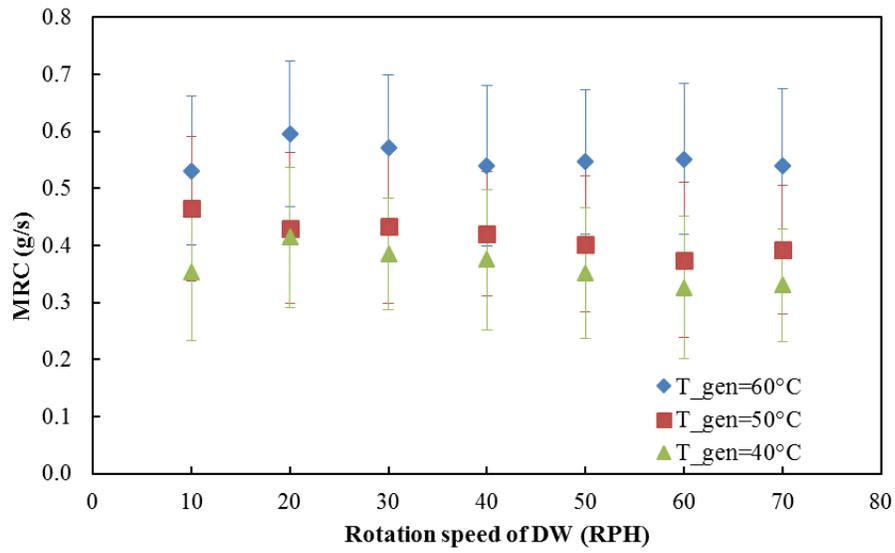
(a) Effects of regeneration temperature on MRC
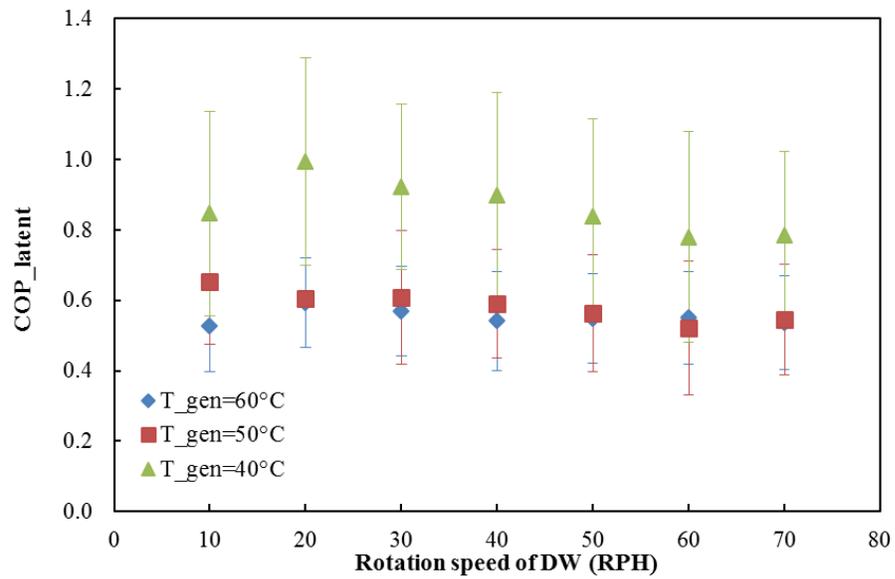
(b) Effects of regeneration temperature on COP$_{latent}$
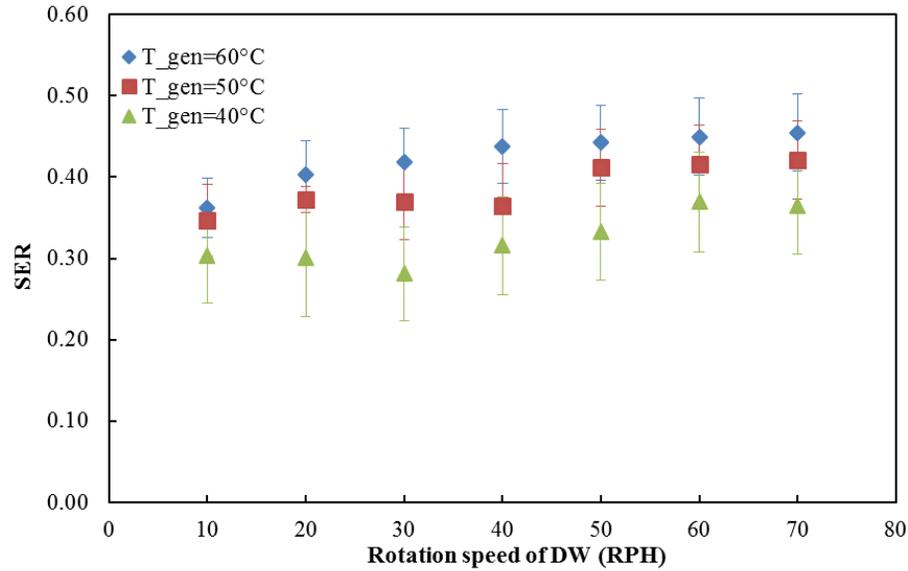
(c) Effects of regeneration temperature on SER

Figure 3-17: Effects of regeneration temperature and rotation speed under high humidity conditions

3.3.6 Desiccant Wheel Model Development

Desiccant wheels play key roles in dehumidification process. It can be used as a standalone dehumidification equipment or combined with vapor compression chiller as a separate sensible latent cooling system. Either way it is interesting to explore benefits of applying desiccant wheels in microgrid energy systems. Therefore, desiccant wheel models need to be developed.

Table 3-13 summarizes available desiccant wheel modeling approaches. There are physical based desiccant wheel models developed recently, as presented chapter 3.3.1. Usually these models require extensive knowledge on material properties and desiccant wheel dimensions. However, these information are not easy to obtain for any desiccant

wheels. Therefore, it is not applicable for general performance prediction models. Alternatively, one may refer to correlation or performance map based models to avoid physical details. There are two types of model available from TRNSYS. However, both have limitations. One is only applicable to silica gel materials and the other only accepts one regeneration temperature.

Table 3-13: Desiccant wheel modeling approaches

Modeling Approach	Model Type	Comments
Detailed Physical Based Model	Physical Based	Requires extensive inputs of desiccant material properties
TRNSYS Type 716 Type 1716a/b	Correlation Based	Only applicable to silica gel
TRNSYS Type 1225	Performance Map	Only accept one regeneration temperature
Model based on the author's experimental study	Performance Map	Covers extremely high humidity conditions

Hence the desiccant wheel model was developed based on the author's experimental study, which provides extensive data on polymer desiccant wheels, particularly under high humidity conditions for real sea route conditions. A performance map was developed based on the experimental data. Details of the performance map is summarized in Table 3-14. The performance map assumed the mass flow rate of process air steam and regeneration air stream are the same. The performance map was then integrated into TRNSYS program.

Table 3-14: Details of desiccant wheel performance map

Input	Min	Max	Output
T_p_in (°C)	24.4	35.1	T_p_out (°C)
RH_p_in (%)	39.1	97.4	RH_p_out (%)
T_r_in (°C)	37.6	61.6	T_r_out (°C)
RH_r_in (%)	7.8	44.6	RH_r_out (%)
MFR (kg$\cdot$hr^{-1})	229	450	Pressure drop (Pa)
Rotation Speed (RPH)	10	70	

3.4 Summary

In this chapter, several components were modeled and studied to provide basis for dynamic microgrid system modeling. Specifically, a novel absorption cycle model was developed accounting for real operation constraints and validated against data from open literature. Meta-model was developed for vapor compression refrigeration units. A novel sea route weather model capable of predicting hourly sea rout weather was developed. Main engine and waste heat model was set up with engine manuals. Detailed shipboard living space model was also developed with manufacture specifications.

The performance of the new polymer desiccant material was investigated experimentally. This desiccant material can be regenerated using a low temperature heat source like 50°C. The effects of the process air stream's temperature and humidity, the regeneration temperature, the desiccant wheel's rotational speed and the DW thickness were investigated. Desiccant wheels were also investigated under extremely high humidity conditions for sea route climates. It was found that thin polymer desiccant wheel (70 mm) was able to increase its performance above standard levels, with a COP_{latent} as 1. A new desiccant wheel model was developed based on experimental data.

4 Microgrid System Dynamic Modeling

4.1 Solar Energy Powered System

4.1.1 Background

Traditionally, the cruise ships heavily rely on diesel engine for propulsion and other energy uses. In cruise ships, the heating, ventilation and air conditioning (HVAC) systems are responsible for the second largest power consumption, which usually consumes 30% of the total onboard installed power. Currently the cooling system mostly relies on the VCC technology, which requires the electricity from diesel combustion to power up. Therefore, the hybrid cooling system, which utilizes either renewable energy resources (e.g. solar and wind energy) or waste heat onboard (e.g. exhaust gas, air cooler and jacket water) to power up the cooling systems, can greatly reduce the fuel consumption and improve the ship efficiency. Furthermore, the cruise range could be increased since the more fuel could be used for the propulsion purpose.

Although there have been a number of studies conducted on hybrid cooling systems, very limited studies were specifically focused on cruise ship applications. Garimella et al. [96] proposed a waste heat driven absorption/vapor compression cascade refrigeration system for navy ships. The system was modeled with Engineering Equation Solver (EES). The estimated system COP was 0.6 and consumed 31% less electricity compared with an equivalent two-stage VCC. Liang et al. [97] simulated an electricity-cooling cogeneration system using the EES. The system was a combination of Rankine cycle and absorption cycle. It was reported that the useful output of the whole system was increased by 9%. Ouadha [98] studied the integrated system of ammonia-water refrigeration with marine

67

diesel engine. All components were analyzed by the first law of thermodynamics. From the literature review, it was found that there are only limited studies on hybrid cooling system for marine sectors. Also most studies were based on steady state simulation. However, the ships were usually operated under transient ambient conditions. Therefore, the study on the long term performance under varying weather conditions is of great interests and importance.

In order to address these deficiencies, this chapter investigates the solar energy powered hybrid cooling systems under transient conditions. There are two options for solar powered cooling system. One is PV powered vapor compression cycle. The other is ETC powered absorption cycle. The goal of this study is to simulate the solar powered hybrid cooling system under transient weather conditions, and evaluate their performance and potentials in fuel reductions. Transient systems simulation program (TRNSYS) is a convenient tool to simulate an energy system under transient conditions and was used in this study.

The Oasis of the Seas, the world's 2nd largest cruise ship was selected for the study. It was reported that this cruise ship already installed 2,000 m^2 PV panels to meet part of the power demands [99]. Therefore, 2,000 m^2 was assumed to be the available deck area for PV panels or ETC installation. Typical guest room volume is 40 m^3. In this study, the building model volume was set as 47,756 m^3, which contains about 1,194 guest rooms, about the half of the total guest rooms on the Oasis of the Seas. The TMY2 weather data for Miami, Florida was chosen for the simulation purpose since the cruise ship is operated between Miami and Bahama. The ventilation rate of cooling air was set to be 0.3 L·(s·m^2)$^{-1}$ based on ASHRAE standard on ventilation flow rate for hotel rooms [100]. The

simulation time of all systems was set as 8,640 hours, which is one year. Generators were used in all three scenarios. It was assumed that the generators were all powered by diesel fuels. The fuel consumption rate of the generators was 0.23 kg·(kW·hr)$^{-1}$ [101].

4.1.2 System Configurations

In this part, the model developed for the PV powered VCC system is described. Battery cell stacks were used as power storage systems. Figure 4-1 shows the flow chart of PV system model. The power generated by PV is in direct current (DC). However, the vapor compression chiller requires alternating current (AC) input. Therefore, an inverter is used to convert the DC power into AC with appropriate frequency. The AC power is then provided to the vapor compression chiller to produce chilled water. The chilled water cools down the cabin air through a water-to-air heat exchanger. The cooled air is then ventilated to the desired cooling spaces.

The battery stacks start with uncharged. Therefore, at the beginning the power from the inverter charges the batteries first. Once the stacks were fully charged, the chiller always has higher priorities in using power from the inverter. Charging the battery begins only when the chiller demands have been met. At night, when the PV panel no longer works, the batteries stacks discharge to the inverter, and then supply power to the chiller. Whenever there is no enough power to meet the chiller demands, the generators is used as a supplementary option.

The control strategy of the whole system was set up. The thermostat monitors the zone temperature of the building model all the time. When the zone temperature is higher

than the set cooling point temperature (24°C), the chiller and fan are turned on. When the zone temperature is lower than the set point, the chiller and fan are turned off.

The detailed description of the components used in TRNSYS simulation of the whole system is provided in Table 4-1.
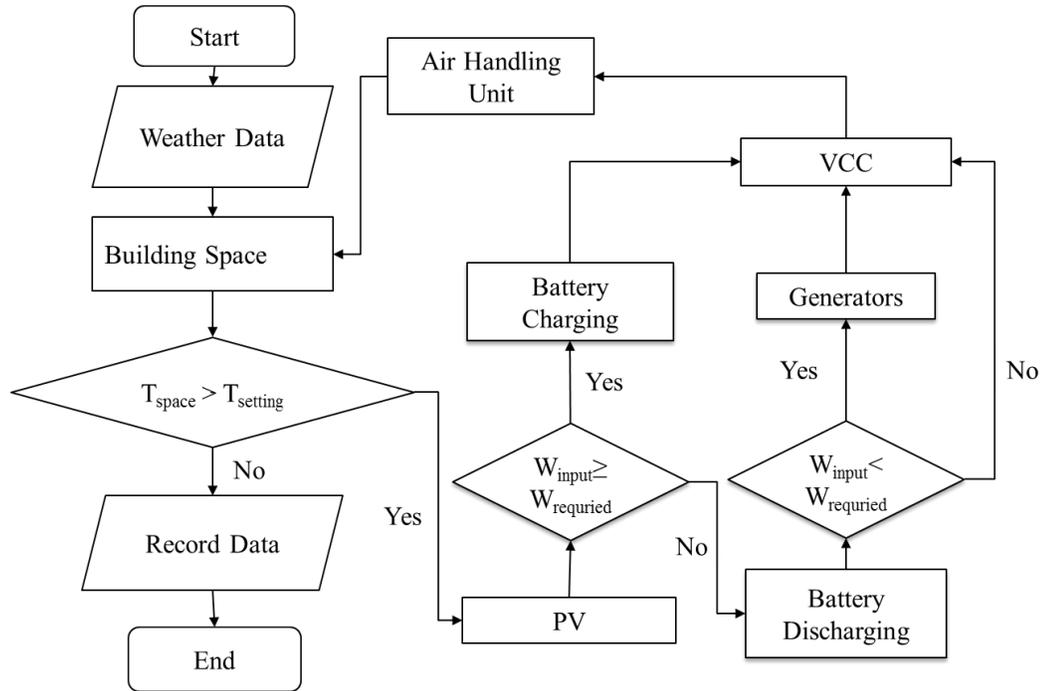
Figure 4-1: Flow chart of the PV system model

Table 4-1: Details of the components in PV system

Component	Parameter	Value
Multi-zone building model	Capacitance of zone	57,307 kJ·K^{-1}
	Volume	47,759 m^3
PV Panel	Efficiency	0.12
	Area	1.0 m^2
Regulator and inverter DC/AC	Regulator efficiency	0.78
	Inverter efficiency	0.96
Electrical storage	Cell energy capacity	16.7 Ah
	Charging efficiency	0.9
	Max. current per cell charging	3.33 A
	Max. current per cell discharge	-3.33 A
	Max. charge voltage per cell	2.5 V
Vapor Compression Chiller	Rated capacity	351.7 kW
	Rated COP	3
	Chiller water flow rate	50,000 kg·hr^{-1}
	Chiller water set point temperature	6.67°C
Thermostat	Temperature dead band	2°C
	Cooling set point	24°C
Fan	Maximum flow rate	30,948 kg·hr^{-1}
	Maximum power	86.0 kW
Pump	Rated flow rate	50,000 kg·hr^{-1}
	Rated Power	37.3 kW

In this part, the ETC powered ABC system model is described. Water tanks were used as heat storage system. Figure 4-2 shows the flow chart of ETC system model.

Start

Weather Data

Building Space

Air Handling Unit

ABC

Pump

Water Tank ← Generators

$T_{space} > T_{setting}$

Yes

No

Record Data

$W_{input} \geq W_{requried}$

Yes

No

End

ETC
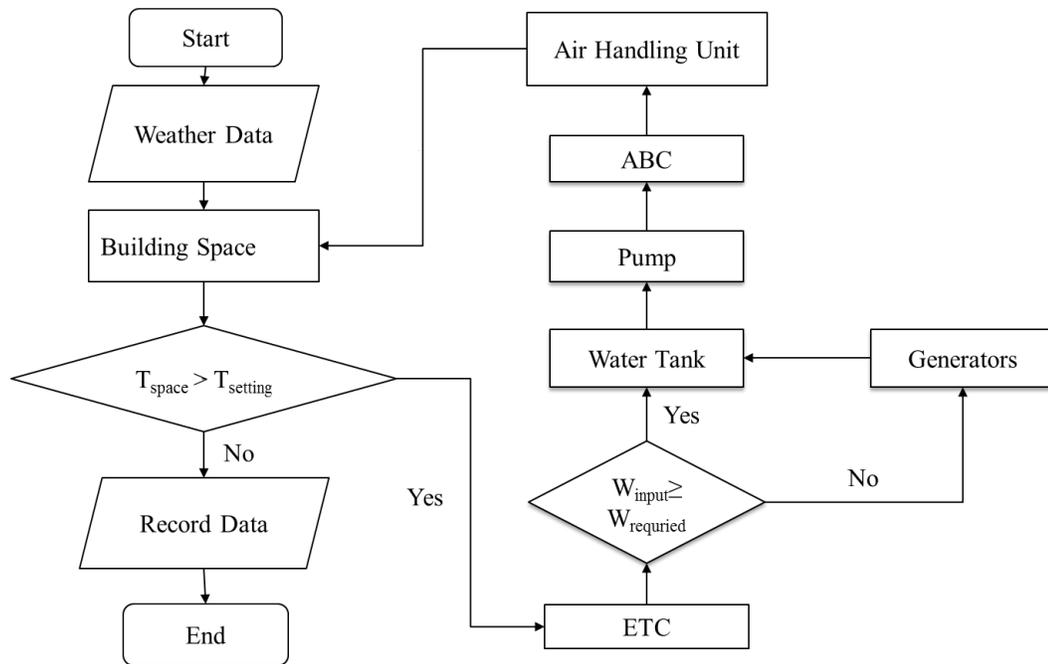
Figure 4-2: Flow chart of the ETC system model

The pump circulates the water to the ETC, in which the water is heated up. The water is then sent to the water tank. The water tank contains internal heater in case additional power is required to maintain certain hot water temperature. The hot water coming from the water tank is then supplied to the generator of the ABC. The ABC produces cooling energy carried by chilled water. The chilled water cools down the cabin air through a water-to-air heat exchanger. The cooled air is then ventilated to the desired cooling spaces.

The control strategy of the whole system was set up. The pump keeps circulating water to the solar thermal collector every day from 8 a.m. to 6 p.m. The thermostat monitors the zone temperature of the building model all the time. When the zone temperature is higher than the set cooling point temperature (24°C), the fan is turned on and the pumps

circulate hot water from hot water tank to the generator of ABC. When the zone temperature is lower than the set point, the pump and fan are turned off.

The detailed descriptions on the components used in TRNSYS simulation of the whole system are provided in Table 4-2. The absorption cycle model (Type 223) was developed by Wei et al. [102]. The component utilizes approach temperatures to model the absorption cycle with LiBr-H$_2$O as its working fluid. The modeling results were compared with EES modeling results with good agreements.

Table 4-2: Details of components in ETC system

Component	Parameter	Value
Multi-zone building model	Capacitance of zone	57,307 kJ·K^{-1}
	Volume	47,759 m^3
ETC (Evacuated thermal collector)	Collector Area	2 m^2
Thermal storage tank	Tank volume	3.5 m^3
	Water specific heat	4.19 kJ·(kg·K)$^{-1}$
	Water density	1,000 kg·m^3
	Tank loss coefficient	3 kJ·hr^{-1}·m^2·K
	Number of nodes	10
	Height of each node	0.05 m
	Boiling point	100°C
Absorption cycle	Coolant	Water
	Chilled water temperature	6°C
	Effectiveness of SHX (solution heat exchanger)	0.8
Water to air heat exchanger	Air specific heat	1.005 kJ·(kg·K)$^{-1}$
	Heat exchanger effectiveness	0.8

4.1.3 Results Analysis

All systems were simulated for one year (8,640 hours) and achieved space cooling targets. Figure 4-3 shows the ambient and zone temperature profiles of the PV system in

yearly basis. The other two systems exhibit exactly the same curves. The red curve is the ambient temperature, and the blue one is zone temperature. As can be seen, the zone temperature is fluctuating between 22 and 24.7°C when ambient temperature is higher than 24°C. While for winter times (the beginning and ending parts), the cooling system is not operated as the ambient temperature is below 24°C. Moreover, the heating mode is not considered in this simulation program. Therefore, the zone temperature is very close to ambient temperature.
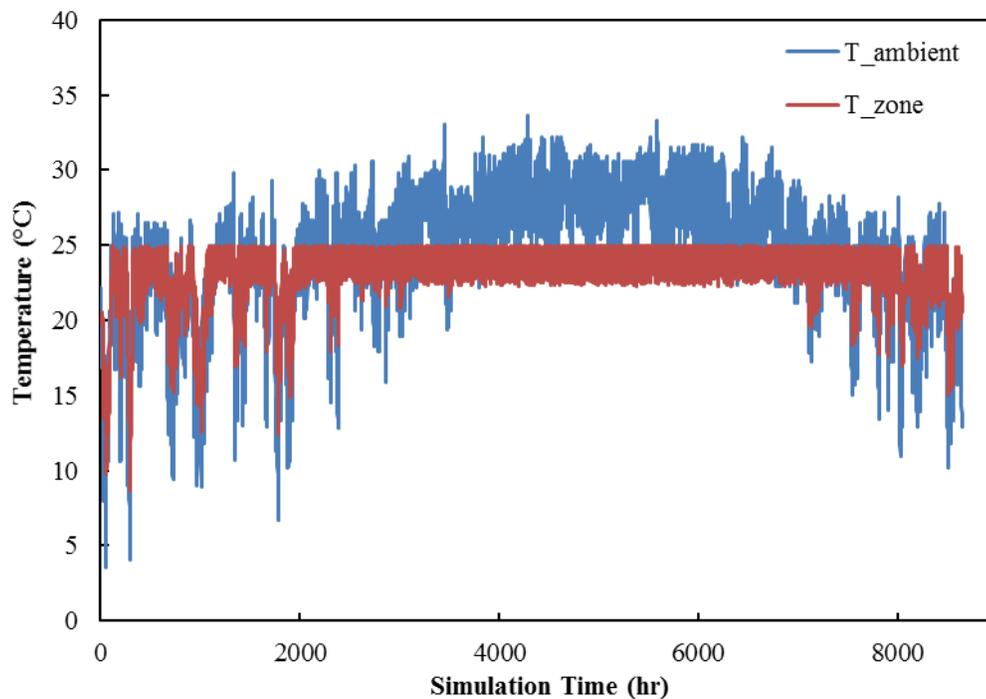
Figure 4-3: Yearly temperature profiles of the PV system

Several indices were used to evaluate the system performance. The first one is solar power fraction, which is defined in Equation (4-1). The higher the solar power fraction, the more power is provided by the PV panels or ETC, instead of the generators. Therefore, the higher solar power fraction is in favor of fuel reduction.

$$\text{Solar Power Fraction} = \frac{\text{Power supplied from PV or ETC}}{\text{Total power demanded by the chiller}} \qquad (4\text{-}1)$$

The second one is the yearly performance factor and defined in Equation (4-2). It indicates how much energy is needed to deliver desired cooling capacity on the yearly basis. Higher yearly performance factor means better system performance.

$$\text{Yearly Performance Factor} = \frac{\displaystyle\int_{0}^{8640} \text{Cooling capacity } dt}{\displaystyle\int_{0}^{8640} \left(\text{Solar radiation} + \text{Generator power} + \text{Pump power} + \text{Fan power}\right) dt}$$

$$(4\text{-}2)$$

The last one is the PV utilization fraction as shown in Equation (4-3). There are times that PV produces excessive power than the chiller demands and the battery is fully charged. In such case, the excessive power is dumped by the system. It is considered as undesirable loss for the system. Therefore, higher PV utilization fraction means the less power is lost by the system.

$$\text{PV Utilization Fraction} = 1 - \frac{\text{Dumped PV power}}{\text{Total power produced by PV arrays}} \qquad (4\text{-}3)$$

The battery system within the system is of great interests for parametric study as the size of the battery system affects the whole system performance and cost greatly. The solar power fraction, yearly performance factor and PV utilization fraction were used for the parametric study. The goal here was to select the optimum battery stack size, which has high values in all three indexes.

Figure 4-4 shows how the above three performance indices change with increasing battery capacities. The x axis is in logarithmic scale to better illustrate the trends. As can be seen, the solar power fraction increases with increasing battery size in the beginning, and then decreases after reaching a maximum point. The yearly performance factor has minor changes throughout all battery sizes. The reason is that the solar radiation is the dominant factor compared to the other three energy consumption terms in the yearly performance factor, and the solar radiation remains constant regardless of battery sizes. The PV utilization fraction increases rapidly with bigger battery size. This is expected as bigger battery size means more capacity for the storage of power produced by PV panels. The optimal point is determined to have 38,400 battery cells in total. The solar power fraction, yearly performance factor and PV utilization fraction are 0.98, 0.33 and 0.47, respectively. The solar power fraction and yearly performance factor reach maximum at this point. While bigger battery size improves the PV utilization fraction, it is not recommended for two reasons: first, the solar power fraction and yearly performance factor decrease, and second, larger battery size results in higher weight and cost, which is discussed next.
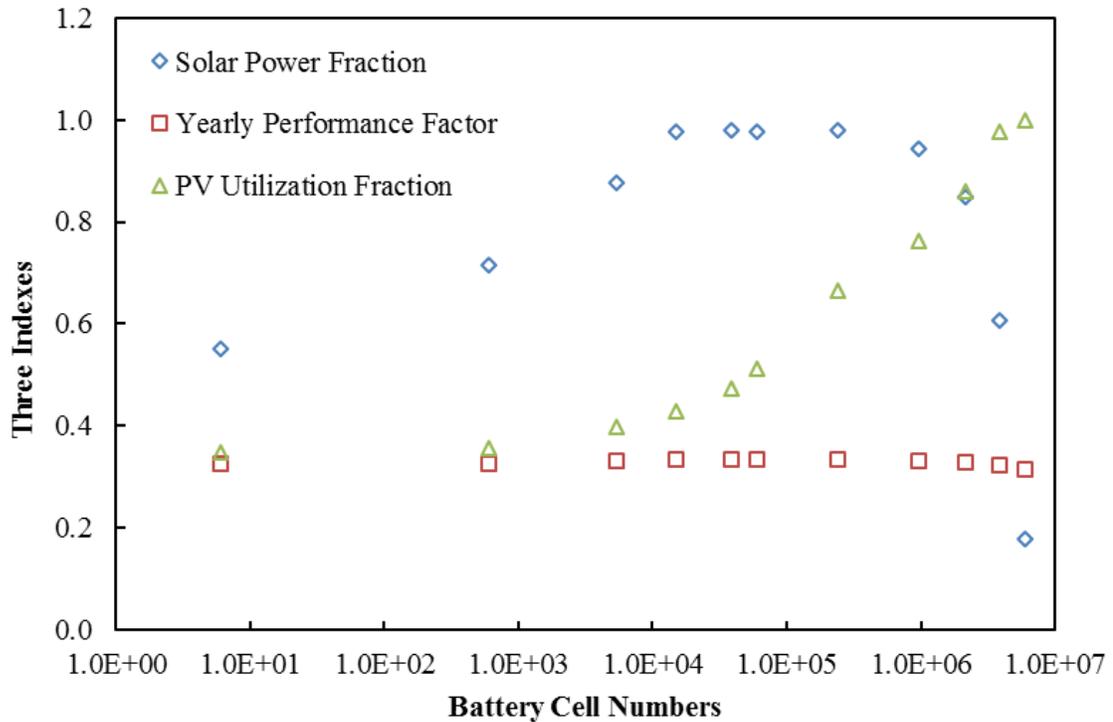
Figure 4-4: Battery size parametric study for PV system

As stated before, the diesel generators powered VCC system was considered as the baseline. The PV system and ETC system were compared with the baseline to see their performance differences. Table 4-3 shows the performance comparisons among the three systems. For the solar PV system, there are two cases considered. The first one doesn't have battery storage system. The second one has the optimum battery size – 38,400 cells.

Considering the performance, the optimized PV system has the better performance than the ETC system. The power fraction and yearly performance factor of the ETC system are 0.78 and 0.30, respectively, a little lower than that of the optimized PV system – 0.98 and 0.33.

As described in the introduction parts, one of the major goals for proposing the solar powered hybrid cooling system is to reduce the electricity produced by fuel.

Therefore, it is necessary to evaluate the abilities of the solar cooling systems to reduce fuel consumption. Table 4-3 shows that the yearly fuel consumption of all scenarios. The PV system without batteries can reduce the fuel consumption by 55%, while the optimized PV system can reduce it by 98%. For ETC system, this value is 78%. By reducing the fuel consumption, the weight and volume of fuel tank are reduced. However, adding the battery storage system or water tanks adds weight and volume to the facility compartment of the cruise ship. Therefore, it would be interesting to investigate the net weight and volume gain by introducing solar powered system. As Table 4-3 shows, the optimized PV system reduces the overall volume by 9.4 m^3 but adds 4,817 kg more mass to the ship due to the high density of batteries. For the ETC system, it can reduce the weight by 6,788 kg.

The greenhouse gas (GHG) emissions, as stated before, is also a major concern for ships. Table 4-3 also presents the life time GHG emissions of all scenarios. All systems were assumed to operate for 20 years, which are typical life time of PV or ETC system. It is shown that the optimized PV system and ETC system could reduce GHG emissions by 93% and 75%, respectively.

Table 4-3: Performance comparisons of three systems

System Option	Generators + VCC	PV + Battery + VCC		ETC + ABC
		No Battery	PV in optimized size	
PV or ETC Area (m^2)	N/A	2,000	2,000	2,000
Number of Battery Cell	N/A	N/A	38,400	N/A
Cooling Cycle Efficiency (VCC/ABC)	4.6	4.6	4.6	0.82
Solar Power Fraction	0	0.55	0.98	0.78
Yearly Performance Factor	4.6	0.32	0.33	0.30
PV Utilization Fraction	N/A	0.35	0.47	N/A
Fuel Consumption ($kg \cdot year^{-1}$)	13,500	6,060	269	2,960
Net Weight Gain (kg) [103] [104]	N/A	-7,437	4,817	-6,788
Net Volume Gain (m^3) [103] [104]	N/A	-8.8	-9.4	-9.0
GHG Emissions (ton CO_{2eq}) [105]	984	496	73.5	242

Table 4-4 shows the cost analysis of all four scenarios. The total cost is divided into two parts – initial cost and operating cost. The initial cost is considered as the summation of costs of all components. The operating time is set to be 20 years for all systems. The initial cost of the optimized PV system is the highest among all scenarios, mostly contributed by the battery storage system. For the life time total cost, the ETC system is the lowest in all scenarios. It costs about 28% of baseline system and 23% of the optimized PV system.

Table 4-4: Cost analysis of three systems

System Option	Generators + VCC	PV + Battery + VCC		ETC + ABC
		No Battery	PV in optimized size	
PV or ETC area (m^2)	N/A	2,000	2,000	2,000
Initial cost of PV or ETC ($) [106] [107] [108] [109]	N/A	800,000	800,000	800,000
Initial cost of battery ($) [110]	N/A	0	806,400	N/A
Initial cost of cooling device ($) [111] [112]	27,000	27,000	27,000	38,000
Total initial cost ($)	52,000	838,250	1,633,400	838,000
Total cost (Initial + Operating) (million $)	47.4	60.4	57.0	13.3

4.2 Waste Heat Powered System

4.2.1 Cruise Ship Application

For cruise ships, most are operated in tropical regions and require extensive amount of space cooling demands. In this chapter a novel waste heat powered microgrid system, primarily for space cooling, is proposed and studied. The space cooling system was modeled in TRNSYS. The system modeling starts with setting up cooling generation device – a chiller. Then the chilled water loop could be formulated with air handling units. The air loop could be implemented next by connecting to the building model. Lastly, the control logic needed to be set up. The cargo ship modeled in this study is operated between Miami and Bahama constantly. Therefore, weather data of Miami, FL was used. The simulation time ranges from the beginning of June to the end of September, when cooling demands are substantial. The simulation time step was 0.1 hour. Pumps and fans are two main auxiliary components in cooling systems. For pump simulation, a standard component in TRNSYS – type 741 was used. The power consumption of the pump was

calculated based on flow rate and pressure drop. For fan simulation, a standard component – type 662 was used. Similarly, the power consumption was obtained with known flow rate and pressure head. When setting the supplied air flow rate to each conditioned space, there has to be certain amount of fresh air mixed in to meet the hygiene requirement. ASHRAE standard "Ventilation for Acceptable Indoor Air Quality" [113] was followed as the guideline to set the amount of mixed fresh air. The total air flow rates and chill water pump flow rates for each cabin was obtained from manufacturer. Two cooling systems were set up – a baseline cooling system powered by VCC and a waste heat powered ABC cooling system. Following next, each system layout and control logic are discussed in detail.

4.2.1.1   *System Configuration*

For the baseline cooling system, the vapor compression chiller is sea water cooled. The supplied chilled water temperature is set to be 6.7°C [114]. The chilled water is distributed to air handling units of each cabin through a separate chilled water pump for each cabin. In the air handling units, the chilled water cools down the air, while itself gets heated up and then flows back to vapor compression chiller. On the air side, cooled air after air handling units is supplied to each cabin. At the exhaust air outlet, part of it is dumped to the ambient. The others are recirculated and mixed with fresh air. Then it is sent back to air handling units and gets cooled.

The control strategy was also set up. The thermostat keeps recording the space temperature of each cabin, and compares it with set temperature at each time step. An on/off signal is then produced and sent to air fan. The upper cooling set temperature is 25°C, which means the signal is on when the cabin temperature is higher than 25°C. The

81

lower limit of operation temperature is 23°C, which indicates the signal is off when the cabin temperature is below 23°C. The thermostat works as a controller with specific run time. Once the signal is on, it remains on for at least 0.2 or 0.1 hour (depending on different cabins) until it might be switched to off. Likewise, once the signal is off, it remains off for at least 0.1 hour until switching to on is possible. The room temperature, power consumptions and other key metrics are recorded as outputs at each time step. Also, they are displayed throughout the simulation as monitoring of the program.

Figure 4-5 show the schematic diagram of the waste heat powered absorption cooling system. The waste heat powered ABC cooling system has the same chilled water loop, air loop and control strategy design as the baseline cooling system. Instead of the vapor compression chiller, the H_2O/LiBr ABC is applied. The evaporator in the absorption cycle cools down the returned chilled water to the set temperature. The condenser and absorber are cooled by parallel sea water flows. The absorption cycle is hot water powered, which means the hot water flows through the generator and transfers heat to H_2O/LiBr solution. The hot water is obtained by pumping fresh water through the exhaust gas heat exchanger and absorbed heat from exhaust gas. The outlet hot water from the generator is used to meet shipboard hot water demands (residential, kitchen and clinic), then pumped back to the exhaust gas heat exchanger and heated up again. A water-to-water HX is designed to provide hot water demands. One side is recirculated hot water from outlet of the generator in the absorption cycle. The other side is demanded hot water from residential, kitchen and clinic. The sanitary demands were simulated with standard TRNSYS type 1234a. This component treats water usage with a daily schedule.
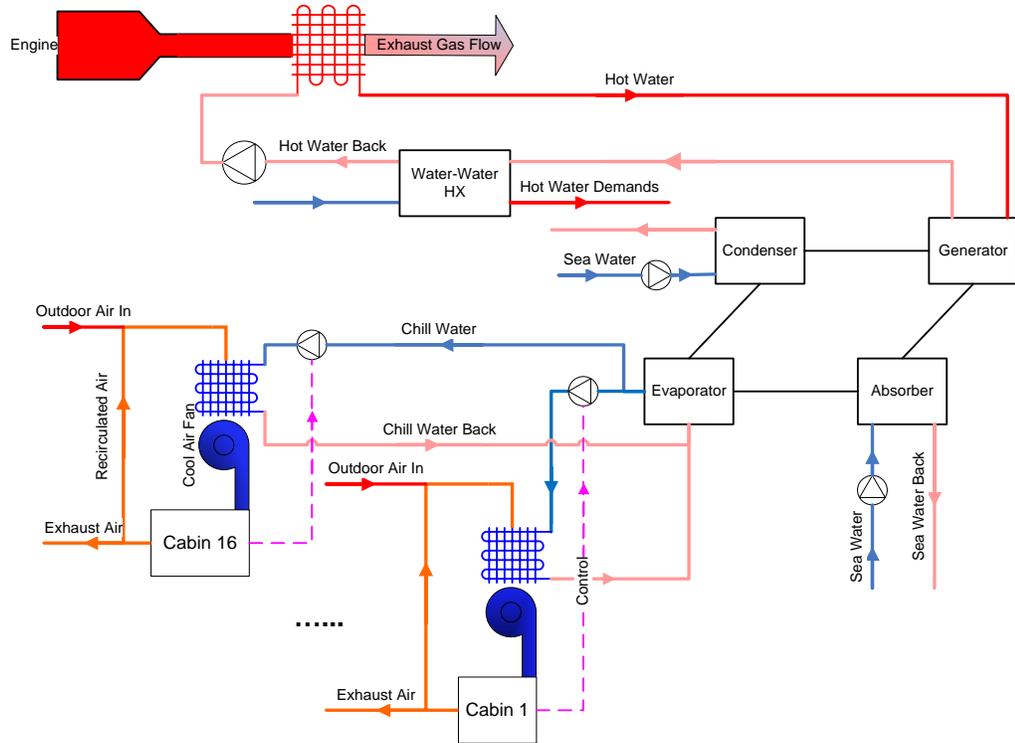
Figure 4-5: Schematic of waste heat powered absorption cooling system

4.2.1.2   *Space Condition Control*

The space psychrometric conditions are important indications for reasonable system design and successful control. First, the conditions are investigated from control point of view. Figure 4-6 presents the psychrometric chart of moisture air. There are two clouds of data. The gray dots represent ambient conditions in Miami, FL. The blue dots represent the space conditions of 16 living spaces simulated. The red solid line indicates the control signal of thermostat. As it is merely based on temperature, only the upper (25°C) and lower (23°C) operation temperature limits are plotted.
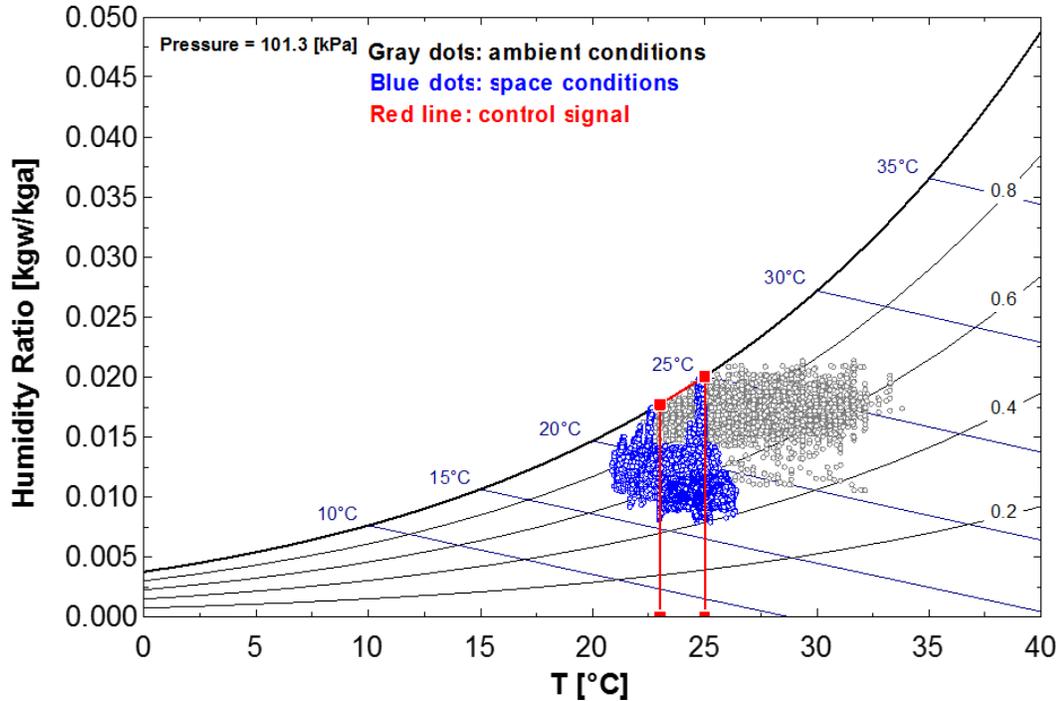
Figure 4-6: Psychrometric chart of space conditions with control signal

It can be seen that the ambient conditions are mostly located in high temperature (less than 23°C) and high humidity (greater than 0.013 kgw·kga[-1]) regions, which corresponds to typical summer conditions in Miami. Such conditions present substantial cooling loads. Regarding the control, majority of space conditions (70%) are located within the control signal temperature range. There are some points located beyond the range however. It is mainly due to the operation strategy of the thermostat. For instance, once the cooling system is on, it will remain on for at least 0.2 hour. Therefore, the room temperature may already fall below 23°C after 0.2 hour, at which time the room temperature being recorded again and off signal is produced. As most of points are fluctuating within or around the control signal temperature range, the system is considered to have a robust control.

Coming next the space conditions are investigated from thermal comfort point of view. Figure 4-7 shows the space conditions with thermal comfort region. The red line presents the thermal comfort region of living space in summer based on ASHRAE standard "Thermal Environmental Conditions for Human Occupancy" [115]. It can be seen that most of the space conditions (above 80%) are located within the thermal comfort regions. Therefore, the system is considered to have a reasonable design for Miami ambient conditions.
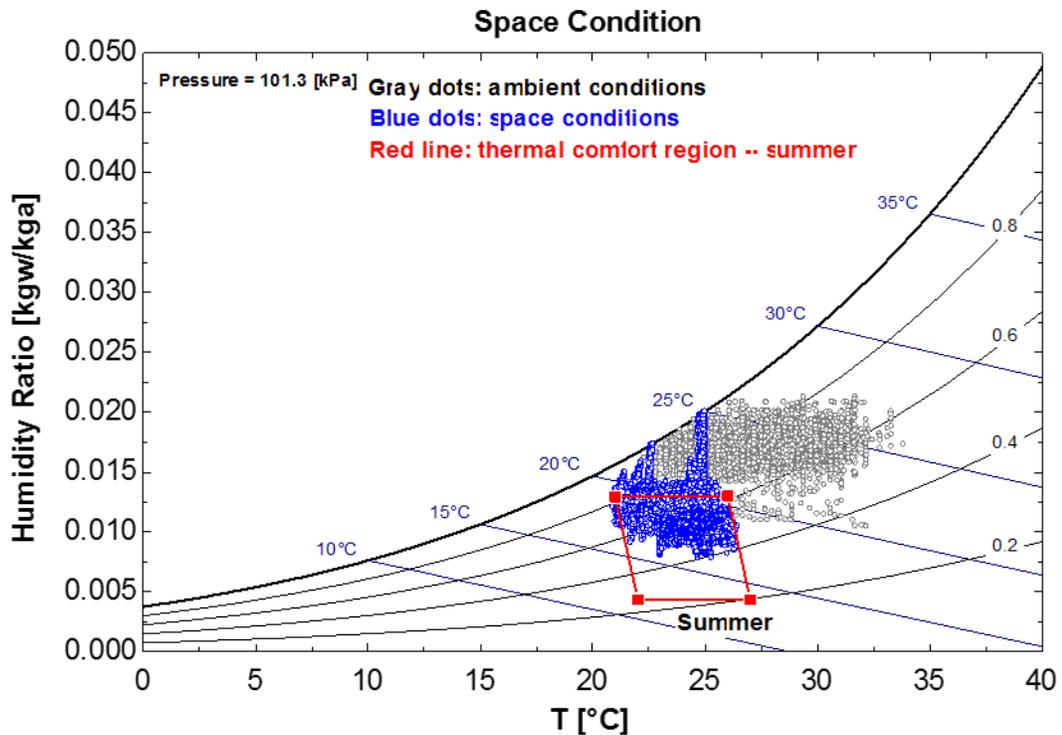
Figure 4-7: Psychrometric chart of space conditions with thermal comfort region

4.2.1.3 *Cooling Season Performance Evaluation*

In this chapter, the performances of the baseline and waste heat powered cooling systems are summarized and compared. First, the cooling system simulation results need to be carefully validated. Experimental data matching shipboard cooling system simulated

is not available. Building dataset commercial building energy consumption survey (CBECS) is used instead. Table 4-5 shows comparison of the cooling system electricity consumption intensity between the baseline system and CBECS dataset [116]. Particularly, two subsets in CBECS were chosen according to the cooling equipment of the baseline system and weather data region. The cooling system electricity consumption intensity matches each other well since the weather conditions are the same. However, shipboard cabins experience larger convection heat transfer rates due to higher relative wind velocities. Therefore, the electricity consumption intensity is slightly higher than building dataset.

Table 4-5: Electricity consumption intensity comparison between baseline cooling system and CBECS dataset

Index	Baseline Simulation	CBECS (Cooling Equipment: Central Chiller)	CBECS (Region: South Atlantic)
Cooling system electricity consumption intensity (kWh·ft^{-2})	3.4	3.1	3.0

Table 4-6 summarizes the performance of both cooling systems over the whole cooling season. Both systems have exactly the same cooling demands, which is expected as they are simulated under the same ambient conditions with exact chilled water and air loop configurations. The waste heat powered cooling system has higher power consumptions (13,999 kWh) in fans and pumps than the baseline (5,870 kWh). The reason is that the absorption cycle needs extra pumps for cooling sea water flows and hot water flows. Besides meeting the cooling demands, the waste heat powered system could also provide high temperature (98~99°C) water flows at the generator outlet. The hot water flow could meet residential hot water demands or other heating purposes.

Table 4-6: Comparison of the performance of baseline and waste heat powered

cooling system under Miami condition

Index	Baseline (VCC)	Waste Heat (ABS)
Energy Demands and Consumptions		
Cooling Demands (kW·h)	131,780	131,780
Pumps and Fans (kW·h)	5,870	13,999
Chiller Power (kW·h)	30,687	-
Generator Demands (kW·h)	-	205,826
Byproduct		
Hot Water Flow Rate (kg·s^{-1})	-	24
Hot Water Temperature (°C)	-	98~99
System Performance		
COP$_{VCC}$	4.29	-
COP$_{ABS}$	-	0.64
COP$_{system}$	3.60	0.60 (9.41)
Fuel and CO$_2$ Emission		
Total Fuel Consumption (kg)	8,408	3,220 (-62%)
Total CO$_2$ emission (ton CO$_2$eq)	30.71	11.76 (-62%)

The system performance is calculated for the whole cooling season. The definitions are given in Equations (4-4) to (4-6).

$$COP_{VCC} = \frac{\dot{Q}_e}{W_c} \tag{4-4}$$

$$COP_{system} = \frac{\dot{Q}_e}{W_c + W_p + W_f + W_{sp} + \dot{Q}_g} \tag{4-5}$$

$$COP_{system\_electricity} = \frac{\dot{Q}_e}{W_c + W_p + W_f + W_{sp}} \tag{4-6}$$

The Q_e is the evaporator capacity or cooling demands in other words. W_c is the power consumption of chiller. W_f and W_p are the power consumptions of pumps and fans,

respectively. Q_g is the generator capacity in the absorption cycle. The vapor compression chiller has a COP of 4.26, while the absorption cycle's COP is 0.64. Including the power consumptions of pumps and fans, the baseline system has a COP of 3.60, which is higher than that of waste heat powered cooling system (0.60). However, the COP of the waste heat powered cooling system could be up to 9.41 if the waste heat energy is considered "free".

The main motivation of proposing the waste heat powered cooling system is to reduce the fuel consumption and consequently, CO_2 emission. In this study, the electricity demands (pumps, fans, vapor compression chiller, etc.) in both cooling systems are provided by diesel generators. Therefore, reductions in electricity demands lead to fuel consumption and CO_2 emission reductions. The fuel consumption rate is assumed to be 0.23 kg per unit electricity consumption (kW·h) [117]. The lifetime CO_2 emission rate is 0.84 kg CO_2eq per unit electricity consumption (kW·h) [118]. It is shown that the waste heat powered system reduces the fuel consumption and CO_2 emission by 62%, compared with that of the baseline.

4.2.1.4 *Weather Location Comparison and Study*

The cargo ships are sailing along the sea routes routinely. Therefore, the ambient conditions will change according to locations. In this section, the cooling systems were investigated under three different locations: Baltimore as a cold weather region, Miami as a hot weather region, and Abu Dhabi, UAE as an extreme hot weather region.

There are three input changes when the locations are modified – weather data, sea water temperature and absorption cycle solution flow rate. Changes in weather data results

in different cooling demands and also space conditions. Differences in sea water temperatures lead to the performance fluctuations in the vapor compression chiller and absorption chiller. For ABC, the solution flow rate needs to be adjusted to prevent the crystallization issue, which is discussed in detail later. Note the chilled water and air loop designs remain the same as these configurations remain the same once the system has been designed and built.

Figure 4-8 (a), (b) and (c) present the space conditions with thermal comfort regions in Baltimore, Miami and Abu Dhabi. In Figure 4-8, each psychrometric chart has two clouds of data – the gray ones represent the ambient conditions and blue ones represent the space conditions. The red solid lines indicate thermal comfort regions.
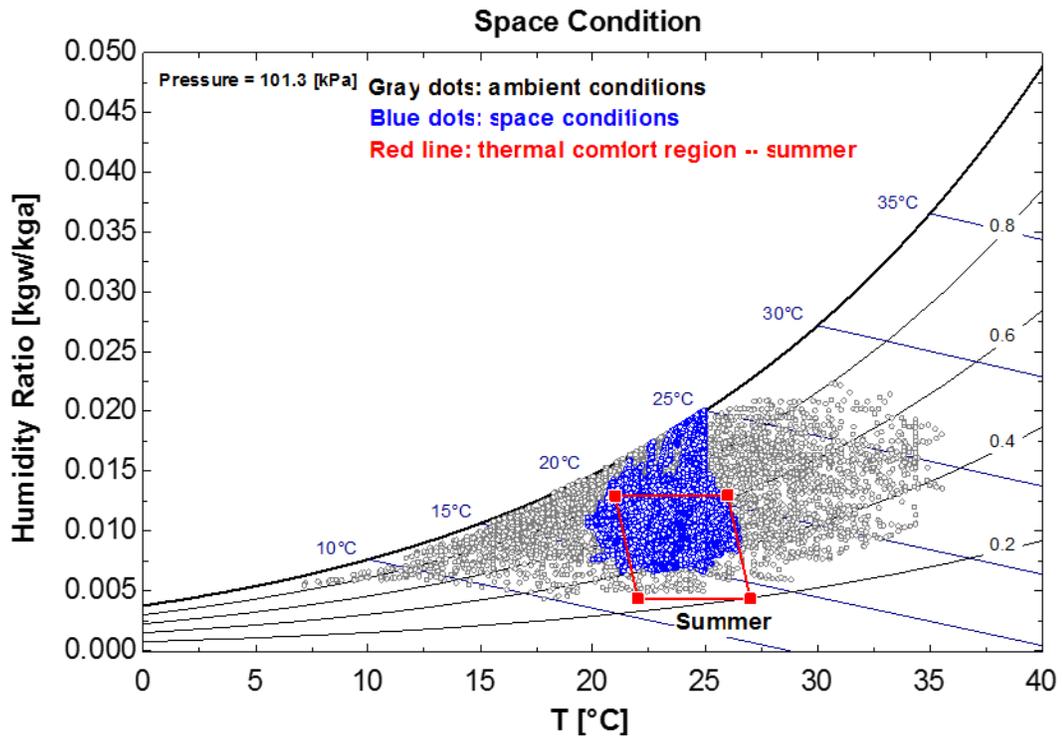
(a) Space conditions with thermal comfort region – Baltimore
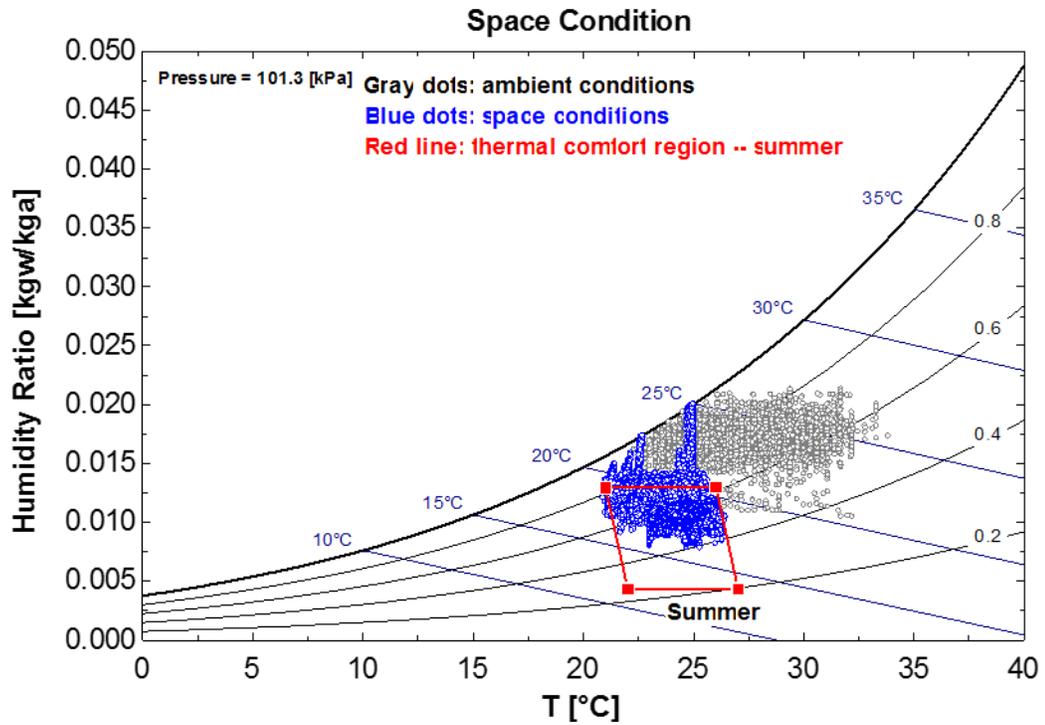
(b) Space conditions with thermal comfort region – Miami
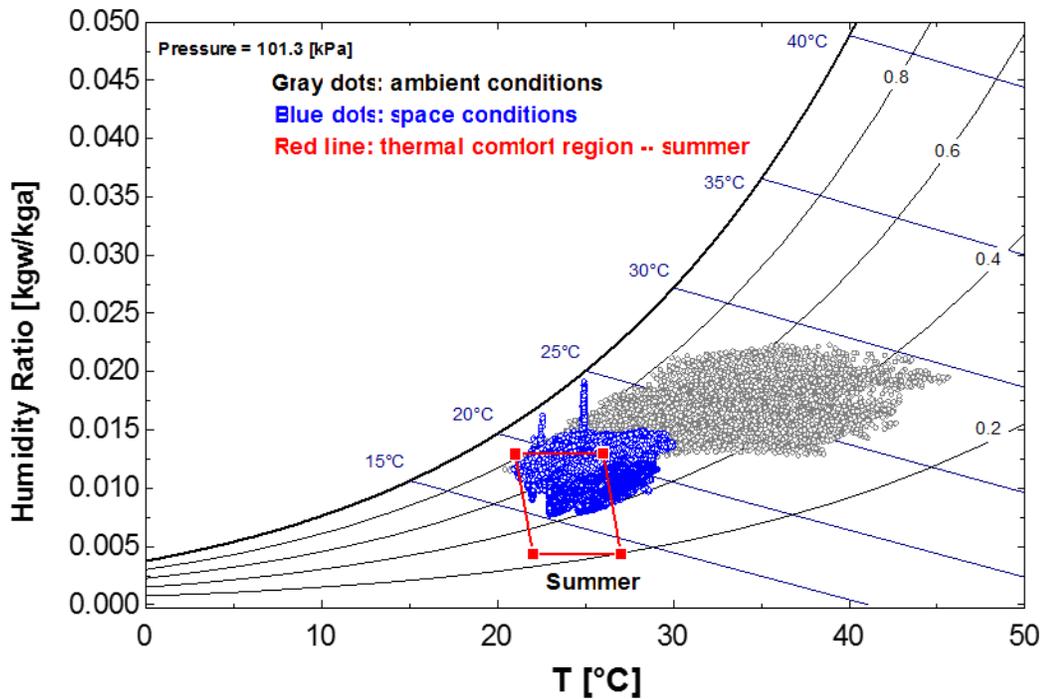
(c) Space conditions with thermal comfort region – Abu Dhabi

Figure 4-8: Space conditions of the cooling system under different locations

90

The gray points clearly indicate three different climates in three locations: mild summer in Baltimore, hot and humid summer in Miami, and extremely hot and dry summer in Abu Dhabi. Therefore, it is expected that Abu Dhabi has highest cooling demands, followed by Miami and Baltimore. Regarding space conditions, it can be seen that more points in Baltimore are located below the lower limit of thermal comfort region, compared to that of Miami. In contrast, more points in Abu Dhabi are located beyond the upper limit of thermal comfort region. This can be explained by the effects of mixed ambient air. Each space has a portion of mixed ambient air in the supply air, which could lead the room conditions inclined to ambient conditions.

The performances of the systems under three locations are also compared, as shown in Table 4-7. It can be seen that Abu Dhabi has highest cooling demands (145,423 kW·h), compared to 131,780 kW·h of Miami and 86,952 kW·h of Baltimore. As a result, the chiller power consumptions and generator capacities increase. For pumps and fans, the increments are rather insignificant as the only difference is the operation time of cool air fans, which have rather small power consumptions compared to that of cooling sea water pumps and fans.

Table 4-7: Comparison of cooling system performance under different locations

Location	Baltimore	Miami	Abu Dhabi
Baseline (VCC)			
Cooling Demands (kW·h)	86,953	131,780	145,423
Chiller Power (kW·h)	16,696	30,687	37,264
Pumps and Fans (kW·h)	5,810	5,869	5,888
COP_{VCC}	5.21	4.29	3.90
COP_{system}	3.86	3.60	3.37
Total Fuel Consumption (kg)	5,176	8,408	9,925
Total CO_2 Emission (ton CO_2eq)	18.91	30.71	36.25
Waste Heat (ABC)			
Cooling Demands (kW·h)	86,953	131,780	145,423
Generator Demands (kW·h)	134,823	205,826	236,563
Pumps and Fans (kW·h)	13,939	13,999	14,018
COP_{ABS}	0.64	0.64	0.61
COP_{system}	0.58	0.60	0.58
$COP_{system\_electricity}$	6.24	9.41	10.37
Total Fuel Consumption (kg)	3,206	3,220	3,224
Total CO_2 Emission (ton CO_2eq)	11.71	11.76	11.78
Fuel/CO_2 Reduction	0.38	0.62	0.68

Since the electricity demands of the waste heat powered ABC cooling system mostly come from pumps and fans, the fuel consumption and CO_2 emission also increase insignificantly. On the contrary, the baseline system has a significant increase in electricity consumption, contributed by the VCC. That being said, waste heat powered cooling system could save more in fuel consumption and CO_2 emission. The waste heat powered cooling system reduces the CO_2 emission by 68% in Abu Dhabi, 62% in Miami and only 38% in Baltimore.

For the VCC performance, the COP decreases from 5.21 to 3.90 with increasing sea water temperature from 22°C to 35°C. With higher sea water temperature cooling

condenser, the condenser pressure increases. Meanwhile, the evaporator pressure keeps the same as the chilled water set point temperature remains the same. Therefore, the temperature lift between the condenser and evaporator increases, consequently the VCC power consumption.

For the ABC, keeping the operation constraints (primarily the crystallization issue) inactive is the main concern. Increasing the cooling sea water temperature leads to increase in concentrations in strong solution flows. Eventually crystallization happens. One solution is to increase the solution flow rate. By doing that, the concentration of strong solution flows reduces and will offset the effects brought by raising sea water temperature. Note the COP of ABC in the system is around 0.6, while for a typical single effect H_2O/LiBr absorption cycle, the COP ranges from 0.6 to 0.8 [58]. The lower COP appears as the cycle is operating under transient conditions. Any off-design conditions increase the irreversibility in the cycle and degrade the COP.

The waste heat powered cooling system aims to reduce the fuel consumption of the cooling system, and ultimately the whole ship (by alleviating the main engine fuel loads). Cooling loads on the ship vary depending on the type of the ship. Therefore, the cooling loads were varied to show a higher potential of the suggested concept in fuel saving. The container ship has relatively small space cooling demands compared to the cruise ship. Table 4-8 shows comparison of fuel consumptions between the container ship and cruise ship. The cruise ship has 2,000 living cabins [99], compared to 16 on the container ship. As cooling loads are increased, the share of cooling system fuel consumption/saving to the main engine fuel consumption increases. As shown below, applying the waste heat

powered absorption cycle cooling system in the cruise ship can save the total energy consumption by 8.23%.

Table 4-8: Comparison of cooling system fuel consumption between container ship and cruise ship

Index	Container Ship	Cruise Ship
Cabin No.	16	2000
Baseline system fuel consumption (kg)	13,626	1,703,248
Waste heat powered system fuel consumption (kg)	5,218	652,235
Cooling system fuel consumption saving (kg)	8,408	1,051,013
Main engine fuel consumption (kg)	12,764,390	12,764,390
Cooling system fuel consumption share (%)	0.11	13.34
Cooling system fuel saving share (%)	0.0007	8.23

4.2.2   Container Ship Application

Different from cruise ships, container ships usually have large amount of reefer containers which requires deep refrigeration. The space cooling demands are much smaller than cruise ships as only crew living space requires space cooling. Besides, container ships are sailing throughout the world even in high latitude sea route, therefore heat demands need to be considered. In this chapter, a novel waste heat powered microgrid system for space cooling, refrigeration, space heating and water heating is proposed and studied.

TRNSYS [119] was used as the platform to conduct system simulation. Previously developed models were integrated with standard TRNSYS types to setup systems. Two systems were simulated – the baseline and waste heat powered (WHP) system. Both system configurations are explained in detail in following two chapters. Specifications regarding thermal zones, as well as the internal loads were introduced in the previous publication [120]. Reefer containers are distributed into three temperature settings: 40% at

-5°C, 40% at -15°C and 20% at -25°C based on ship operation information from Samsung Heavy Industry. The simulation time step is 0.1 h. Table 4-9 summarizes the general simulation information.

Table 4-9: Simulation program information

Index	Information	Comment
Main engine	WARTSILA 8RT-flex68-D	Rate capacity 25,040 kW
Living spaces	16 in total	Details in [120]
Reefer containers	65 FEUs maximum	
Sea route	Pusan, South Korea to Karachi, Pakistan Tokyo, Japan to San Francisco, U.S.A.	~1000 hrs. sailing time ~300 hrs. sailing time
Sailing Time	Start at the beginning of August	
Simulation Step	0.1 hr.	
Pump	Type 741	Standard TRNSYS component
Fan	Type 662	Standard TRNSYS component
Heat exchanger	Type 5b	Standard TRNSYS component

4.2.2.1 *System Configuration*

Figure 4-9 shows schematics of the baseline system. There are two modes in the baseline system – space cooling and heating. In space cooling mode, a sea water cooled vapor compression chiller is used to produce chilled water. The chilled water cools down supply air to living spaces. The cooled air meets space cooling demands. The air circulation loop is designed based on ASHRAE standards [121]. A certain amount of return air is recirculated and mixed with ambient air. Under space heating mode, a fuel fired boiler is used to generate hot water. The hot water circulates through heating coil and heats up air, which meets space heating demands. The electric heater is used as a backup heating equipment. The hot water can also meet residential hot demands. The refrigeration system

represents integrated reefer containers onboard. For the baseline system, reefer containers are equipped with air cooled VCC reefer units. The ambient air is used as cooling source.

The control strategy is set up using on or off controllers with specific run time. For space cooling or heating, control signals are sent to pumps to regulate chilled water or hot water flows. The heating and cooling set points are 22 and 24°C, respectively. For the reefer unit, the controller controls on and off status of the VCC reefer unit, as well as supply air flow rate.
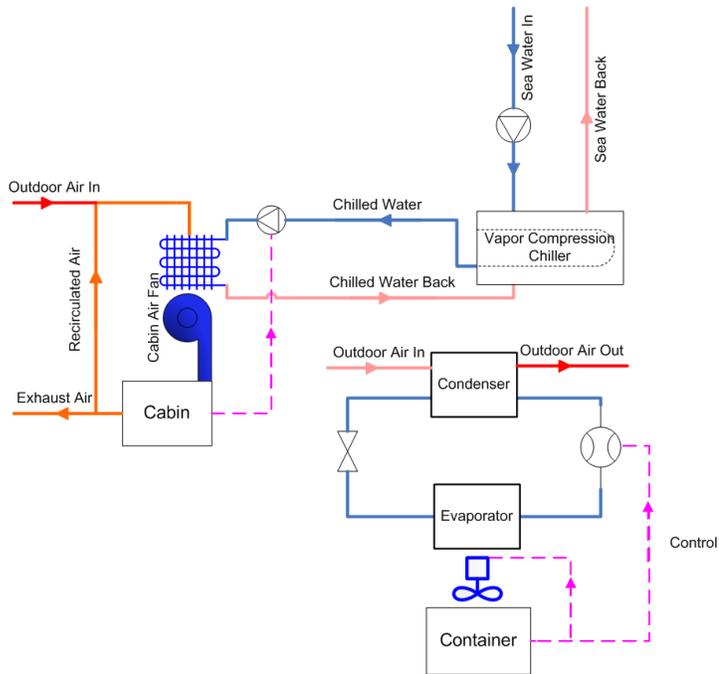
(a) Cooling mode
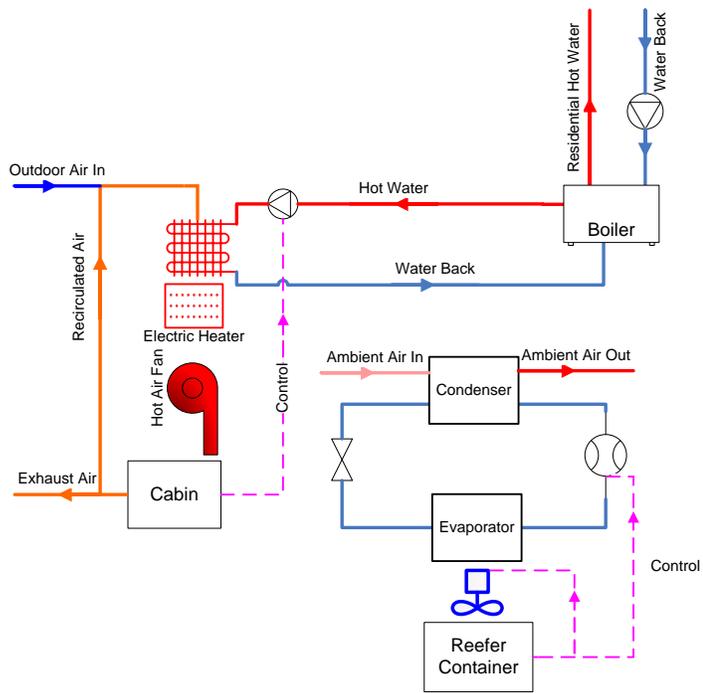
(b) Heating mode

Figure 4-9: Schematic of the baseline system

Figure 4-10 shows the schematic of the WHP system. The exhaust gas from the main engine flows through a waste heat recovery heat exchanger, where exhaust gas transfers heat to fresh water flow. The outlet hot water is used to drive ABC. Chilled water generated from the ABC is divided into two sub-flows. The first flow passes through the space cooling coil, similar to the baseline system. The second flow goes through a dedicated water-air heat exchanger. The chilled water cools down air, which is the cooling source for condensers of VCC reefer units. The cooling air for reefer units is cooled by 6.7°C chilled water, therefore it is usually around 12°C. This temperature is much lower that ambient temperature during most of low latitude sea routes. Therefore, the proposed cascaded configuration is able to lower refrigeration unit condenser pressure, consequently reduce compressor power consumption throughout the sailing route.

The hot water coming out from the generator of absorption cycle is around 85°C and can be used for space heating or residential water heating. An economizer is used in the WHP system. The hot water from ABC heats up water flow supplied to space heating coil or residential usage. The WHP system employs similar control strategies as the baseline system. The space temperature control is realized by regulating hot water or chilled water flow to heating or cooling coil, respectively. The reefer container temperature control is reached by regulating on or off status of VCC and supplied air flow.
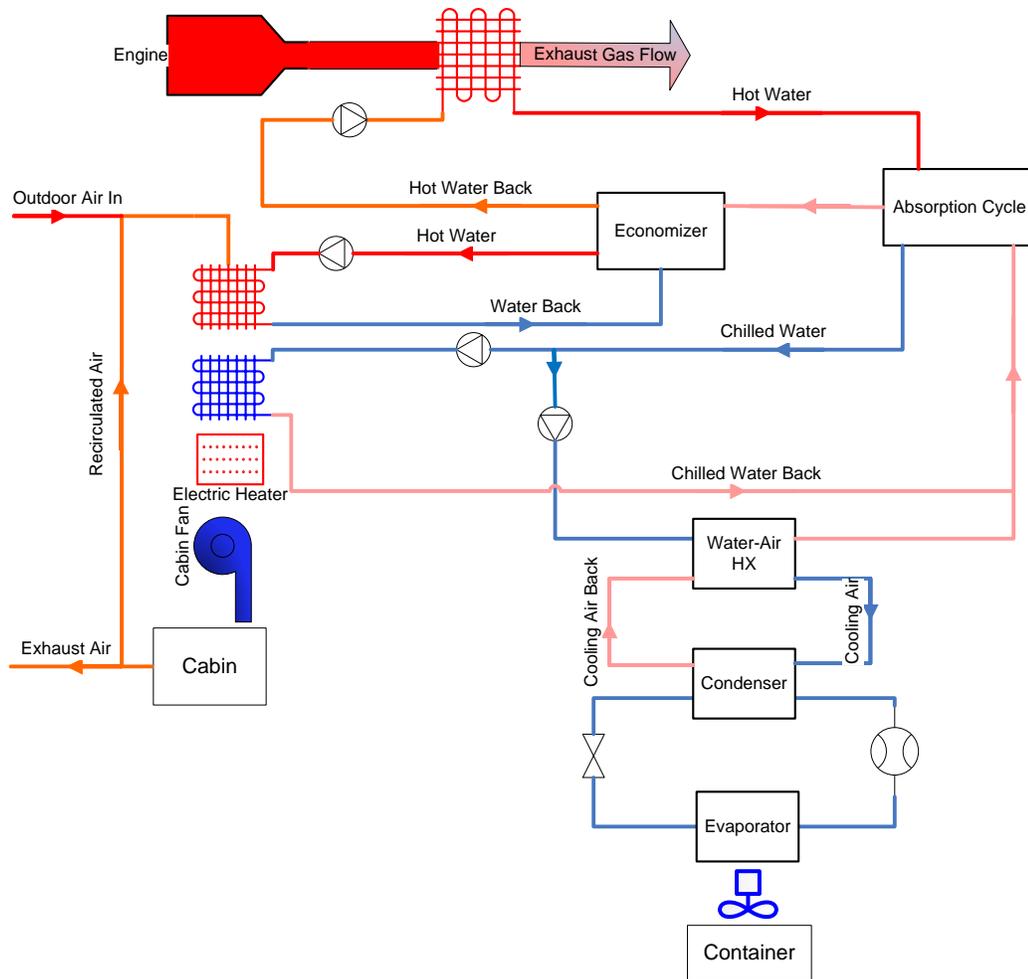
Figure 4-10: Schematic of the waste heat powered system

Note a water-to-air heat exchanger is used in the cascaded absorption-compression system, instead of using chilled water cooling condensers of reefer units directly, which is expected to bring better performance as the chilled water can cool condensers down to lower temperatures. It is not considered here as most VCC reefer units manufactured do not have water cooling options available. That being said, the air cooled cascaded cooling system still needs to be tailored properly to minimize duct and pipe work. Nowadays container ships tend to use the ship hold design. Usually dozens standard FEUs or TEUs are placed within one ship hold. The ship hold has two large openings for cooling air

circulation. For the conventional design, one opening is for supply air, while the other opening is for return air. Such configuration can be fully utilized in the WHP system.

Figure 4-11 shows the proposed ship hold duct and pipe layout. The dedicated water to heat exchanger supplies cooling air to ship holds. For each ship hold, there is a circulated air loops connected to the water to air heat exchanger. Inside the ship hold, reefer containers are stacked in the same direction. The supply air is inducted to cool condensers of reefer containers and then dumped to the other end. The layout fully utilizes the conventional ship hold design. The extra duct work is the circulation air loops for each ship hold and piping for dedicated water to air HX.
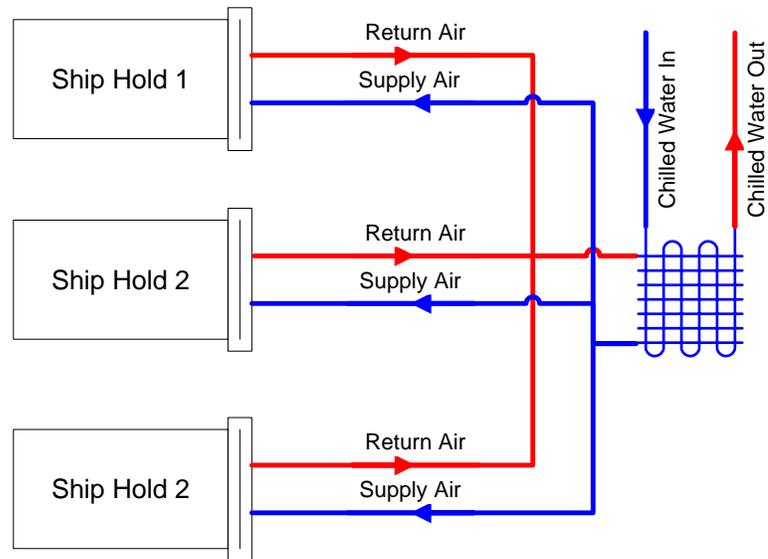
(a) Outside the ship hold
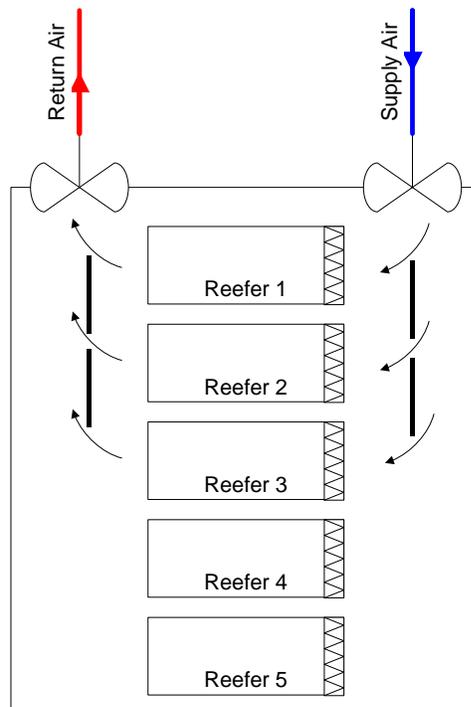
(b) Inside the ship hold

Figure 4-11: Waste heat powered system ship hold duct and pipe layout

4.2.2.2 Performance Evaluation

The system performance evaluation starts with space condition monitoring, indicating whether the system operates normally. Figure 4-12 presents the psychrometric plot of living spaces. The gray dots are ambient conditions, which are mostly hot (>25°C) and humid (>60%). The green dots are living space conditions and the red line is ASHRAE cooling season thermal comfort zone [122]. It is seen that space conditions are mostly within ASHRAE cooling season thermal comfort zone. Some space conditions have higher humidity than thermal comfort zone, which are expected as the space are conditioned based on temperature settings merely.
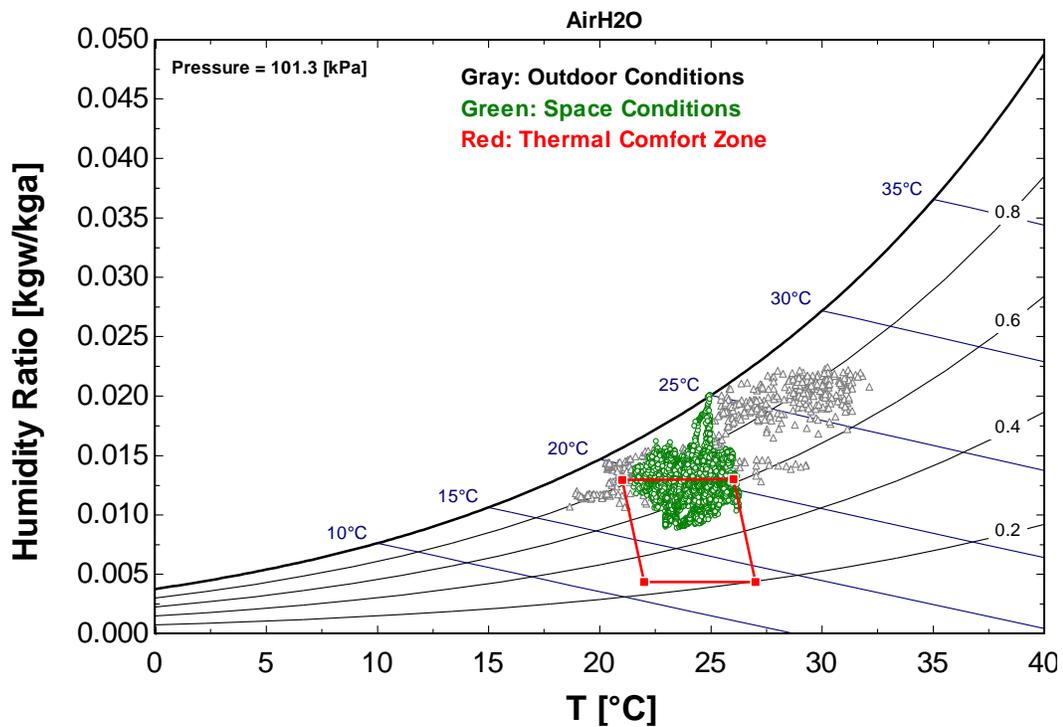
Figure 4-12: Container ship living space conditions

The simulated system meets several shipboard energy demands. Figure 4-13 shows daily energy demands and ambient air temperature along the route. It is seen that

refrigeration demands are the dominant one, roughly takes 75% all time. Space cooling comes next. Another trend is that space cooling demands are weather dependent, which are higher during middle of sailing period, corresponding to higher ambient temperature. On the contrast, refrigeration and water heating demands are insensitive to ambient conditions. The reason is that the space cooling system involves conditioning ambient air, which directly imposes weather effects on space cooling demands. The refrigeration and water heating system are operated without conditioning ambient air. As the sea route has high ambient temperature throughout the sailing period, there is no space heating demands.
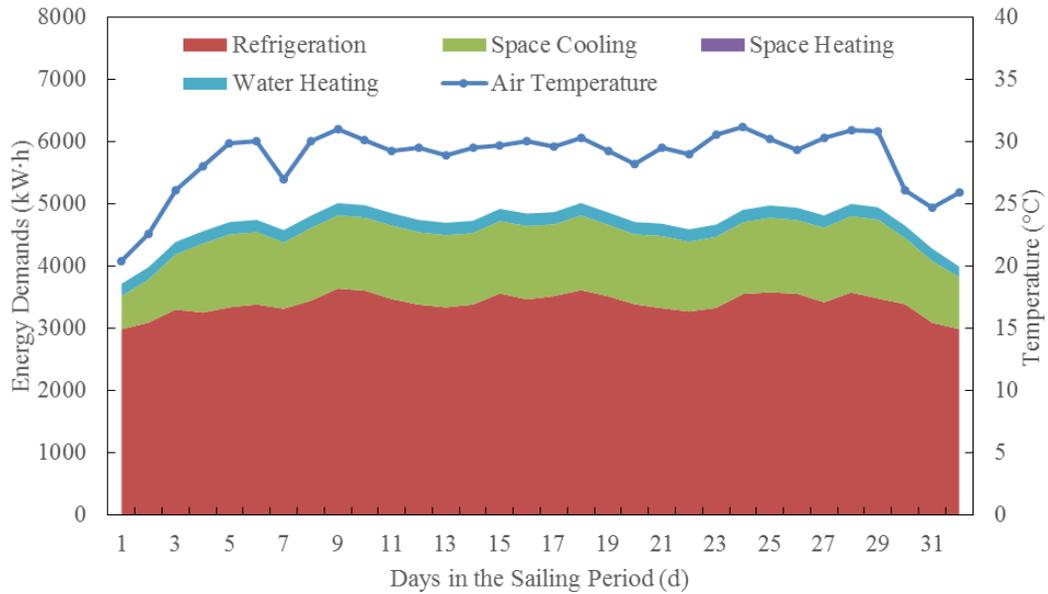
Figure 4-13: Daily energy demands and ambient temperature along sea route from Pusan to Karachi

While two systems meet same amount of energy demands, fuel consumptions are different. Figure 4-14 compares the daily fuel consumptions of two systems. The WHP system generally has lower fuel consumption than the baseline system, though its daily

103

reduction varies. When ambient temperature is higher, the baseline system fuel consumption increases, while the WHP fuel consumption remains relatively unchanged. The reason comes from the refrigeration system. For the baseline system, condenser cooling source is ambient air. When ambient air temperature increases, so does the condenser pressure. Therefore, the reefer unit power consumption increases. For the WHP system, the cooling source are cooled air, of which the temperature is relatively constant (fluctuating between 11~13°C).
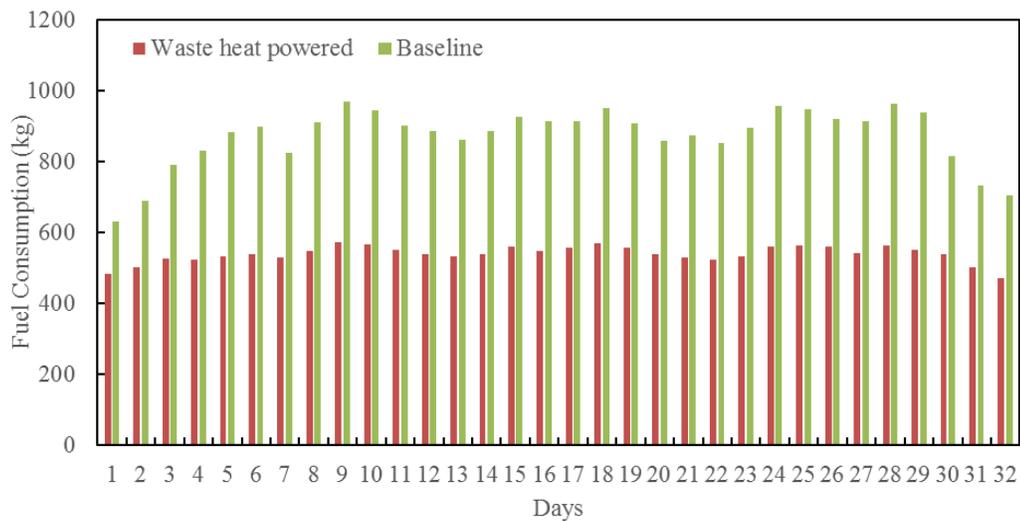
Figure 4-14: Daily fuel consumption comparison between the baseline and WHP system

Table 4-10 summarizes energy demands, system performance, fuel consumption and CO_2 emission of two simulated systems. Energy demands are almost the same, as both systems operate under same weather conditions. Reefer units of the WHP system consume 43% less power than baseline units, resulted from lower condenser pressure. The auxiliary power consists of pump and fan power consumption. Compared to the baseline system, the WHP system has extra pumps for exhaust gas flow, hot water flow to ABC and chilled

water flow to dedicated water-to-air heat exchanger. Consequently, it has higher auxiliary power consumption.

Table 4-10: Comparison of two systems along Pusan, South Korea to Karachi,

Pakistan sea route

Index	Baseline	WHP
Energy Demands & Consumption		
Space Cooling Demands (kW·h)	35,372	35,342
Reefer Cooling Demands (kW·h)	108,420	108,411
Water Heating Demands (kW·h)	6,304	6,304
VCC Chiller Power (kW·h)	7,620	-
VCC Reefer Power (kW·h)	98,880	56,584
Auxiliary Power (kW·h)	11,500	18,393
Boiler Energy Input (kW·h)	8,081	-
Generator (ABC) Energy Input (kW·h)	-	336,176
System Performance		
$COP_{chiller}$	4.64	-
COP_{ABC}	-	0.59
COP_{VCC}	1.10	1.92 (+75 %)
η_{boiler}	0.78	**-**
$COP_{system\text{-}electricity}$	1.27	2.00 (+57 %)
Primary Energy Ratio	0.50	0.80 (+60 %)
Fuel Consumption and CO_2 Emission		
Total Fuel Consumption (ton)	27.89	17.24 (-38 %)
Total CO_2 emission (ton CO_2eq)	254	157 (-38 %)

System performances are calculated and compared. Two indices are used to evaluate the overall system performance – COP of system based on electricity input and PER. The definitions are given in Equations (4-7) and (4-8).

$$COP_{system-electricity} = \frac{Q_{spacecooling} + Q_{reefer} + Q_{waterheating}}{P_{VCCchiller} + P_{VCCreefer} + P_{auxiliary}} \tag{4-7}$$

$$PER = \frac{Q_{spacecooling} + Q_{reefer} + Q_{waterheating}}{M_{HFO}LHV_{HFO}} \tag{4-8}$$

M_{HFO} is the total fuel consumption. LHV_{HFO} is the low heating value of heavy fuel oil, which is 39,000 kJ·kg^{-1}. It is concluded that reefer units of the WHP system have 75 % better performance than that of the baseline system. Regarding the whole system performance, WHP improves the COP of system based on electricity input by 57 %, and PER by 60 %.

The motivation to propose the WHP system is to reduce fuel consumption, which brought by diesel generators. The heavy fuel oil consumption rate of diesel generators is 0.23 kg·(kW·h)$^{-1}$ [123]. The life time CO_2 emission rate of heavy fuel oil is 840 g CO_{2eq}·(kW·h)$^{-1}$ [124]. As presented in Table 4-10, the WHP reduces total fuel consumption and CO_2 emission by 38%.

4.2.2.3 *Energy and Carbon Flow Analysis*

The simulated system involves many different categories of energy demands, energy inputs and energy conversion equipment. To have a clear understanding how energy and CO_2 emission flows, Sankey diagram is used. The Sankey diagram is able to show the energy or CO_2 emission flow from energy input to final output, and the input-output characteristic of each equipment.

Energy flow characteristics of two systems are presented in Figure 4-15. Figure 4-15 (a) shows the energy flow diagram of the baseline system, while Figure 4-15 (b) shows the energy flow diagram of the WHP system. The baseline system is fully powered up by heavy fuel energy. Most of it is supplied to diesel generators. The electricity produced from diesel generators is used to meet auxiliary demands, VCC chiller and VCC reefer units. The boiler takes the rest portion of fuel energy and meets water heating demands. Diesel

generators bring most energy loss, thus degrade the whole system performance. For the

WHP system, the waste heat from the main engine provides most energy input, rather than

the heavy fuel oil. The waste heat is mainly used to power up the ABC, the rest is used to

meet water heating demands through economizer. The electricity produced by diesel

generators is supplied to VCC refer units and auxiliary components.
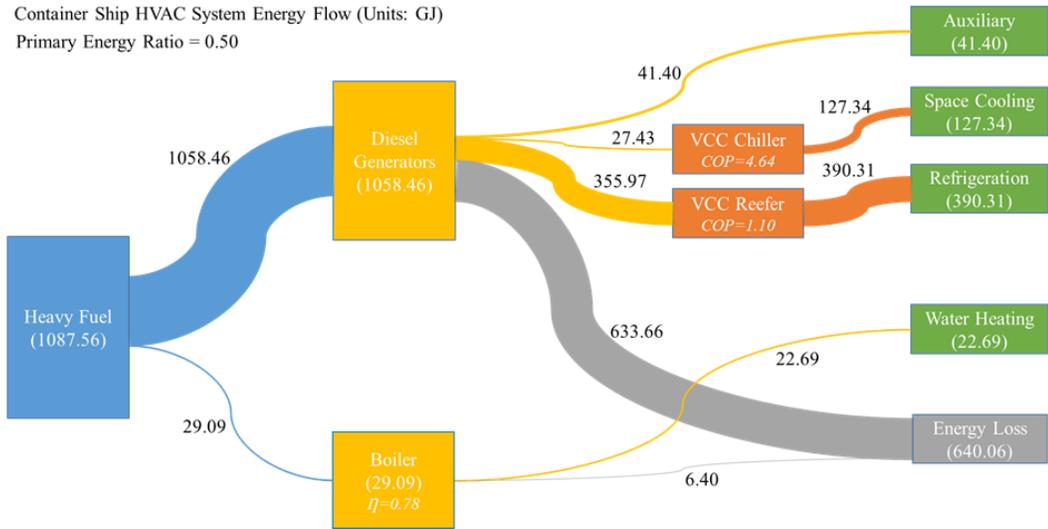
(a) Baseline system
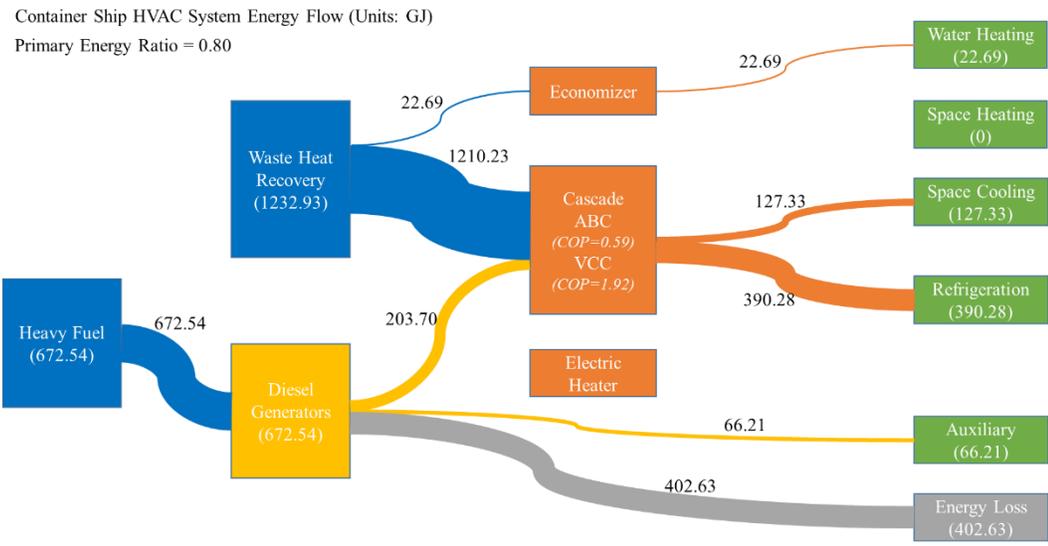
(b) WHP system

Figure 4-15: Energy flow of the baseline and WHP system

Burning heavy fuel oil brings many environmental concerns. The most significant one is the CO_2 emission. Figure 4-16 shows CO_2 emission flows of two systems. The CO_2 emission flow diagram indicates how much each energy demand and equipment contributed to total CO_2 emission. For the baseline system, direct emissions from diesel

generators contribute most, followed by VCC reefer units. For the WHP system, recovered waste heat has no contribution to CO_2 emission. Only diesel generators produced CO_2 emission. Direct emissions from diesel generators are still the dominant factor.

Container Ship HVAC System CO_2 Emission Flow (Units: ton CO_{2eq})
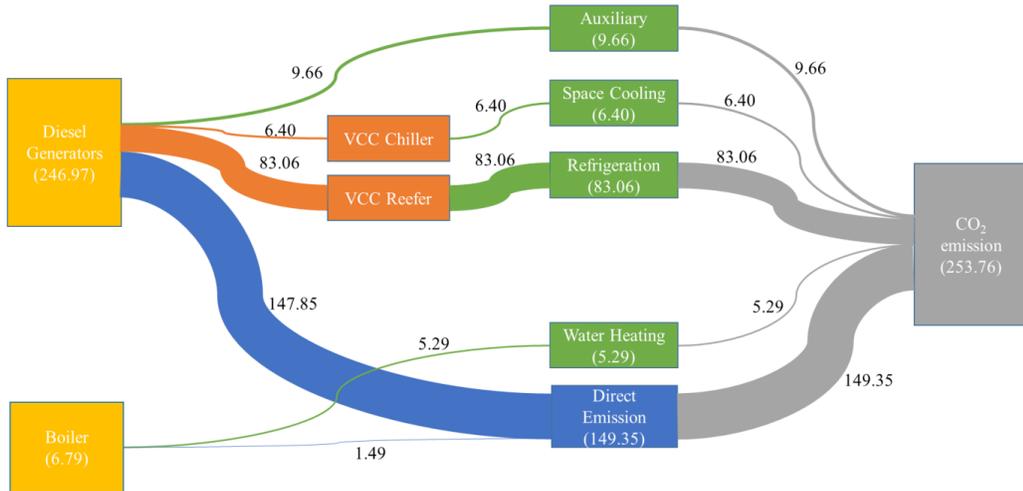
(a) Baseline system

Container Ship HVAC System CO_2 Emission Flow (Units: ton CO_{2eq})
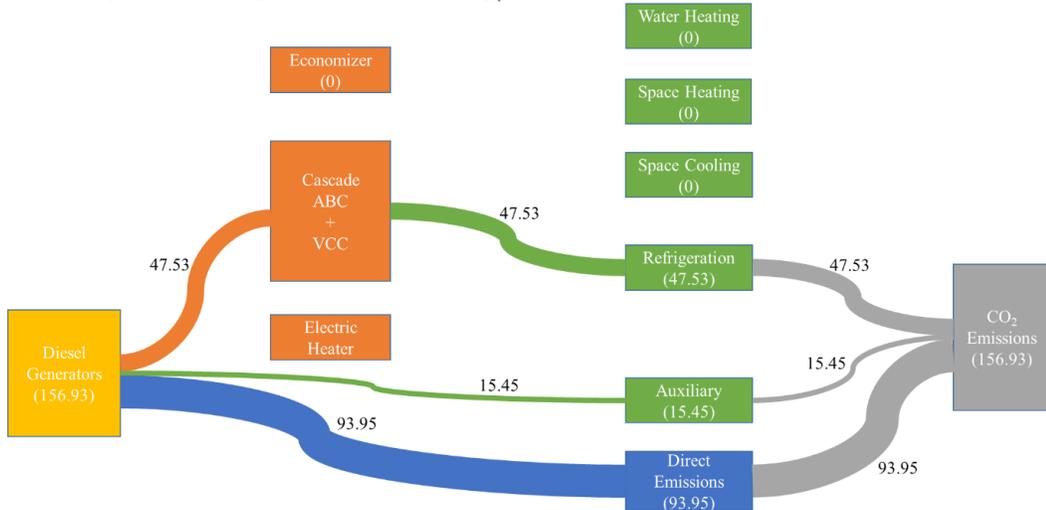
(b) WHP system

Figure 4-16: CO_2 emission flow of the baseline and WHP system

The main engine performance is also simulated throughout the sailing period, using performance map introduced in Chapter 2.3. Main engine energy flow diagrams of the baseline and WHP system are shown in Figure 4-17. The fuel energy supplied to main engine is either used for propulsion, or dumped as waste heat. The waste heat consists of air cooler, engine jacket, lubricant oil, radiation and exhaust gas, of which exhaust gas takes largest portion. Part of exhaust gas is recovered in the WHP system, therefore boosting up the main engine efficiency from 50.6% to 53.6%.

Main Engine Energy Flow – w/o Heat Recovery (Units: GJ)

ŋ = 50.6%

Air Cooler
(4,940)

4940

Engine Jacket
(2,305)

2305

2305

4940

Lubricant Oil
(2,115)

2115

2115

Main Engine
(41,961)

858

Radiation
(858)

858

Energy Loss
(20,710)

10493

Exhaust Gas
(10,493)

10493

21251

Propulsion
(21,251)
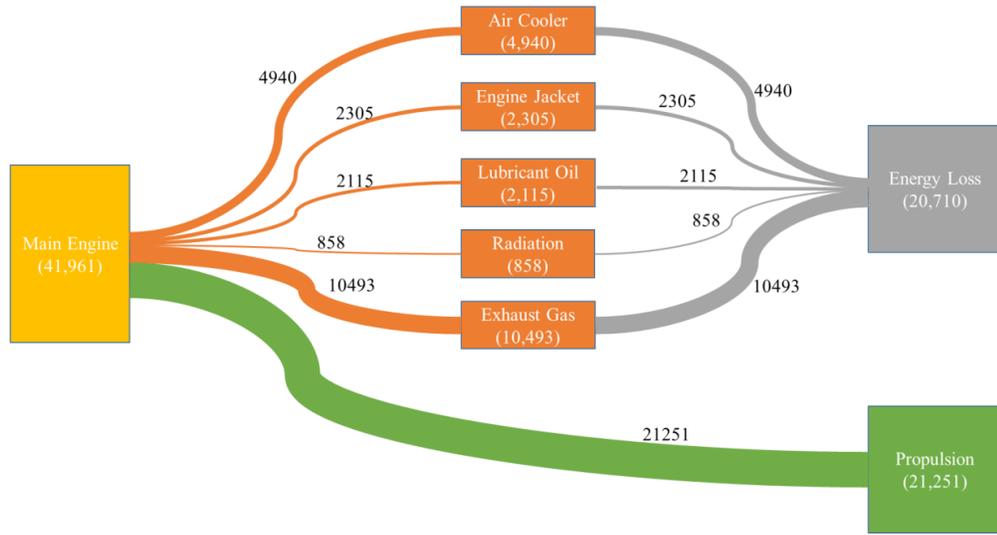
(a) Baseline system

Main Engine Energy Flow – w/ Heat Recovery (Units: GJ)

ŋ = 53.58%

Air Cooler
(4,940)

4940

Engine Jacket
(2,305)

2305

2305

4940

Lubricant Oil
(2,115)

2115

2115

Main Engine
(41,961)

858

Radiation
(858)

858

Energy Loss
(19,477)

10493

Exhaust Gas
(10,493)

9260

WHR
(1,233)

1233

21251

Propulsion
(21,251)
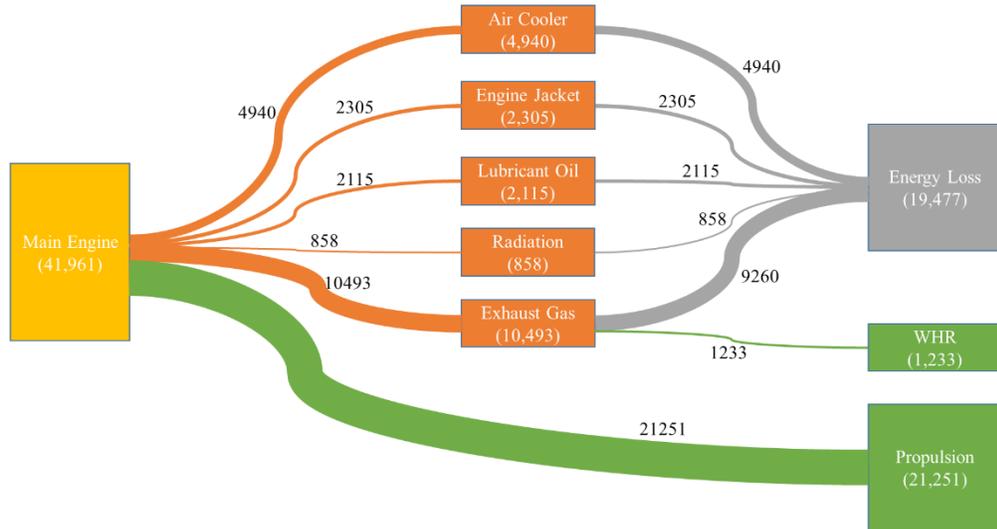
(b) WHP system

Figure 4-17: Main engine energy flow diagram

4.2.2.4   Sea Route Comparison

For the sea route investigated before, the temperature is relatively high (>25°C) throughout the sailing period, therefore the system has no space heating demands. In this chapter, the system is examined in a different sea route – from Tokyo to San Francisco. The sailing time is in August and lasts 13 days.

Figure 4-18 presents daily energy demands and temperature profile. The system operates under cooling mode at the beginning of the sailing time, later it transfers to heating mode. Figure 4-19 compares daily fuel consumptions between two systems. The trend is observed when ambient temperature goes down, fuel savings of the WHP system decrease. This is because under low ambient temperature, the baseline reefer unit already operates under low condenser pressure. Therefore, the cascaded cooling system configuration has relatively small advantage in power savings. In fact, when ambient temperature is lower than that of cooling air temperature (11-13°C) in the WHP system, the cascaded cooling system no longer reduces power consumption.
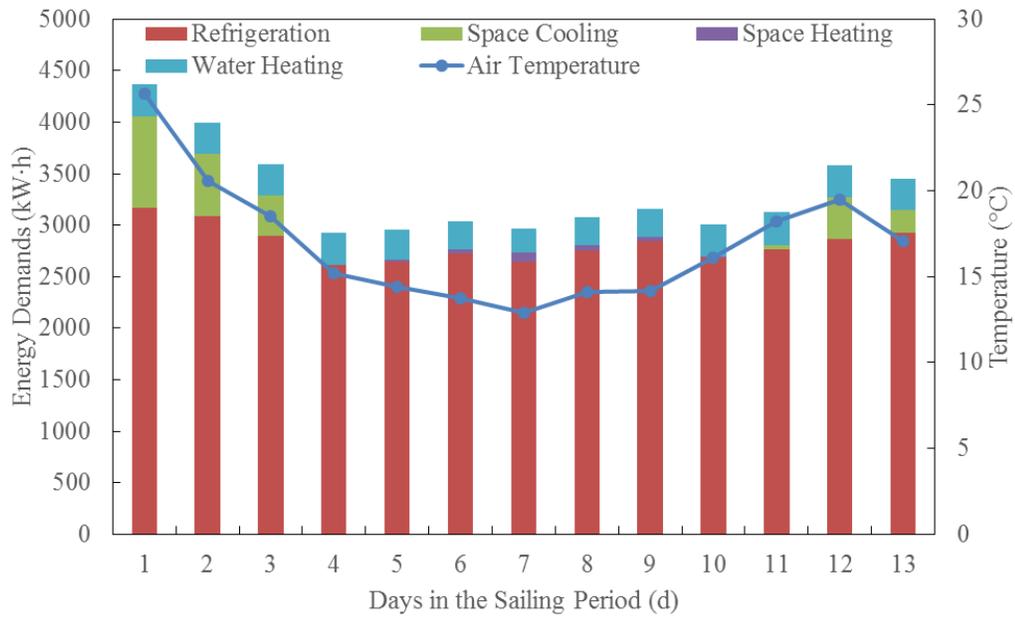
Figure 4-18: Daily energy demands and ambient temperature along sea route from Tokyo to San Francisco
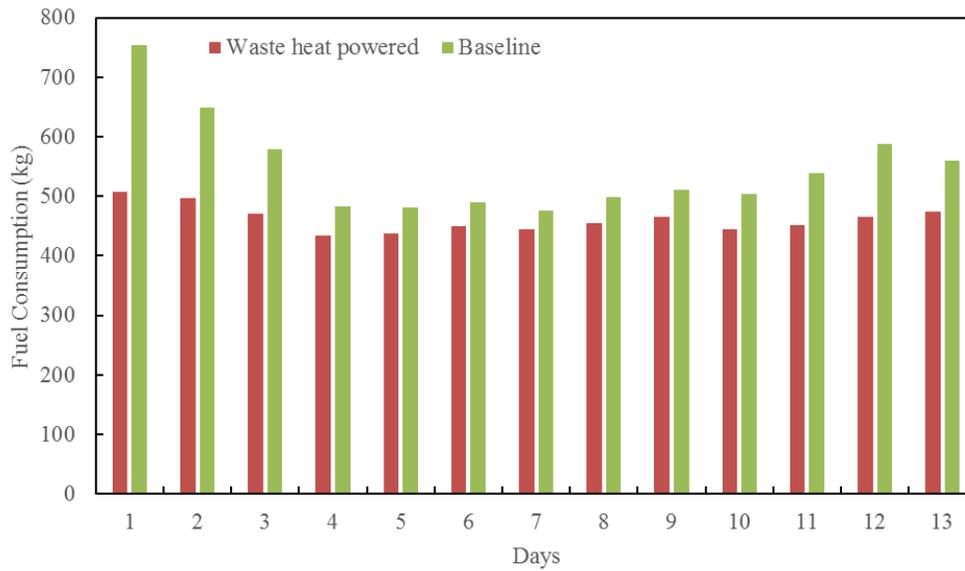
Figure 4-19: Daily fuel consumption comparison along sea route from Tokyo to San Francisco

113

Table 4-11 summarizes two system performances from Tokyo to San Francisco sea route. The WHP system is able to reduce the fuel consumption by 16%, less than 38% along sea route from Pusan to Karachi. As a conclusion, the proposed WHP system has better fuel saving potential when cooling and refrigeration demands are high.

Table 4-11: Performance comparison along Tokyo to San Francisco sea route

Index	Baseline	WHP
System Performance		
$COP_{chiller}$	5.22	-
COP_{ABC}	-	0.61
COP_{VCC}	1.47	1.92 (+31%)
η_{boiler}	0.78	**-**
$COP_{system\text{-}electricity}$	1.42	1.66 (+17%)
Primary Energy Ratio	0.55	0.67 (+22%)
Fuel Consumption and CO_2 Emission		
Total Fuel Consumption (ton)	7.11	6.00 (-16%)
Total CO_2 emission (ton CO_2eq)	64.71	54.60 (-16%)

4.2.3 System Validation

The baseline system simulation results from Pusan, South Korea to Karachi, Pakistan are validated against experimental data from Samsung Heavy Industry. Based on available experimental data, power consumptions of air conditioning unit and VCC reefer units were validated. The validation approach from ASHRAE guideline 14 [125] was adopted. Two indices were used to evaluate the accuracy of simulation results against experimental data – coefficient of variation of the root mean square error (CVRMSE) and normalized mean bias error (NMBE). Their definitions are given in Equation (4-9) and (4-10).

$$CVRMSE = 100 \times [\frac{\Sigma(y_i - \hat{y}_i)^2}{n - p}]^{1/2} / \bar{y} \qquad (4\text{-}9)$$

$$NMBE = \frac{\sum\limits_{}^{n}(y_i - \hat{y}_i)}{(n-p) \times \bar{y}} \times 100 \qquad (4\text{-}10)$$

In which $\hat{y}_i$ is simulation data, y_i is experimental data. N is the count of validated points. P is taken as one. These two indices are commonly used in building energy model calibrations.

Figure 4-20 shows hourly validations of air-conditioning and VCC reefer unit power consumptions. It can be seen that simulation data yield good agreement with experimental data. CVRMSE and NMBE of air-conditioning unit validation are 9.45% and 0.11%, respectively. For the reefer unit validation, the reefer number is updated according to real time loading / unloading profile. CVRMSE and NMBE of reefer unit power consumption validation are 26.95% and -4.85%, respectively. The reefer unit has a little bit larger deviations compared with air-conditioning unit, mostly contributed from time slots when loading / unloading information is not available (e.g. around 550 hr.) During these time slots, the profile is assumed to be the same with precedent time. As a conclusion, the baseline system simulation results yields satisfying accuracy regarding air-conditioning and reefer unit power consumptions.
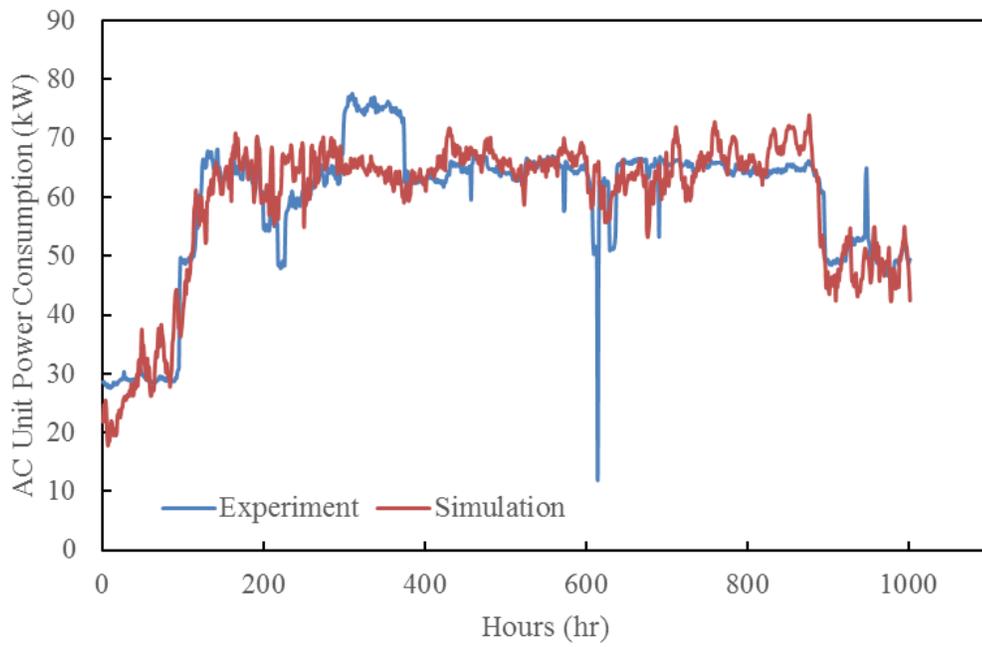
(a) Air-conditioning unit power validation
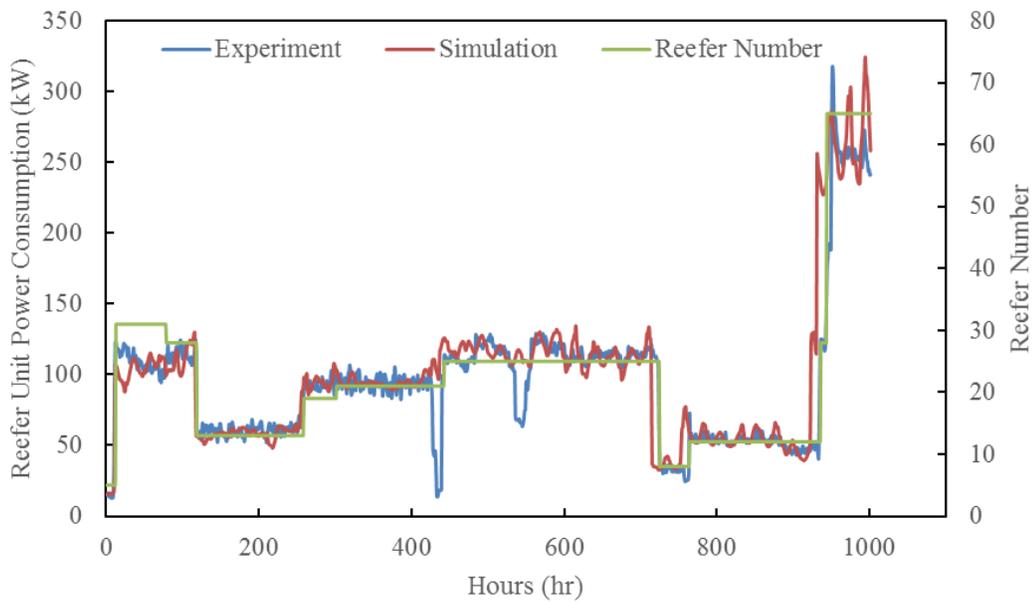
(b) Reefer unit power validation

Figure 4-20: Baseline system power consumption validation

4.2.4 Payload and Economic Study

Applying the WHP system to container ships saves fuel consumptions. However, the WHP system brings concerns at the same time. Two important questions need to be answered. The first one is how the WHP system affects the ship payload and main engine fuel consumption. The second question is whether replacing the baseline system with the WHP system makes sense or not from economic point of view. The first question leads to payload study of two systems, while the second question requires economic study.

The payload study starts with weight analysis of two systems. All major equipment was considered, of which the weight information was collected through manufacture manuals. Table 4-12 summarizes the weight information. It should be noted some common equipment such as cooling and heating coils were neglected as they make no contribution to the weight difference. The weight of fuels supplied to diesel generators for the whole sailing period were also considered, assuming all fuels were loaded at the beginning of the sailing period. As can be seen, the WHP system has 11% less initial total weight than the baseline system.

Table 4-12: System weight comparison

Equipment	Baseline (kg)	Waste Heat Powered (kg)
Compression chiller [126]	390	-
Absorption chiller [127]	-	11,113
Boiler [128]	531	-
Economizer [129]	-	4
Water to air heat exchanger [130]	-	252
Waste heat recovery unit [131]	-	574
Auxiliary pumps [132]	30	281
Diesel generators [133]	12,906	7,170
Fuel	26,817	16,787
Total weight	40,674	36,181 (-11%)

When the ship sails, the fuel weight keeps reducing. Therefore, it is meaningful to investigate the weight changes along the sea route. Figure 4-21 compares weight differences between two systems along the sailing route from Pusan to Karachi. Initially the WHP system has lower weight. As the ship sails, the WHP system fuel weight reduces at smaller rate compared to the baseline system. At the middle of the sailing period, the two systems reach the same weight. Eventually, the WHP system has higher weight than the baseline system. In short, in region A, the WHP system saves ship payload compared to the baseline system, while in region B, the baseline system benefits the ship payload.
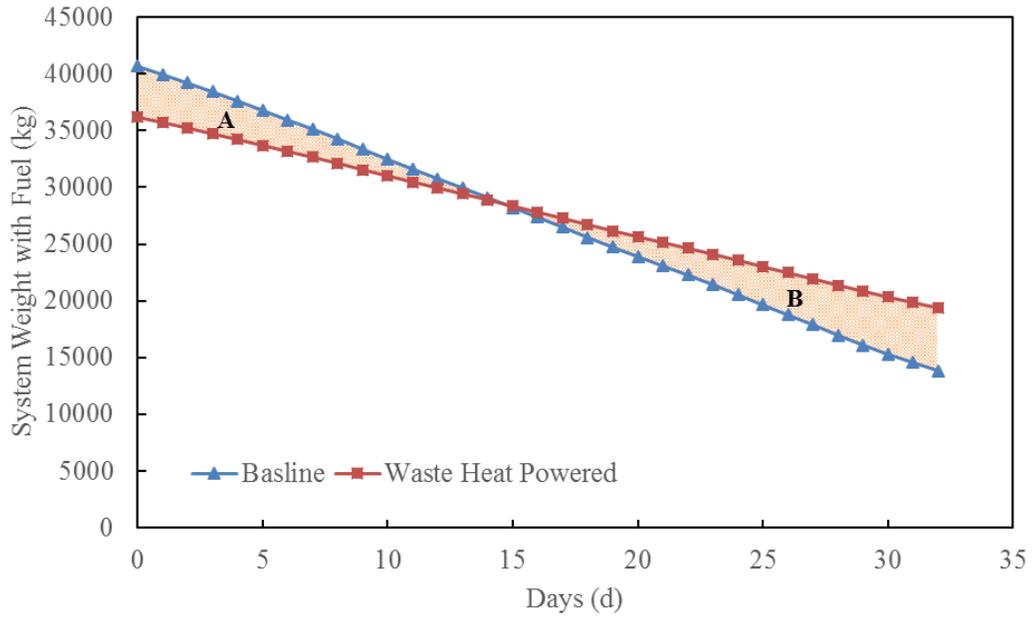
Figure 4-21: System weight comparison along the sea route

To understand the impact of system weight differences on the main engine fuel consumption, the admiralty coefficient [134] is introduced in Equation (4-11).

$$C = \frac{\Delta^{\frac{2}{3}}V^3}{P} \tag{4-11}$$

C is admiralty coefficient. Δ is ship mass displacement. V is ship speed and P is the main engine power. For similar ship designs, C can be considered constant. Assuming under both the baseline and WHP scenarios, the container ship sails at same speed. Therefore, the main engine powers have the following relation, stated as Equation (4-12).

$$\frac{P_w}{P_b} = \left(1 + \frac{\Delta_w - \Delta_b}{\Delta_b}\right)^{\frac{2}{3}} \tag{4-12}$$

119

Here w denotes WHP system, b denotes baseline system. For the whole sailing period, the aggregated weight differences are 15,810 kg, as shown in Equation (4-13).

$$\sum_{i=1}^{32}\left(\Delta_{w,i}-\Delta_{b,i}\right)=15810 \text{ kg} \tag{4-13}$$

For the container ship studied, we have

$$\frac{\sum_{i=1}^{32}\left(\Delta_{w,i}-\Delta_{b,i}\right)}{\Delta_{b}}<1\% \tag{4-14}$$

As a result,

$$\frac{P_{w}}{P_{b}}\approx 1 \tag{4-15}$$

In summary, the weight differences incurred by replacing the baseline system with the WHP system have negligible effects on the main engine fuel consumption.

Life cycle cost analysis has been performed for both systems. Three types of cost were considered – capital cost, maintenance cost and operational cost. For capital cost, following cost equations shown in Table 4-13 were adopted. Table 4-14 summarizes the capital cost of two systems. The WHP system has higher capital cost as it has more equipment than the baseline system. Also the absorption chiller cost is much higher than the compression chiller.

Table 4-13: Capital cost equation

Component	Capital Cost Equation ($)
Diesel generators [135]	$641.71\ Capacity$
Compression chiller [136]	$110.79\ Capacity + 2454.7$
Absorption chiller [136]	$147.3\ Capacity + 100680$
Boiler [136]	$-0.0139\ Capacity^2 + 42.756\ Capacity + 1990.1$
Economizer [137]	
Water to air heat exchanger [137]	$130 \left(\frac{Area}{0.093}\right)^{0.78}$
Waste heat recovery unit [137]	
Pumps [138]	$3540\ Power^{0.71}$

Table 4-14: Capital cost comparison

Equipment	Baseline ($)	WHP ($)
Diesel Generator	412,125	236,642
Compression Chiller	62,953	N/A
Absorption Chiller	N/A	246,497
Boiler	3,678	N/A
Economizer	N/A	578
Water to Air HX	N/A	24,382
WHR Unit	N/A	5,978
Auxiliary Pumps	1,748	26,241
Total Capital Cost	480,504	540,317

The equipment maintenance cost was assumed to be 2% of the capital cost [139]. The operational cost is the fuel cost associated with operating two systems. The simulated sailing period is from 6/8 to 7/20. For simplicity, the ship was assumed to sail the seam route six times per year. The heavy fuel price was $360 per ton [140]. The lifetime span of the system was assumed to be 25 years. Net present values (NPV) of both systems were calculated and the definition is given in Equation (4-16).

$$NPV = \sum_{t=0}^{N} \frac{R_t}{(1+i)^t} = CC + \frac{MC+OC}{(1+i)^1} + \cdots + \frac{MC+OC}{(1+i)^N} \qquad (4\text{-}16)$$

Here CC, MC, OC are short for capital cost, maintenance cost and operational cost, respectively. Symbol i is the discount rate, here 10% is taken, a commonly used value in energy system life cycle cost analysis. Table 4-15 summarizes the life cycle cost of both systems. Though the WHP system has higher capital cost, NPV of the WHP system is 88% of the baseline system.

Table 4-15: Life cycle cost analysis

Index	Baseline	Waste Heat Powered
Capital Cost ($)	480,504	540,317
Annual Maintenance Cost ($/year)	9,610	10,806
Annual Fuel Consumption (MT)	161	101
Annual Operational Cost ($/year)	57,931	36,266
Net Present Value ($)	1,093,579	967,599
R_{NPV}	0.88	

The NPV was further investigated on a yearly basis to determine payback period. Figure 4-22 plots NPVs of two systems along the life time span. The payback period is the time when two systems reaches the same NPV. From Figure 4-22 it was determined to be 4 years.
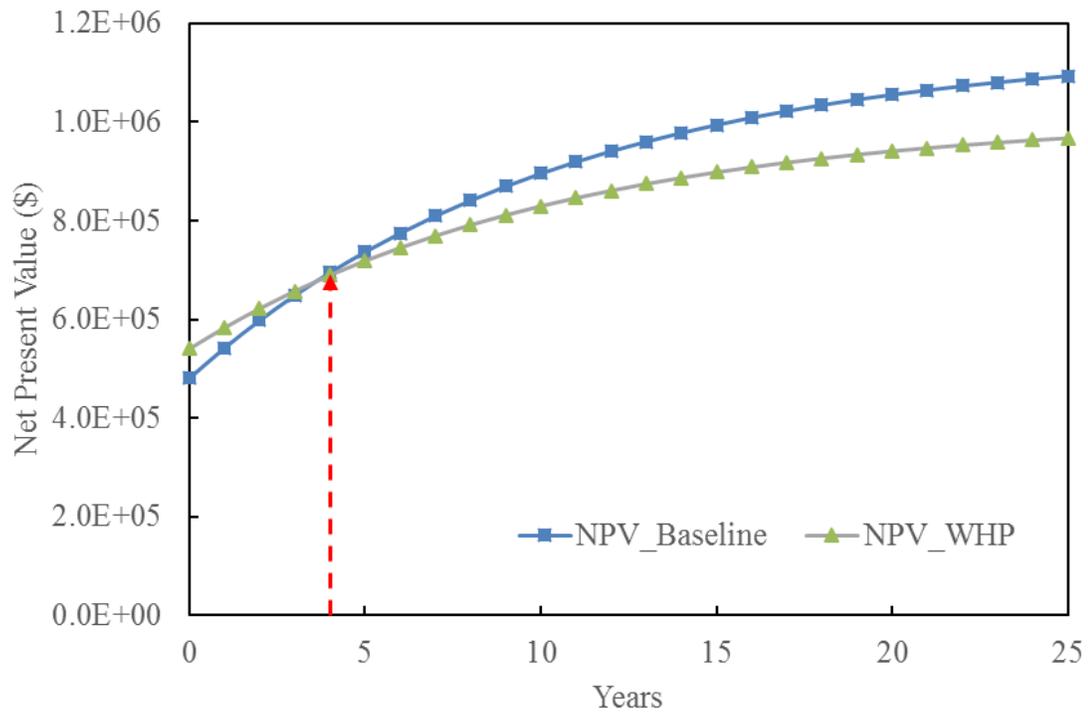
Figure 4-22: Net present value comparison

4.3   Challenges and Discussions

Moving absorption cooling system to a shipboard application faces new challenges brought by ship motion and sea climates. There are three major concerns: anti-swaying, anti-vibration and anti-corrosion [141].

The swaying and vibration brought by ship motions may improve the heat and mass transfer to some extent, due to the improved flow conditions. However, it may also degrade the heat exchanger performance. Consider shell-and-tube heat exchangers, which are frequently used in cooling systems as condensers or generators. The falling film formed will depart the tubes due to swaying if they are designed in vertical ways, thus lose

performance to some extent [142]. To prevent performance degradation, horizontal tube layout or fully merged tube design can be applied [143].

Anti-corrosion is a common concern for ship design. In this study, the main focus is heat exchangers as the condenser and absorber are sea water cooled. There have been some studies on heat exchanger corrosion issues [144]. One of the solutions is the anti-corrosion coasting, as investigated by L. Fedrizzi (2008) [145]. Besides, the absorption chiller should be located in a dry, under deck cabin, in which the ventilation air needs to be processed to lower humidity level.

4.4   Summary

In the first part, two solar powered microgrid systems have been simulated with TRNSYS to provide space cooling for up to 1,194 guest rooms for a container ship. The control strategies have been set up. The zone temperature was well controlled with temperature fluctuation less than 2.7°C. Parametric study was conducted on battery size. The optimum battery cell numbers were determined based on solar power fraction, yearly performance factor and PV utilization fraction. Simulation results show that the optimized PV system can reduce the yearly fuel consumption and life time GHG emissions by 98% and 93%, respectively as compared to the baseline system. For ETC system, it can reduce these two indexes by 78% and 75%, respectively. The optimized PV system adds 4,817 kg net weight to the ship, while the ETC system reduces the weight by 6,788 kg. The cost analysis shows that the ETC system has lowest total life time cost, which is only 28% of the baseline system and 23% of the optimized PV system.

In the second part, transient simulation of the engine waste heat powered ABC cooling system for cruise ship application was conducted in TRNSYS platform. The waste heat powered cooling system was simulated under Miami weather condition and compared with the baseline VCC cooling system. The space conditions indicate a reasonable system design and robust control under Miami condition. The waste heat powered cooling system shows a cooling COP of 0.6, versus 3.6 of the baseline. If the waste heat energy is considered "free", the COP could be up to 9.4. The fuel consumption and CO_2 emission of the waste heat powered cooling system are 62% less than that of the baseline. The cooling system performance was also investigated under different locations. It was found that the fuel consumption and CO_2 emission reductions increase up to 68% under hotter conditions (Abu Dhabi), while decrease to 38% under colder conditions (Baltimore). Applying the waste heat powered absorption cycle cooling system in the cruise ship can save the total energy by 8.23%.

In the third part, the WHP system was applied to the container ship to meet space heating, space cooling and refrigeration demands. The WHP system employs the waste heat powered ABC for space cooling. The waste heat is also utilized for heating directly. The cascaded absorption-compression cooling configuration is utilized for reefer units, with a novel layout to minimize duct and pipe work. Both the WHP system and baseline system were simulated on TRNSYS for two sailing routes. The baseline system simulation results were validated against experimental data regarding air-conditioning and reefer unit power consumptions. The CVRMSEs of air-conditioning unit and reefer unit validations are 9% and 27%, respectively, indicating satisfying agreements. Simulation results reveal that the WHP system is able to reduce the fuel consumption and CO_2 emission by 38%.

The diesel engine capacity could also be reduced by 40%. Sankey diagrams were created to analyze the energy and CO_2 emission flow of both systems. Direct emissions from diesel generators are dominant CO_2 emission factors in both systems. Alternative sea route comparison indicates hotter climate is in favor of the proposed WHP system regarding fuel savings.

Payload and life cycle cost analysis is performed on the proposed WHP system and baseline system. Differences on weight between two systems have negligible impacts on the main engine fuel consumption. NPV of the WHP system is only 88% of the baseline system. The payback period of the WHP system is four years. Challenges to absorption cooling system on shipboard applications are also addressed by suggesting potential solutions.

5 Microgrid System Optimization

5.1 Background

The objective of the study is to develop an advanced optimization based design framework, which is able to find optimal system configurations and control strategies for any given equipment options and load/weather profiles. Comprehensive correlation based equipment models were developed, including cascaded systems. The design framework was demonstrated through a case study on an oceanic transportation application. This study addresses following research gaps compared to previous studies:

- Develop an optimization based design framework which could optimize not only system control strategies but also system configurations, i.e., equipment selections.

- Develop comprehensive cycle models including cooling, heating, power and refrigeration cycles. Possible integration among cycles was also considered, such as absorption-compression refrigeration cycle.

- Comprehensively analyzed results through three different optimization perspectives: single-objective, bi-objective and optimization under uncertainty.

- Time-variant load and weather profiles have been considered, as well as their impacts on equipment performance.

- This study focused on off-grid transportation applications.

5.2 Equipment Modeling

This study focuses on microgrid energy system optimization, specifically for transportation applications. The selected system aims to provide cooling, heating, refrigeration and auxiliary power demands for transportation applications, such as a container ship. Such applications usually have no access to grid power. Instead energy could be supplied from power generation units and waste heat from combustion engines.

Component modeling is a prerequisite to preform system optimization. Correlation based models were developed for cooling, heating, power and refrigeration equipment that can be used for any microgrid system applications [146]. Table 5-1 shows energy conversion options from energy supplies to energy demands. In this study, five different energy demands are considered: space cooling, refrigeration, space heating, water heating and auxiliary power for fans and pumps. Three energy sources are available: fuel energy, waste heat and electricity from diesel generators. There were eight equipment modeled based on the energy conversion chart. Each equipment model is introduced in detail as following.

Table 5-1: Energy conversion chart

Energy Supply / Energy Demands	Fuel	Diesel Generator Electricity	Waste Heat
Auxiliary Power	PGU	-	ORC
Space Cooling	-	VCC Chiller	ABC
Refrigeration	-	VCC Reefer	-
Space Heating	Boiler	Electric Heater	Direct Waste Heat
Water Heating	Boiler	Electric Heater	Direct Waste Heat

The power generation unit (PGU) converts fuel energy into electricity. Its efficiency is defined as the electric energy output over fuel energy input, as shown in Equation (5-1). The efficiency of PGU varies with part load ratio (PLR) as in Equation (5-2) [147]. The efficiency increases with PLR nonlinearly, reaching maximum (25%) at full loads.

$$\eta_{PGU} = \frac{W_{output}}{Q_{fuel}} \tag{5-1}$$

$$\eta_{PGU} = a + b \cdot PLR + c \cdot PLR^2 + d \cdot PLR^3 \tag{5-2}$$

Where coefficients a, b, c and d were set as 8.935, 33.157, -27.081, 9.9892, respectively.

The organic Rankine cycle (ORC) transforms thermal energy into electricity. The efficiency is the ratio of electricity energy output over heat energy input, as in Equation (5-3). The condenser of the ORC is water-cooled. Its full load efficiency varies with cooling water temperature as in Equation (5-4), based on modeling results from EES. R-245fa is used as the working fluid. The sea water temperature could vary from 16 to 32°C, as found from sea route weather profiles. The part load efficiency of ORC relies on a variety of factors depending on its sub-component (turbine, pump and heat exchangers). For simplicity, a constant part load efficiency was used, as proposed by Erhart et al. [148].

$$\eta_{ORC} = \frac{W_{out}}{Q_{in}} \tag{5-3}$$

$$\eta_{ORC} = -0.001357 T_w + 0.161708 \tag{5-4}$$

The vapor compression chiller was modeled based on standard type 666 from transient systems simulation program (TRNSYS). Its coefficient of performance (COP) is

defined in Equation (5-5). The vapor compression chiller is water-cooled. Its COP under full load changes with water temperature as Equation (5-6), based on EES program modeling results. The fluctuation range of water temperature is 16 to 32°C, as mentioned earlier. The part load performance of vapor compression chiller is shown in Equation (5-7) [149]. As part load increases, its performance increases nonlinearly, reaching maximum at full loads.

$$COP_{compression\_chiller} = \frac{Q_{evaporator}}{W_{compressor}} \qquad (5\text{-}5)$$

$$COP_{compression\_chiller} = -0.116661T_w + 7.914392 \qquad (5\text{-}6)$$

$$COP_{PLR} = COP\big|_{PLR=100\%} \frac{PLR}{0.1+0.9PLR} \qquad (5\text{-}7)$$

The water-cooled absorption chiller converts thermal energy to cooling energy, with its COP defined in Equation (5-8). It uses H_2O/LiBr as working fluid. Its full load performance varies with water temperature as in Equation (5-9), based on the model introduced in [150]. The application range of water temperature is from 16 to 32°C. The part load performance is given in Equation (5-10) [151]. It increases with part load ratio, though varies in a small range (less than 0.1).

$$COP_{absorption\_chiller} = \frac{Q_{evaporator}}{Q_{generator}+W_{sp}} \qquad (5\text{-}8)$$

$$COP_{absorption\_chiller} = -0.002013T_w + 0.744334 \qquad (5\text{-}9)$$

$$COP_{PLR} = COP\big|_{PLR=100\%} \frac{1}{1.13-0.13PLR} \qquad (5\text{-}10)$$

The refrigeration demands refer to subzero cooling demands, usually coming from reefer containers. The vapor compression refrigeration unit is able to provide cooling energy ranging from -30°C to 0°C, with COP defined in Equation (5-11). It is usually air-cooled. R-404A is used as the working fluid. While ambient air is the most common cooling source, the refrigeration unit could also be coupled with vapor compression or absorption chiller and cooled by low temperature (~12°C) cool air. The cool air is cooled by chilled water from chillers. Such configuration is called cascaded cooling-refrigeration system and introduced in detail in [146] and Chapter 4.2.2.1. The advantage of cascaded system over standalone refrigeration system is that the refrigeration unit condenser operates at lower pressure due to lower cooling air temperature. Hence the refrigeration unit in cascaded system consumes less electricity.

$$COP_{refrigeration} = \frac{Q_{evaporator}}{W_{compressor}} \qquad (5\text{-}11)$$

A binary variable α (α is either 0 or 1) is used to indicate whether refrigeration units work under cascaded or standalone configurations, with zero indicating standalone configuration and one representing cascaded configuration. When the refrigeration unit works as standalone system, its full load performance varies with ambient temperature, based on the meta-model as introduced in [146] and Chapter 3.1.2. When the refrigeration unit works as cascaded system, its COP can be considered as constant since the cooling air temperature is relatively constant. Therefore, the refrigeration unit's full load COP can be expressed as Equation (5-12). Air temperature could vary from 16 to 39°C, based on air temperature fluctuation range from sea route weather profiles. The part load performance is presented in Equation (5-13) [149]. It increases linearly with PLR.

$$COP_{refrigeration} = (1-\alpha)\cdot(-0.032737T_{air} + 2.190436) + 2.018\alpha \qquad (5\text{-}12)$$

$$COP_{PLR} = COP\big|_{PLR=100\%}[1-0.75(1-PLR)] \qquad (5\text{-}13)$$

Under the cascaded configuration, the condensers of refrigeration units reject heat to chilled water from chillers, therefore increasing cooling loads of vapor compression or absorption chillers. As such, chiller cooling loads (evaporator capacities) follows Equation (5-14). $Q_{cooling}$ represents space cooling loads while $Q_{condenser}$ represents condenser loads from refrigeration units.

$$Q_{evaporator} = (1-\alpha)\times Q_{cooling} + \alpha\times(Q_{cooling} + Q_{condenser}) \qquad (5\text{-}14)$$

The boiler converts fuel energy to thermal energy. Its efficiency is defined in Equation (5-15), with a full load efficiency as 82%. Its part load performance is shown in Equation (5-16) [152]. The part load efficiency increases dramatically at low part load ratios and then becomes relatively stable near full loads.

$$\eta_{boiler} = \frac{Q_{heating}}{Q_{fuel}} \qquad (5\text{-}15)$$

$$\eta_{PLR} = \frac{1.572PLR}{(0.1745 + 1.744PLR)} \qquad (5\text{-}16)$$

Electric heaters convert electricity into heat at constant efficiency of one, presented in Equation (5-17).

$$W_{electricity} = Q_{heat} \qquad (5\text{-}17)$$

The direct heating equipment utilizes waste heat for space heating or water heating. There are two waste heat sources: external waste heat from industrial processes or

combustion engines and rejected heat from ORC condensers. When utilizing condenser heat from ORC, direct heating and ORC form a cascaded heating system. Similarly to cascaded cooling-refrigeration system, a binary variable β (β is either 0 or 1) is used to indicate whether cascade heating does exist or not. When β equals to zero it means no cascaded heating system layout. Hence the direct heating energy flow can be presented as Equation (5-18). Q_{heatin} represents external waste heat source while $Q_{ORCcondenser}$ represents the portion of rejected heat from ORC condensers used for direct heating. Keep in mind that variables α and β are two independent variables, therefore the cooling and heating loads in Equation (5-14) and (5-18) are for two independent systems.

$$Q_{heatout} = \beta(Q_{heatin} + Q_{ORCcondenser}) + (1 - \beta)Q_{heatin} \qquad (5\text{-}18)$$

Table 5-2 summarizes the equipment model type and whether they are affected by external weather data. It can be seen that most equipment models are non-linear correlations based and impacted by time variant weather data. Therefore, the optimization problem is highly nonlinear and time dependent, which needs a proper formulation and approach to handle.

Table 5-2: Energy conversion equipment model overview

Equipment Type	Equipment	Model Type	Weather Affected
Power	PGU	Nonlinear Equations	No
	ORC	Linear Equations	Yes
Cooling	VCC Chiller	Nonlinear Equations	Yes
	ABC	Nonlinear Equations	Yes
	VCC Reefer	Nonlinear Equations	Yes
Heating	Boiler	Nonlinear Equations	No
	Electric	Linear Equations	No
	Direct Heat	Linear Equations	No

5.3   Problem Formulation

In this chapter, the general problem formulation for single-objective optimization is introduced in detail. Later, the formulated problem is expanded to bi-objective optimization and optimization under uncertainty, which are introduced in detail in later chapters.

For single-objective optimization, the goal is to minimize system life cycle cost (LCC), which is defined as Equation (5-19).

$$LCC = CC + \sum_{i=1}^{N} \frac{MC + OC}{(1+d)^i} \qquad (5\text{-}19)$$

Where CC, MC and OC represent capital cost, maintenance cost and operational cost, respectively.

The capital cost of each equipment was simplified as a function of their capacity as listed in Table 5-3. The maintenance cost was assumed to be 2% of the capital cost. The operational cost is the primary energy consumption cost such as fuels. Waste heat was considered as "free" energy. N is the life time of the energy system, usually taken as 25

years for typical cogeneration energy systems. Symbol d is the inflation rate. Here 10% was chosen as it is a typical value used in the open literature.

Table 5-3: Equipment capital cost

Equipment	Capital Cost Function ($)
ORC [153]	$945*W_{ORC}$
VCC Reefer [154]	$128.45*Q_{reefer} + 6622.2$
VCC Chiller [154]	$110.79*Q_{chiller} + 2454.7$
ABC [154]	$147.3*Q_{ABC} + 100680$
Boiler [154]	$42.756*Q_{boiler} + 1990.1 - 0.0139*Q_{boiler}^2$
Heater [154]	$60*Q_{heater}$
Direct Heat [155]	$28*Q_{directheatout}$
PGU [156]	$641.71*W_{PGU}$

There are three types of design variables: equipment existence in the form of binary variables, equipment capacity and part load ratios in the form of continuous variables. In addition to design variables, there are three types of parameters needed: weather data, loads (cooling, refrigeration, heating and auxiliary power) and available external waste heat at each time step.

Equipment existence can either be zero or one, with one indicating being selected and zero not. Equipment capacities are non-negative variables, with lower bounds as zero and upper bounds as functions of loads and available external waste heat. Note equipment existence and capacity are time independent. Therefore, they are unique variables for each equipment. Equipment part load ratios are continuous variables ranging from zero to one. Note part load ratios are time dependent. Therefore, the part load ratio at each time step is considered as an independent variable.

There are three types of constraints beyond upper and lower bounds of design variables. The first type is for cascaded system layout. A cascaded system will not exist if

any involved equipment is not selected. As an example, if either absorption chiller or vapor compression refrigeration unit is non-existent, the cascaded absorption-compression cooling system will not exist. Such logic is expressed in Equation (5-20).

$$\alpha_1 \leq \min(\delta_1, \delta_2) \tag{5-20}$$

Where α_1 means the existence of a cascaded cooling system, δ_1 and δ_2 represent existence of absorption chiller and refrigeration unit, respectively.

The second type of constraint is system load fulfillment. For any category of loads, energy supplied should be larger than or equal to energy demands. To prevent excessive energy supply, an upper bound was imposed. Equation (5-21) shows the cooling load fulfillment. Here α was set to be 1.2, a typical value of safety factor for equipment sizing. Similar constraints were implemented for refrigeration, heating and power demands. The waste heat utilized should also be less than or equal to available waste heat. The third type of constraint is the control strategy of equipment. The part load ratio of each equipment cannot fluctuate randomly. Instead, it should fluctuate within a certain range based on value from previous time step. Such constraint exists due to response lag to control signal and safety protection for each equipment. The general expression is presented in Equation (5-22). Here b was set to be 0.33, considering a three hours startup and shutdown period for all equipment.

$$Q_{cooling} \leq Q_{compression\_chiller} + Q_{absorption\_chiller} \leq \alpha \cdot Q_{cooling} \tag{5-21}$$

$$PLR_{i-1} - b \leq PLR_i \leq PLR_{i-1} + b \tag{5-22}$$

The upper bounds of load fulfillment constraints, along with equipment control strategy constraints, are typically missing in recent studies on energy system optimizations. However, these constraints should be included as discussed later.

In a summary, the complete mathematical formulation of the single-objective optimization problem is presented in Equation (5-23).

$$
\begin{aligned}
&\min F(x, y, z, p(t)) \\
&s.t.\ G(x, y, z, p(t)) \leq 0 \\
&0 \leq y_i \leq f(p(t)) \\
&0 \leq z_i \leq x_i \\
&x_i \in \{0,1\}, i = 1, 2, \dots \\
&y_i \in R_+, i = 1, 2, \dots \\
&z_i \in R_+, i = 1, 2, \dots \\
&p(t)_i \in R_+, t = 1, 2, \dots
\end{aligned}
\tag{5-23}
$$

Where F represents the objective function, G represents constraints, x, y, z and p refer to binary variables, continuous variables (equipment capacity), continuous variables (equipment part load ratios) and parameters, respectively. Symbol i means different equipment and symbol t means each time step.

5.4 Optimization Approach

As introduced in the component modeling and problem formulation, the optimization problem can be categorized as mixed integer non-linear programming. Further mathematical deductions proved the problem is non-convex. Genetic algorithm (GA) was chosen to solve the problem. In particular, the genetic algorithm toolbox from MATLAB [157] was selected for its capability to handle integer variables and non-linear constraints.

Figure 5-1 shows the optimization flow chart. First new designs (including system configuration as well as control strategies at each time step) are generated, either by genetic algorithm toolbox or user defined inputs. Then the design is evaluated in preparation for constraints and objective calculations. There are three steps in design evaluation: equipment performance evaluation (including full load and part load performance), equipment energy flow evaluation (including energy input and output for each equipment) and equipment cost valuation (including capital cost, maintenance cost and operational cost of each equipment). Following next, evaluation results are checked against constraints. As stated before, three types of constraints are evaluated for a reasonable design: cascaded system layout, loads fulfillment and equipment control strategies. Those designs not satisfying constraints are discarded while the ones satisfying constraints are calculated for objectives. The optimization toolbox then compares design results and selects the one with optimal objective values.

It is admitted that genetic algorithm, like any other evolutionary algorithm, cannot guarantee whether results are global optimal or not. To enhance the confidence on final results, the optimization program was set up with several different initial populations with sufficiently large population size, as suggested by [158]. Besides, comparison studies were conducted for a simplified problem using genetic algorithm solver from MATLAB and BARON solver [159] from GAMS [160]. The simplified problem optimizes cooling systems under a three hours loading profile. There are three equipment options available: electricity powered vapor compression chiller, waste heat powered absorption chiller and adsorption chiller. The objective is to minimize life cycle cost. It was found optimization

results were the same using two different solvers. Therefore, genetic algorithm can be used to solve the complete problem with confidence on its convergences.

The proposed optimization program was applied to a specific application as a case study. In particular, microgrid energy systems on oceanic container transportation applications were selected. The microgrid energy system refers to energy systems for onboard cooling, heating, refrigeration (from reefer containers), and auxiliary power (apart from propulsions for ships) generations. The container ship sails between Pusan, Korea and Karachi, Pakistan for about 800 hours. Weather, load and waste heat profiles were obtained based on modeling results, which were validated against experimental data. Details regarding modeling results can be found at [146]. For simplicity, the container ship was assumed to operate about six times per year under this sear route, continuously for 25 years. The fuel price was assumed as $360 per ton [161].
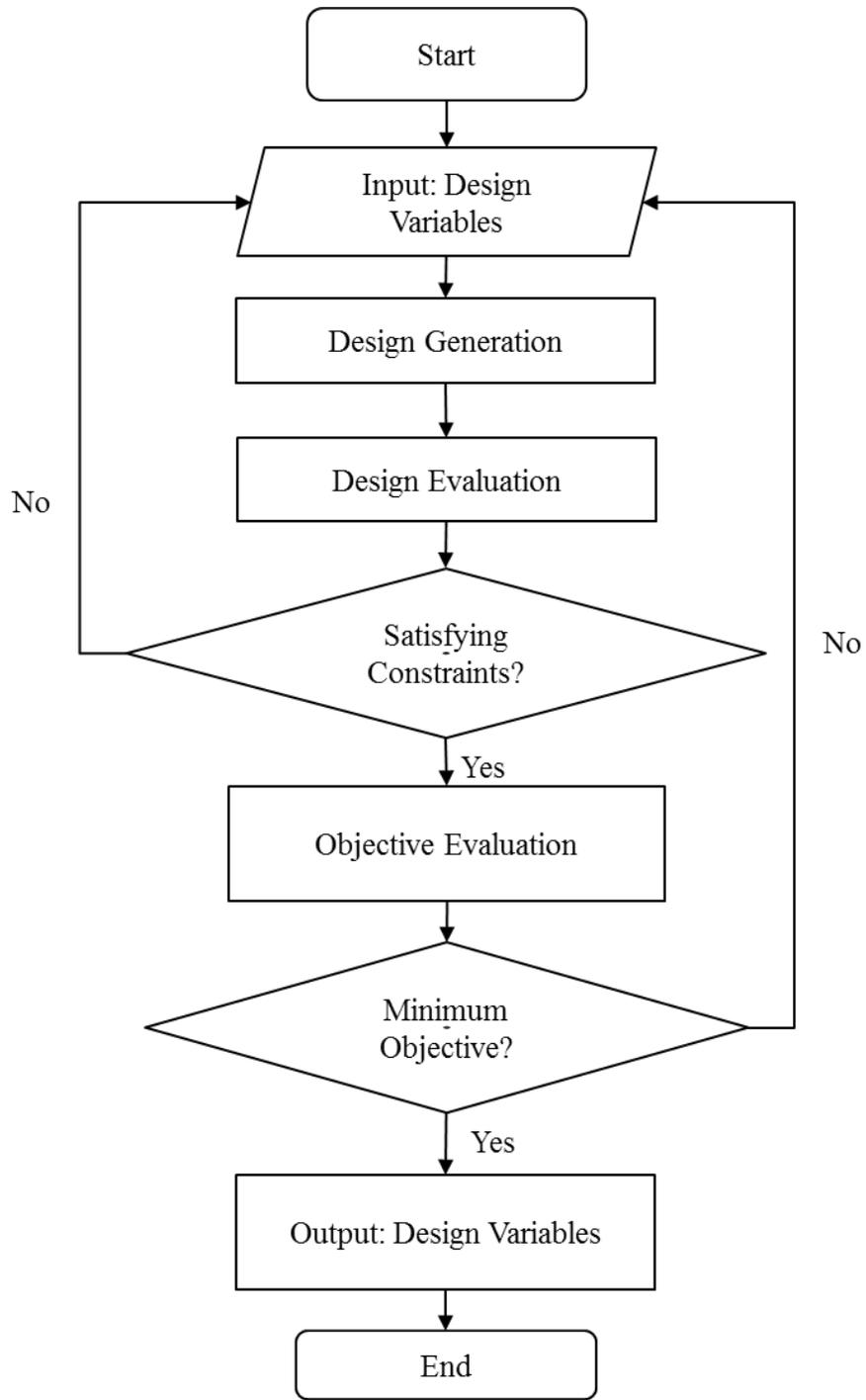
Figure 5-1: Single-objective optimization flow chart

5.5 Case Study

5.5.1 Single-objective Optimization

In this section, single-objective optimization results based on aforementioned case are presented in detail. First, system configurations – both the optimized and baseline systems were studied. Figure 5-2 shows the system configuration for the baseline system, which is the current design for the container ship. Nominal capacities are listed in the brackets below each equipment. Life cycle cost of the baseline system is 2.03 million USD. It is observed that the baseline system purely depends on fuel energy as its primary energy supply. Most of the fuel energy is supplied to PGU to generate electricity. The electricity is mostly supplied to vapor compression chiller for space cooling demands, followed by vapor compression refrigeration unit for refrigeration demands. The remaining portion is used by pumps and fans as auxiliary power demands. The remaining fuel energy is used for the boiler to meet heating demands. To evaluate the overall system performance, an index – primary energy ratio (PER) is introduced. The PER is defined as the total energy supplied over total fuel energy inputs, shown in Equation (5-24). The baseline system has a PER of 0.56.

$$PER = \frac{Q_{spacecooling} + Q_{spaceheating} + Q_{waterheating} + Q_{refrigeration} + Q_{auxiliary}}{Q_{fuel}} \quad (5\text{-}24)$$
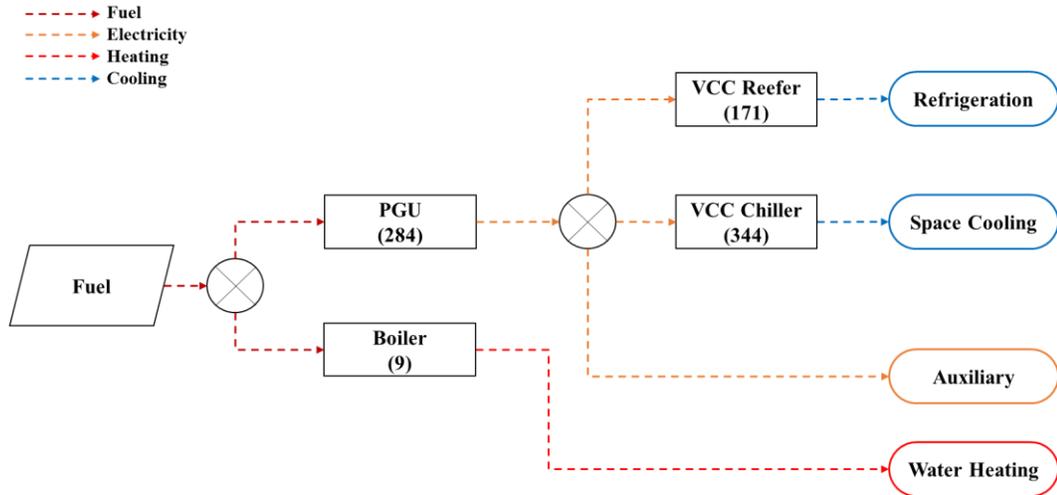
Figure 5-2: System configuration of the baseline system

Figure 5-3 presents the schematic of the optimized system. The optimized system uses direct heating to meet heating demands. Heat supplies come from direct waste heat and condenser heat of ORC. Space cooling demands are fulfilled by absorption chiller and vapor compression chiller. Part of the waste heat is employed to drive absorption cycle while the remaining is used by ORC. The ORC, together with PGU, produces electricity for vapor compression chiller, refrigeration unit and auxiliary power. The optimized system has a life cycle cost of 1.22 million USD, which is 40% less than that of the baseline. Waste heat utilization contributes most to the life cycle cost reduction. The optimized system utilizes waste heat powered equipment to meet all heating demands and considerable portions of cooling, refrigeration and auxiliary demands. Therefore, the PGU can be downsized by 20% as compared to that of the baseline. While introducing new equipment increases system capital cost from 0.26 million USD to 0.51 million USD, the operational cost reduces from 1.73 million USD to 0.61 million USD. The maintenance cost varies from 0.05 million USD to 0.09 million USD. So it is obvious that the operational cost is

142

the dominant one leading to significant life cycle cost reductions. The reason for operational cost reductions is that waste heat powered units, such as direct heating and absorption chiller, do not have operational cost since waste heat energy is considered "free". The optimal system has a PER of 1.93, 2.4 times higher than the baseline.
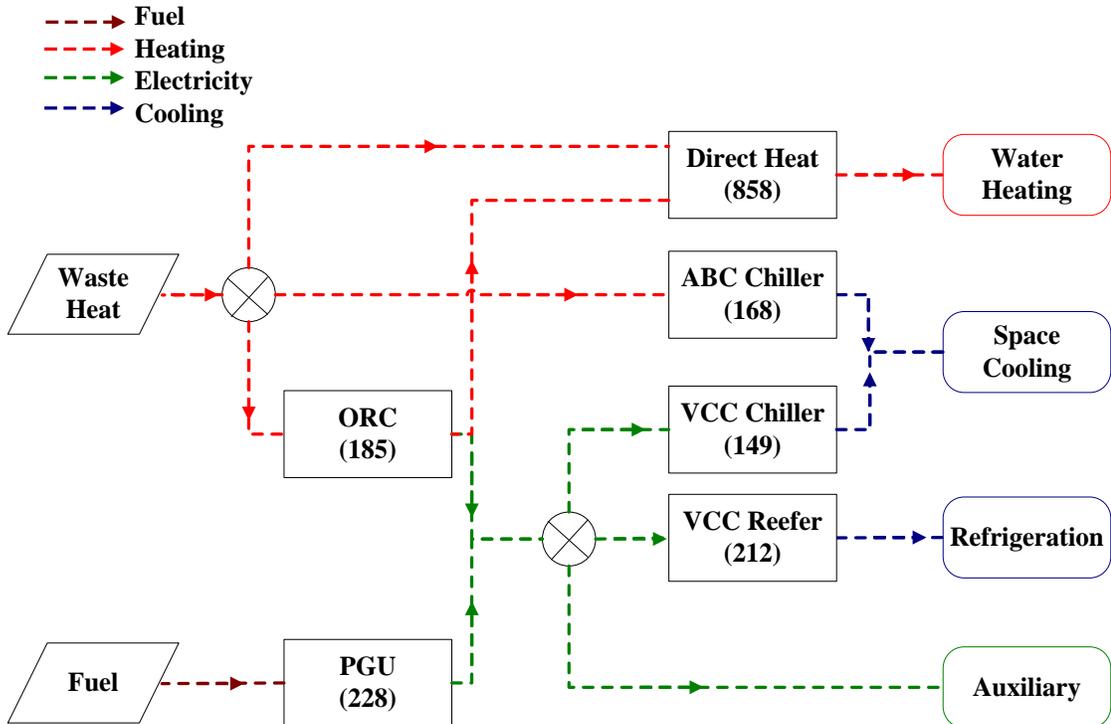
Figure 5-3: System configuration of the optimized system

As system configuration analysis reveals that waste heat utilization is the most important way to reduce system life cycle cost, further analysis was conducted to investigate how waste heat is utilized and how waste heat determines the optimal system configuration. Figure 5-4 shows waste heat utilizations under a sampling period – first 24 hours of the 800 hour sailing route. The waste heat utilization ratio is defined as the utilized waste heat over available waste heat. It is seen the optimized system has a high (>60%)

waste heat utilization ratio during most of time. The minimal available waste heat is the determent factor on optimized design as it defines the upper limit of the "free" energy source the system could explore throughout the sailing period. Particularly for Figure 5-4, it is 24th hour that determines the system design since it is when lowest available waste heat occurs. Indeed, the optimized design is already utilizing 100% waste heat at 24th hour. Note the 1st hour is neglected because all equipment are under start-up periods.
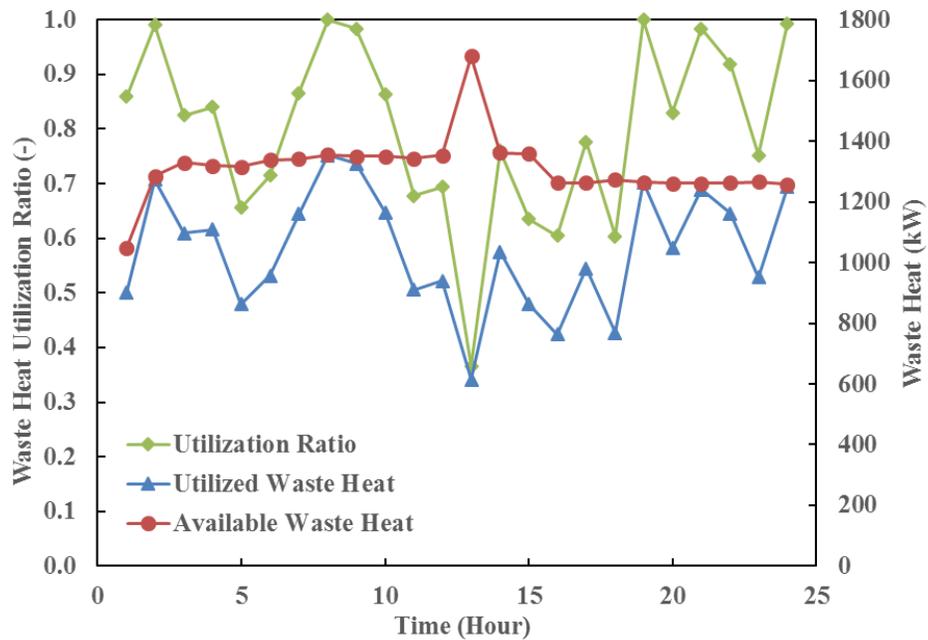
Figure 5-4: Waste heat utilization under the sampling period

To find the effect of minimal available waste heat on system fuel energy input, a parametric study was conducted, as shown in Figure 5-5. As expected, with increasing minimal available waste heat, the fuel energy input decreases. When the waste heat exceeds beyond 2,200 kW (about 25% of entire sailing period), fuel energy required decreases to zero, indicating fuel "free" system design is available.
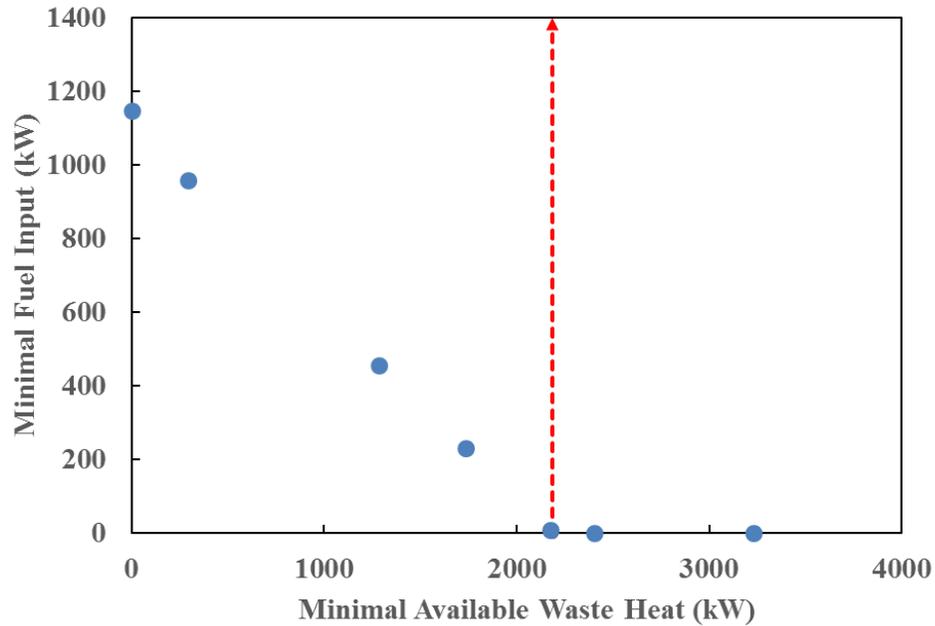
Figure 5-5: Minimal available waste heat vs. minimal fuel input

Further studies were conducted to explain why the upper bounds of load fulfillment constraints and equipment control constraints cannot be neglected. Figure 5-6 compares compression chiller part load ratios with and without control strategy constraints. As shown, the part load ratio fluctuates unrealistically when there are no equipment control strategy constraints. For instance, the part load ratio jumps from 0.1 to 0.9 from 4th hour to 5th hour. Such leaps would not be allowed in reality for safe operations. With the control strategy constraint imposed, the part load ratio fluctuates in a fairly reasonable range, less than the maximum value allowed (set as 0.33 in this study).
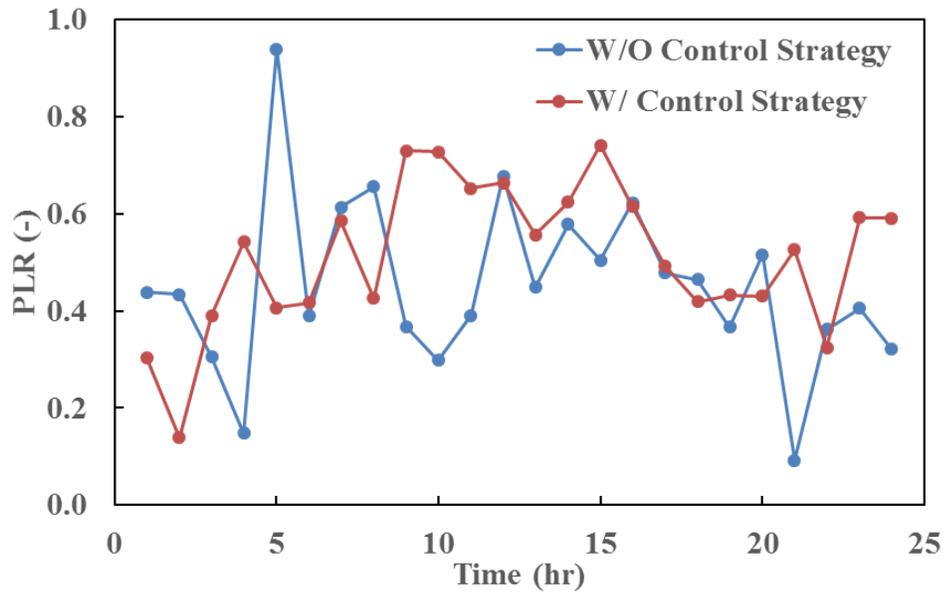
Figure 5-6: Comparison of compression chiller part load ratios w and w/o control strategy constraints

Figure 5-7 shows the cooling energy flow along with total cooling part load ratio when there is no upper bounds of load fulfillment constraints. It is observed the cooling energy supplied may exceed energy demanded significantly. Such oversizing would not be considered as a good design. It can be avoided by imposing upper bound limits to load fulfillment constraints.
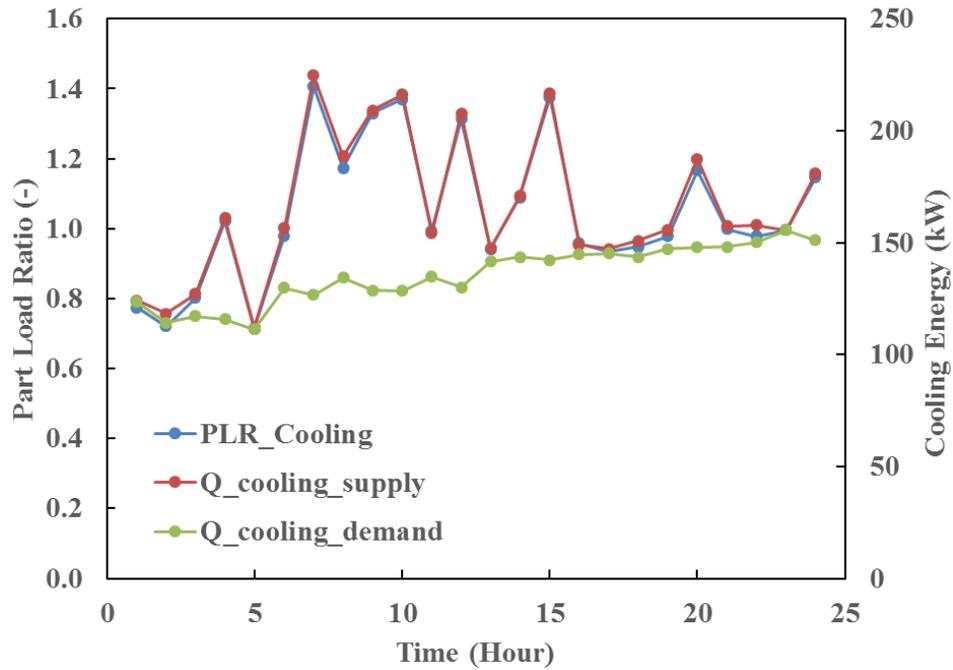
Figure 5-7: Cooling energy flow w/o upper bounds of load fulfillment constraints

5.5.2 Bi-objective Optimization

While single-objective optimization could provide optimal solutions from life cycle cost point of view, it does not reveal the trade-off relationship between capital investment and energy consumption. However, it is usually a major concern for decision makers due to limited budgets and consistent pursue for energy savings. Therefore, bi-objective optimization is conducted. Two objectives need to be minimized are system capital cost and annual fuel energy consumption. They were divided by baseline system capital cost and fuel energy consumption for convenience, as shown in Equations (5-25) and (5-26), respectively. For the baseline system (shown in Figure 5-2), the capital cost is calculated as 0.26 million USD and the annual fuel energy consumption is 5.74×10^6 kW·h.

$$\text{Capital Investment Ratio} = \frac{\text{Capital cost}}{\text{Baseline capital cost}} \qquad (5\text{-}25)$$

147

$$\text{Fuel Energy Consumption Ratio} = \frac{\text{Annual fuel energy consumption}}{\text{Baseline annual fuel energy consumption}}$$

$$(5\text{-}26)$$

The bi-objective optimization problem is formulated the same as the single-objective optimization problem, except for objectives. The problem was solved using MATLAB GA toolbox. Figure 5-8 shows an overview of optimization runs. The blue points are design cases from optimization runs. The red points are Pareto front solutions. Further optimization runs were performed using current Pareto front points as initial variables. However, no better optimization results than current Pareto front solutions were found. Therefore, current Pareto optimality is guaranteed.
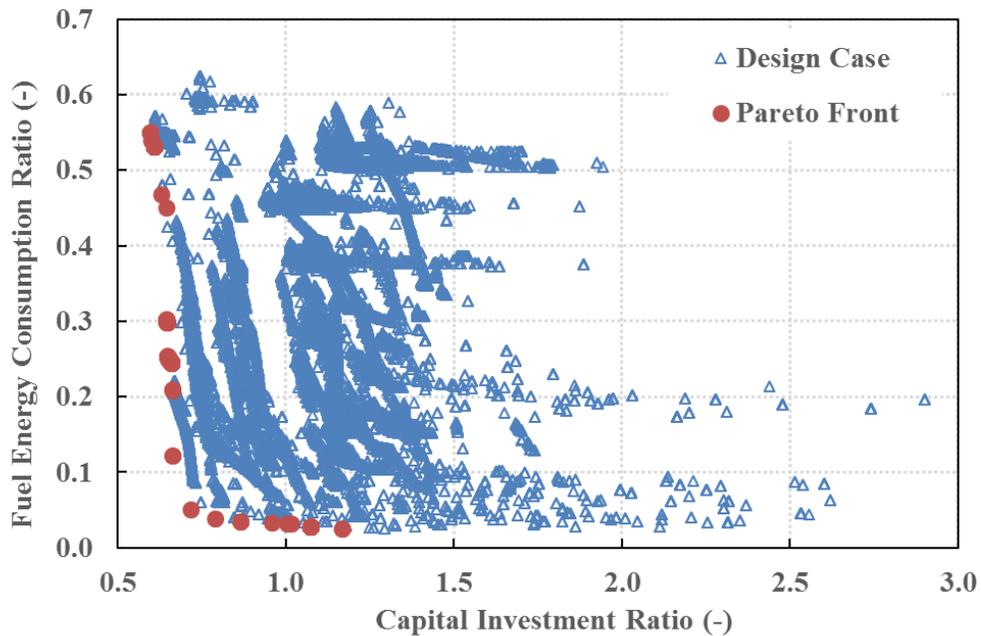
Figure 5-8: Overview of bi-objective optimization runs

Each Pareto front point represents a unique system design (equipment selection and capacity) and control strategy (equipment part load ratio). Figure 5-9 presents a detailed view on Pareto front solutions. The Pareto front solutions are categorized into 12 different cases based on equipment selections. Each case has exactly the same equipment existence, though equipment capacity and control strategy may be different. Further analysis on Pareto system design reveals that all Pareto solutions utilize waste heat as part of the primary energy supply to reduce fuel energy consumption. Regarding cooling energy generation, the vapor compression chiller is preferred over the absorption chiller due to high capital cost of absorption chiller. The cascaded cooling cycle is not preferred as it increases chiller capacity significantly, so does the capital cost. Regarding the power and heating generation, the Pareto front solution can be divided into three groups. The upper group cases do not employ ORC for power generation or cascaded heating generation. Instead, they rely on power generation unit and other heating methods (boiler or electric heater). As a result, their fuel saving potentials are limited, though their capital cost is low. One the contrary, the bottom group cases use ORC for power generation and direct heating for heating generation. Hence their capital cost is high (some are even higher than the baseline) while fuel consumptions are low. The middle group is named as mixed region as it has no clear preference on ORC and direct heating.
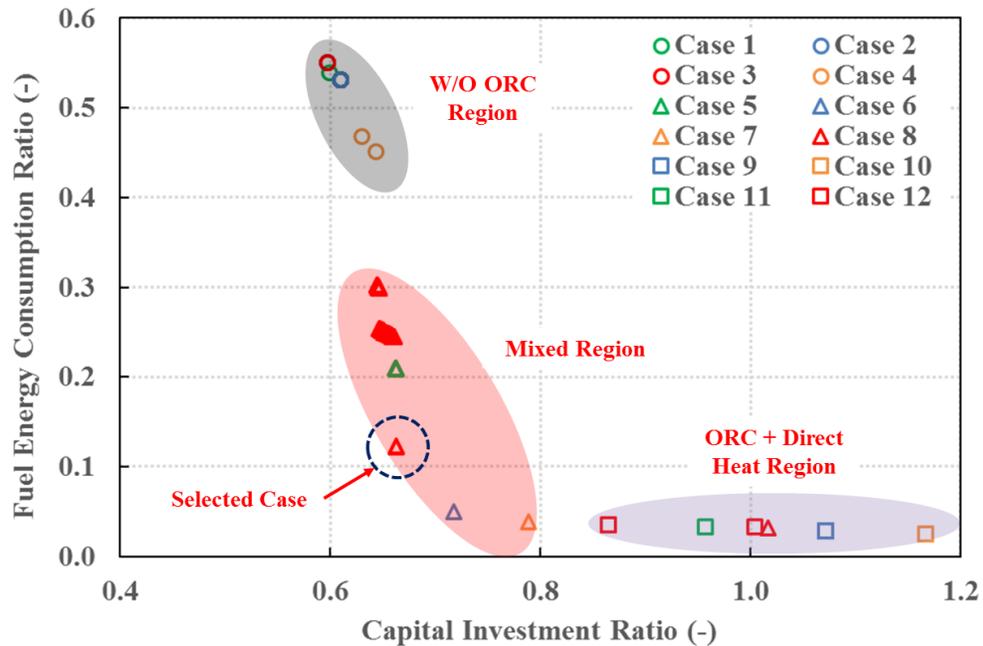
Figure 5-9: Detailed view on Pareto front solutions

A specific case is selected as the optimal design from Figure 5-9 as it has relatively good performance on both objectives. System configuration of the selected optimal design is presented in Figure 5-10. As can be seen, the system uses a combination of direct heating, boiler and electric heater to meet heating demands. Compared to the optimal system design from single-objective optimization, the direct heating capacity of the bi-objective optimization is much lower. The reason is the introduction of capacity cost as an objective to minimize. Therefore, equipment oversizing could be avoided. ORC and PGU provided all electricity demands for electric heater, refrigeration unit, chiller and auxiliary power demands. The optimal system has a capital cost of 0.17 million USD and annual fuel energy consumption of 7.03×10^5 kW·h. It reduces capital cost and annual fuel energy consumption by 34% and 88%, respectively.

150
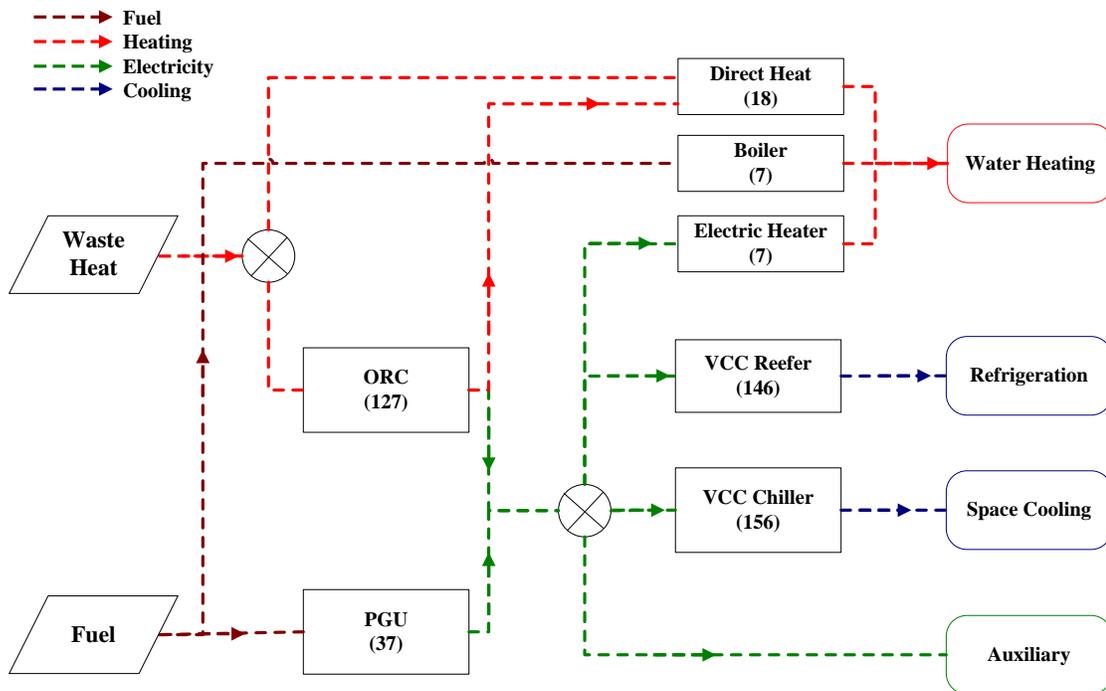
Figure 5-10: System configuration of the selected optimal design

Two more designs were selected to demonstrate differences among the three regions presented in Figure 5-9. Figure 5-11 and Figure 5-12 presents system configurations in w/o ORC region and ORC+ direct heat region, respectively. It is observed that adding ORC boosts up system capital cost significantly. Meanwhile it also reduces dependency on PGU, especially when most cooling and heating equipment are electricity powered (e.g. electric heater and vapor compression chiller).
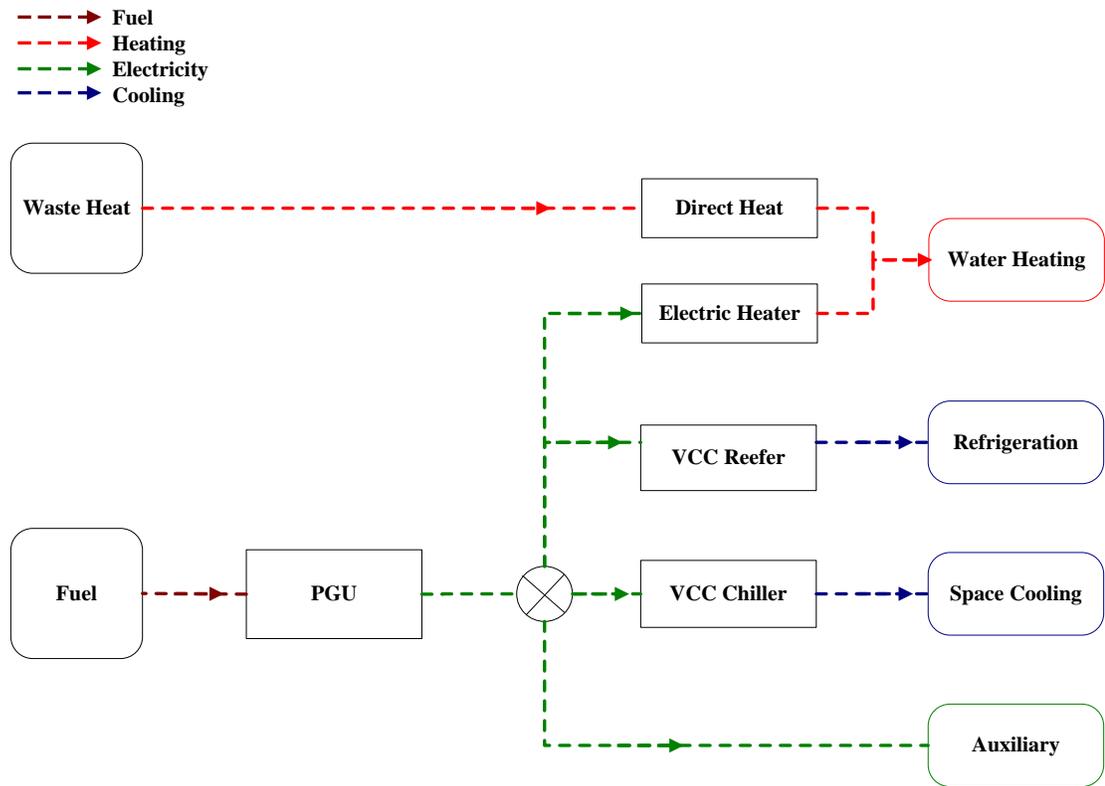
Figure 5-11: Representing system configuration in W/O ORC region
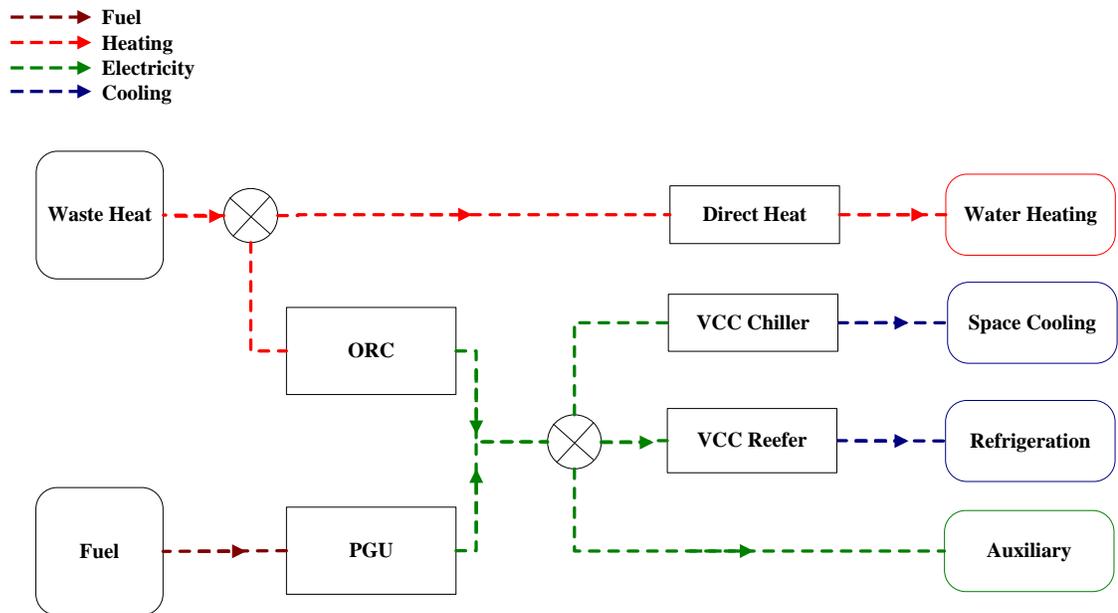
Figure 5-12: Representing system configuration in ORC+Direct Heat region

152

Further analysis was conducted on equipment control strategy. Different from single-objective optimization results, the waste heat utilized is fairly stable, indicating a consistent system control strategy. The waste heat is always prioritized for ORC for electricity productions, followed by direct heating. It is also observed the equipment operate at higher part load ratio overall than single-objective optimization results, due to reduced equipment capacities.

5.5.3 *Optimization under Uncertainty*

Previous single and bi-objective optimizations are confined with known load profiles. In other words, optimization results are valid only under given load profiles. However, load profiles may not be readily available when designing a system. Instead, decision makers need a system design valid for load profiles with certain ranges. Such system design is guaranteed to work under any load conditions falling within the ranges. Limits of ranges indicate extreme operation conditions, usually obtained from historical data or other simulation methods. Therefore, it is necessary to solve such an optimization problem: find the optimal system design under load profiles with uncertainties.

Optimization under uncertainty are a unique type of optimization problems. Depending on the form of uncertainties, three are two popular approaches to address such problems: stochastic programming and robust optimization. Stochastic programming is usually adopted when the uncertainty distribution form is known while robust optimization is able to solve the problem as long as uncertainty limits are given.

In the current case, uncertainties were introduced to energy demand and waste heat profiles. Such uncertainties are difficult to describe in the form of distributions as no clear

patterns can be observed from historical data. As a result, uncertainties are presented in the form of ranges with lower and upper limits. Limits are obtained from historical data and TRNSYS simulation data from the author's previous study [146].

As uncertainties are in the form of ranges, robust optimization approach is chosen to solve the problem. Robust optimization aims to find a solution such that worst-case cost is minimized. Details of robust optimization basics can be found at [162]. Usually a conservative index is introduced to reflect different levels of robustness, indicating validate ranges of optimization results. Open toolbox YALMIP [163] was used to solve the problem. The original problem was first formulated in MATLAB. Then a robust counterpart was derived by YALMIP toolbox, aiming to eliminate the uncertainties. The robust counterpart was then solved using external solvers such as FMINCON [164] and CPLEX [165].

Table 5-4 presents a list of upper and lower bounds of load profile uncertainties under different levels of conservativeness. When the conservative index equals zero, it means no uncertainty is introduced to the load profiles. Conversely, when conservative index equals to one, it means the load profiles may fluctuate within maximum ranges given. Apart from nominal scenarios – no uncertainty is introduced, five different conservative levels were introduced, ranging from 0.2 to 1.

Table 5-4: Uncertainties of parameters under different conservative levels

Type	0 (kW)	0.2 (kW)		0.4 (kW)		0.6 (kW)		0.8 (kW)		1 (kW)	
		LB	UB	LB	UB	LB	UB	LB	UB	LB	UB
Waste heat	1313	1260	1386	1207	1459	1155	1533	1102	1606	1050	1680
Refrigeration	124	120	128	115	133	111	137	107	142	103	146
Space cooling	136	131	140	126	144	121	148	116	152	111	156
Space heating	5.0	4.0	6.0	3.0	7.0	2.0	8.0	1.0	9.0	0.0	10.0
Water heating	10.0	9.6	10.4	9.2	10.8	8.8	11.2	8.4	11.6	8.0	12.0
Auxiliary	38.2	37.6	38.6	37.0	39.0	36.4	39.5	35.9	39.9	35.3	40.4

With load profile uncertainties introduced, optimal system designs were found at different conservative levels to minimize system life cycle cost. Figure 5-13 shows the optimized life cycle cost along with different conservative levels. It is seen that with increasing conservative index levels, the optimized system life cycle cost also increases. Therefore, there is a trade-off relationship between optimized system performance and its robustness. As the conservative level increases, robustness of the optimized system increases as it is able to operate under wider range of load profiles, however its performance regarding life cycle cost reduces. The most robust design (at conservative level of one) reduces life cycle cost by 45% from the baseline, compared to 52% of the leas robust design (at conservative level of zero). Note for this chapter of study only the first 24 hour of the 800-hour sea route profile was selected to scale down the problem to a reasonable size for solvers to handle. Hence results presented here are a little bit different from single-objective optimization results, which considered entire 800-hour sea route profile.
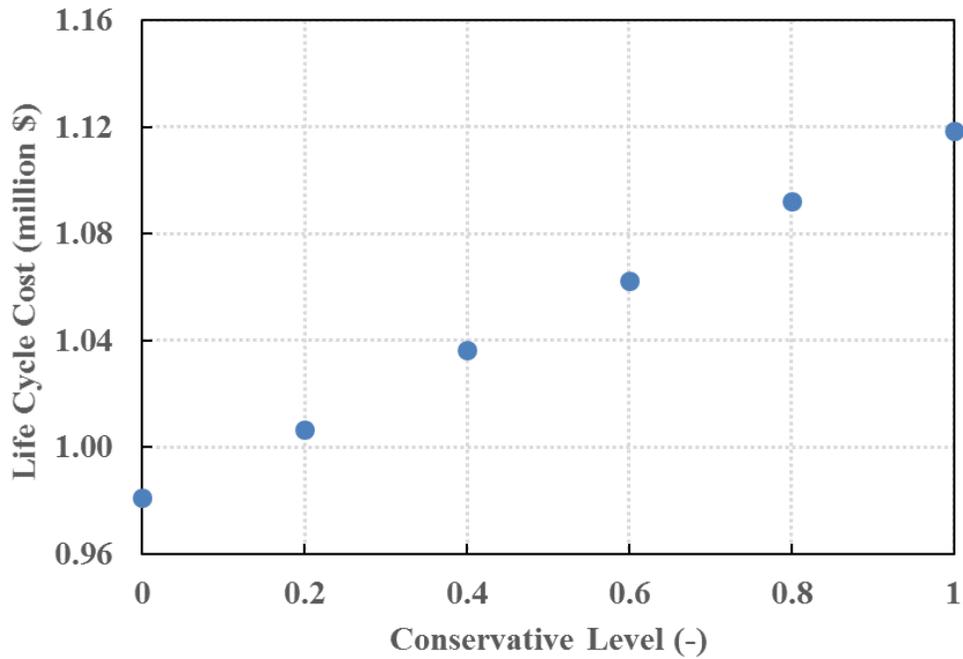
Figure 5-13: Optimized life cycle cost at different conservative levels

Figure 5-14 (a) and (b) present system designs for the least and most robust scenarios, respectively. As can be seen, waste heat is always utilized, though in different ways. For robust designs, waste heat is prioritized for direct heating. Also independent cycles are preferred over cascaded cycles or combined equipment layout for robustness.
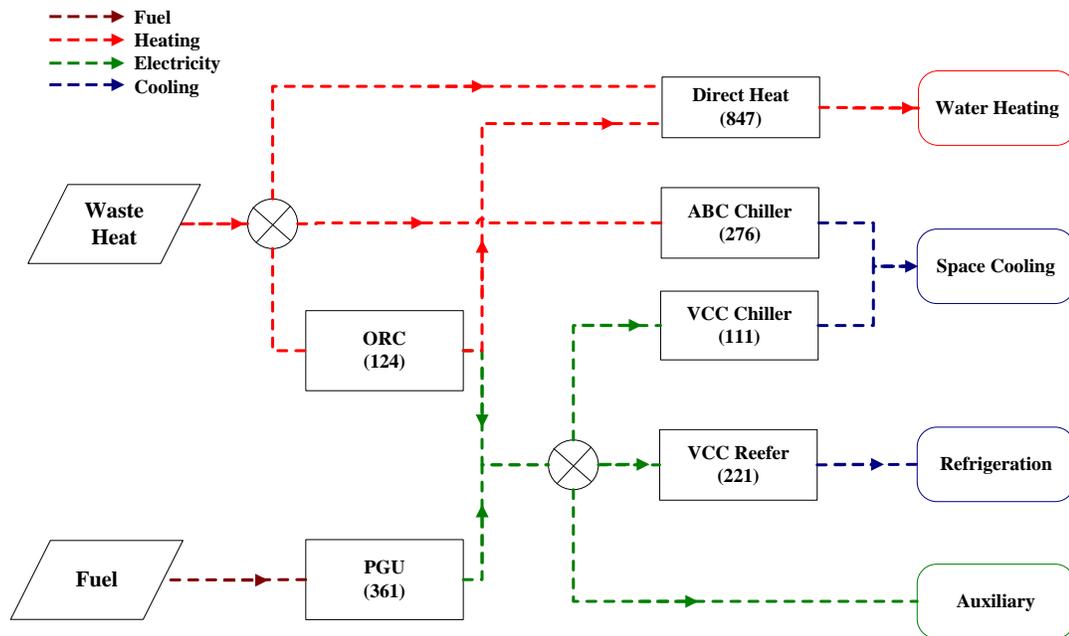
(a) Optimized system design under least robust scenario
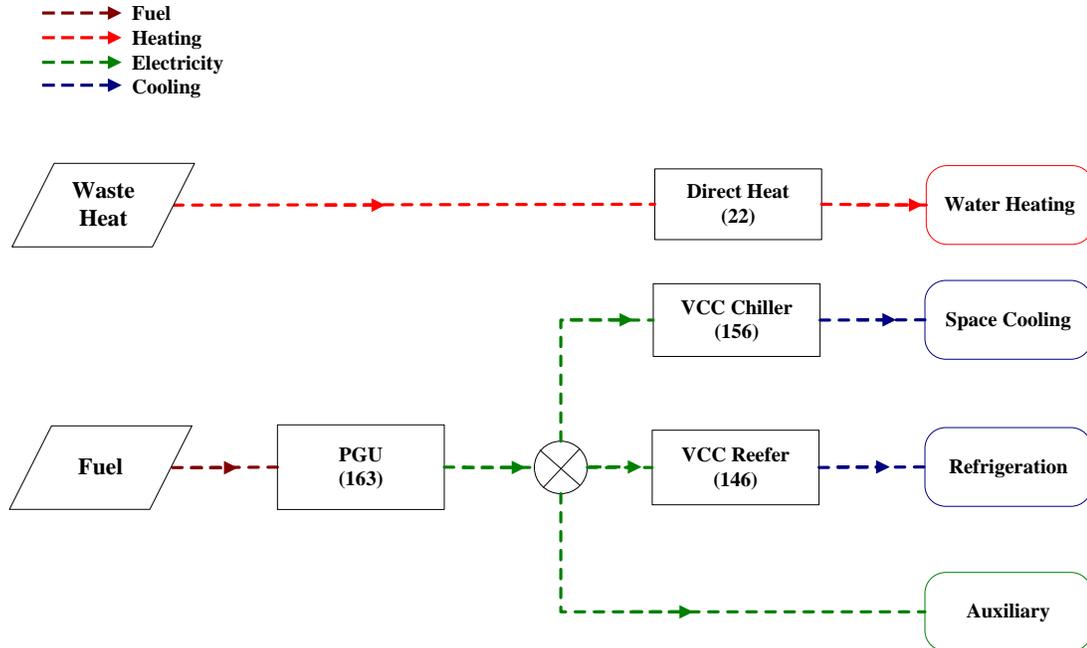
(b) Optimized system design under most robust scenario

Figure 5-14: Optimized system design under different scenarios

5.6 Summary

In this study, an advanced optimization framework was developed on MATLAB platform. The optimization based design framework fills current research gap on complete system level optimization from scratch, with comprehensive coverage on energy conversion equipment models and integrating options.

The design framework is able to find optimal system configurations and control strategies for any given load/weather profiles and equipment options from three different scenarios: minimizing life cycle cost as single-objective; minimizing capital cost and annual fuel energy consumption as bi-objective; minimizing life cycle cost considering uncertainties in load profiles. Comprehensive correlation based equipment models, including cascaded systems were set up for cooling, heating, refrigeration and power generations. The framework was applied to an oceanic container transportation application. Optimized system configuration and control strategy were found for onboard cooling, heating, refrigeration and auxiliary demands.

The optimized systems could reduce life cycle cost by 40% in single-objective optimization scenario, mostly contributed by utilizing waste heat from the main engine. Further analysis reveals that minimum available waste heat is the determent factor for optimized designs. Fuel "free" system designs are available during 25% of the sailing period. Pareto front solutions have been found to reflect trade-off relationships between capital cost reductions and fuel energy savings. Uncertainties has also been considered for load profiles. Robust optimization approach was used to address uncertainties. Optimized systems have been found at different levels of robustness.

6   Microgrid System Enhancements

Energy system designs are unique to specific applications. That being said, each system design can and should be tailored for specific application features. Such customizations can be fulfilled through local technology solutions, aiming to enhance system performance from various aspects. As the thesis focuses on ship applications, two features need to be addressed: high humidity conditions in sea route climates, limited fuel and waste heat availabilities. High humidity conditions brought by sea route weather conditions present high latent cooling loads for cooling system design. Consequently, space thermal comfort should also be evaluated carefully, particularly regarding indoor humidity levels. Limited fuel and waste heat availabilities impose necessities for system performance enhancement, particularly regarding system fuel consumptions.

To address this two features, two methods are considered: separate sensible and latent cooling (SSLC) system and pinch analysis. By applying the SSLC system to the current design, the design is expected to have better indoor thermal comfort performance. By applying pinch analysis to the current design, the design is expected to achieve higher fuel saving potential with better internal heat recovery methods. Following next, application of each method is explained in detail.

6.1   Separate Sensible and Latent Cooling System

Separate sensible and latent cooling system, implied by its name, is a cooling system taking care of sensible and latent cooling load with separate devices. Traditionally, cooling loads are met with a single equipment, such as a vapor compression air conditioning unit. To supply cooling air at a desirable temperature and humidity level, the

process air has to be cooled below its dew point, then reheated again. Therefore, the evaporator of the air-conditioning unit needs to operate at a rather low temperature (lower than the dew point of outdoor air). This leads to high pressure ratio of vapor compression air conditioning unit, hence electricity power consumption. Separate sensible and latent cooling system uses a desiccant wheel (refer to chapter 3.3) to dehumidify air at almost no electricity consumption. The sensible cooling loads are then met by dedicated air conditioning unit, such as a vapor compression unit. The vapor compression unit can now operate at higher evaporator temperature since it won't need to dehumidify air. Hence its power consumption can be reduced greatly. Meanwhile, as sensible and latent cooling loads are met by two independent units, supplied air can achieve desired conditions more easily than the standalone system.

There have been considerable studies on SSLC systems, with a focus on system performance enhancement through system design innovations. Study conducted by Ling et al. [166] serves as the basis for this study. In particular, following configuration was proposed and applied to previous waste heat powered system design (Figure 4-10), as shown in Figure 6-1. Outdoor air (state 1) flows through desiccant wheel and gets dehumidified. The dehumidification process through the desiccant wheel is isenthalpic ideally. Therefore, the air is heated up inevitably, leading to increasing sensible cooling loads. To remove the excess sensible cooling loads brought by desiccant wheel, an enthalpy wheel is used. The air now passes through enthalpy wheel and gets cooled. It then mixes with recirculated indoor air and finally flows through cooling coil, where the sensible cooling loads are fulfilled.
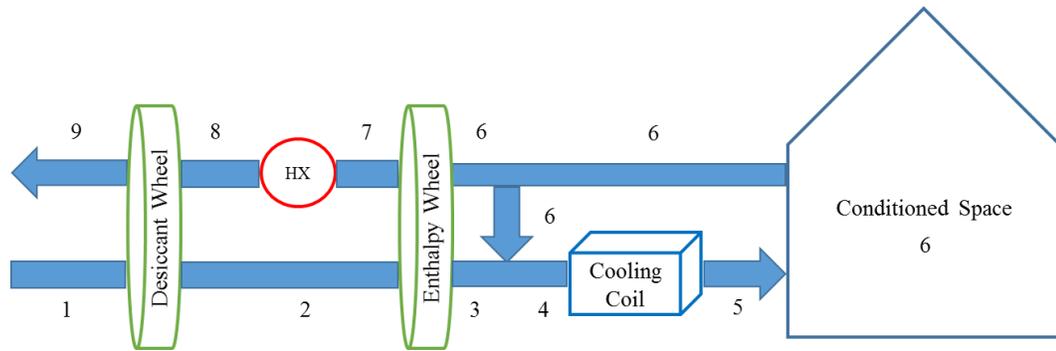
Figure 6-1: Configuration of separate sensible and latent cooling system

Configuration presented above can seamlessly integrated with design presented in Figure 4-10, as an add-on to existing space cooling system layout. The cooling coil can be integrated with existing absorption chiller. Hot water coming out of absorption cycle generator can serve as regeneration heating source for the desiccant wheel. The configuration was investigated from indoor thermal comfort and system fuel saving potential points of view.

First, steady state simulations were conducted on SSLC systems using EES. Following assumptions were used:

- Outdoor condition $T_1 = 27°C$, $RH_1 = 80.2\%$

- Room condition $T_6 = 25°C$, $RH_6 = 50\%$

- Desiccant wheel COP = 0.5

- Enthalpy wheel effectiveness $\varepsilon = 0.75$

- Isenthalpic process through desiccant wheel

- Recirculation air ratio 0.8

- The VCC removes sensible load only

- Regeneration air $T_8 = 60°C$

Figure 6-2 shows overall system process on a psychrometric chart. The state points are corresponding to those on Figure 6-1. As can be seen, the desiccant wheel takes care of removing moisture from outdoor air while enthalpy wheel and cooling coil lowers air temperature. The regeneration heating source for the desiccant wheel is 60°C, which can be realized using hot water coming out of absorption cycle generator. According to steady state simulation results, the desiccant wheel needs to have a moisture removal capacity of 5.1 $g \cdot s^{-1}$. Therefore, 150 mm DW is selected for the design (refer to Table 3-11).
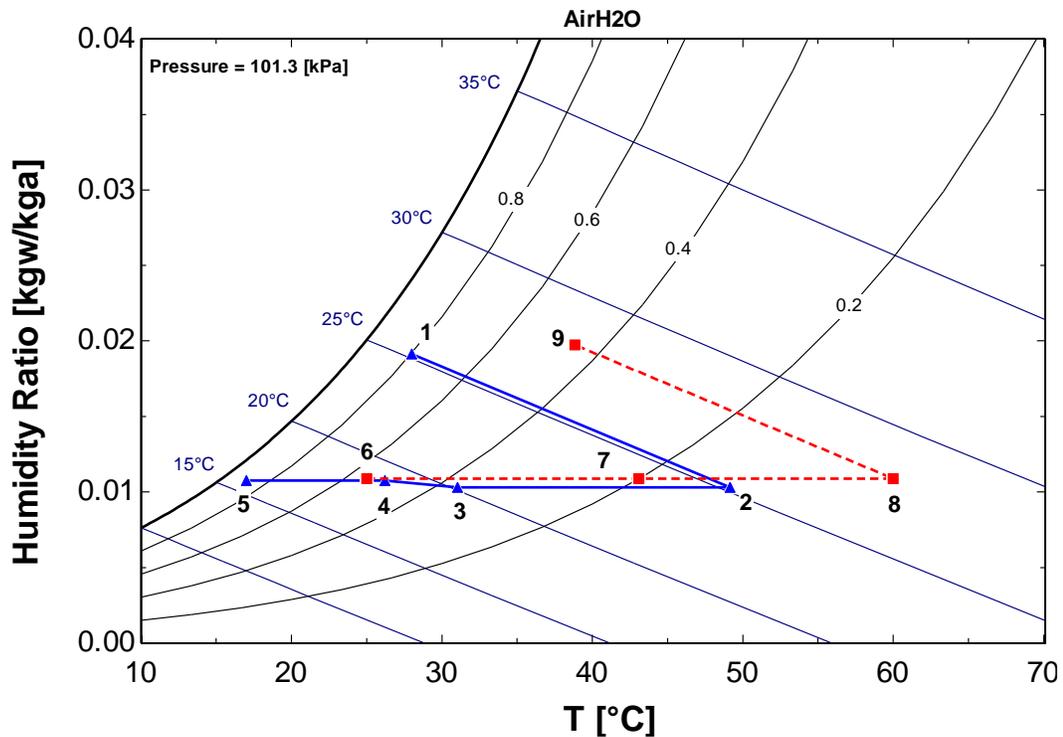
Figure 6-2: SSLC system process on the psychrometric chart

The SSLC system is then integrated to previous waste heat powered system on the TRNSYS platform for transient modeling study. Performance map based model was developed for the desiccant wheel, using results from previous experimental testing (refer to chapter 3.3). Standard type 667d from TRNSYS was used for enthalpy wheel. The

integrated system was simulated for the entire sailing route (from Pusan, Korea to Karachi, Pakistan).

Figure 6-3 shows cooling loads breakdown for the entire sailing period. As can be seen, all latent cooling load comes from outdoor air. The desiccant wheel removes a large portion of latent load (63%), followed by air conditioning unit (35%) and enthalpy wheel (2%). Note under transient simulations, desiccant wheel does not remove 100% of latent loads as design results indicated by steady state simulations. This is expected as the system may operate under off-design conditions considering fluctuations of outdoor humidity levels, regeneration heat source temperatures and indoor conditions. The sensible load comes from outdoor air (62%) and desiccant wheel heating (38%). The enthalpy wheel removes 25% of total sensible cooling loads. The air conditioning unit removes the rest.
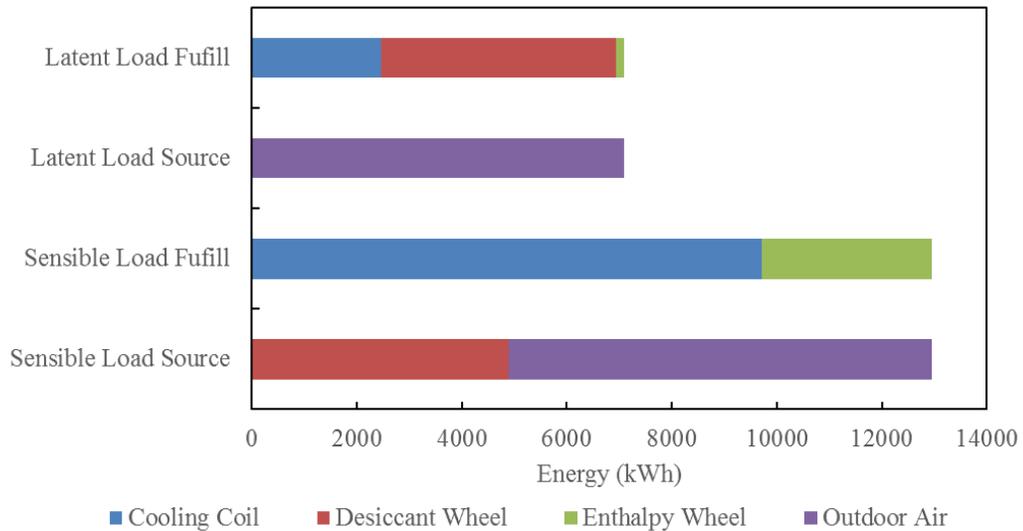
Figure 6-3: Cooling load breakdown in SSLC system

Figure 6-4 compares system indoor thermal comfort performance on a psychrometric chart. The gray clouds represent outdoor conditions. The orange clouds

represent indoor space conditions without SSLC system while the blue clouds are corresponding to indoor conditions with SSLC system. It is observed better indoor conditions can be achieved with SSLC system, particularly regarding humidity levels.
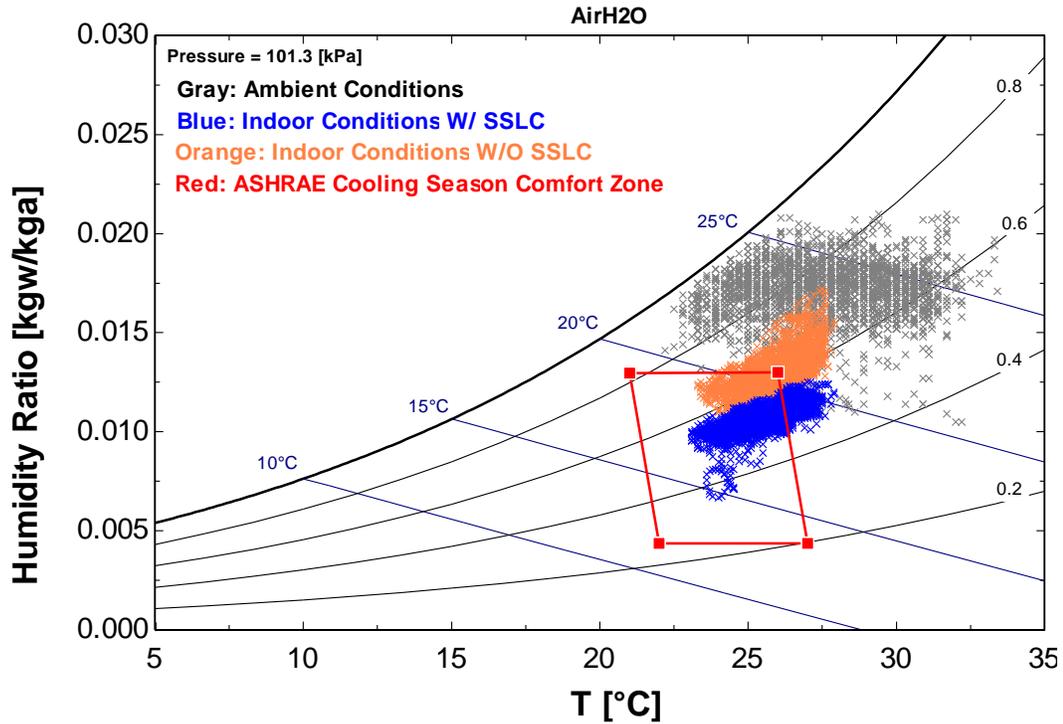
Figure 6-4: Indoor thermal comfort comparison w and w/o SSLC system

Table 6-1 summarizes performance improvements by integrating SSLC system to current waste heat powered system design. As indicated before, SSLC system would allow air conditioning unit evaporator operating at higher temperature. Thus power consumption of compression air conditioning unit would reduce due to reduced pressure ratio. However it is not the case in this study as an absorption chiller is used. Hence higher evaporator temperature won't reduce electricity power consumption greatly, though the solution pump power consumption is reduced. Meanwhile, the desiccant wheel and enthalpy wheel increase pressure drop in the air duct, thus fan power consumption. As a result, introducing

the SSLC system only increase system performance by around 11% and reduce fuel consumption further by 2.7%. In summary, introducing SSLC system to current design brings significant indoor thermal comfort benefits while limited fuel saving benefits.

Table 6-1: System performance improvements with SSLC system

Index	WHP	WHP and SSLC
$COP_{system-electricity}$	2.00	2.21 (+10.5 %)
Primary Energy Ratio	0.80	0.89 (+11.3 %)
Total Fuel Consumption (ton)	17.24	16.78 (-2.7 %)
Total CO_2 emission (ton CO_{2eq})	156.93	152.67 (-2.7 %)

6.2 Pinch Analysis

Pinch analysis is a methodology for minimizing energy consumption of energy processes by calculating thermodynamically feasible energy targets (or minimum energy consumption) and achieving them by optimizing heat recovery systems, energy supply methods and process operating conditions. Kemp [167] presents a comprehensive review on pinch analysis methodology. Pinch analysis has been widely used in energy system analysis, particularly those systems involving heat processes.

The waste heat powered system presented before (refer to Figure 4-10) was used for pinch analysis. The system involves many heat processes at various temperature levels. The first step in pinch analysis is to define all process streams. Table 6-2 presents a list of process streams extracted from the waste heat powered system. Each stream is listed with fluid, supply and target temperature, heat duty and stream type.

Table 6-2: Process streams for pinch analysis

Stream No.	Stream Name	Stream Fluid	Supply Temperature °C	Target Temperature °C	Heat Duty kW	Stream Type
1	Absorption Generator	LiBr-H_2O	63	83	438	Cold
2	Absorption Condenser	H_2O	77	40	314	Hot
3	Absorption Evaporator	H_2O	3	5	260	Cold
4	Absorption Absorber	LiBr-H_2O	45	33	384	Hot
5	VCC Reefer Evaporator	R-404A	-30	-25	141	Cold
6	VCC Reefer Condenser	R-404A	90	40	215	Hot
7	Cooling Coil	Air	25	15	46	Hot
8	Heating Coil	Air	15	25	46	Cold
9	Desiccant Wheel	Air	25	60	37	Cold

The composite curve was then generated based on process stream data, with pinch point temperature difference defined as 10 K. Figure 6-5 presents composite curve analysis. The composite curve presents hot and cold process streams in two different lines, with temperature variations versus heat duties. Hot and cold pinch temperatures are 73°C and 63°C, respectively. Based on the composite curve analysis, the minimal hot and cold utilities are 331 and 367 kW. The region in between represents the maximum heat recovery could be achieved.
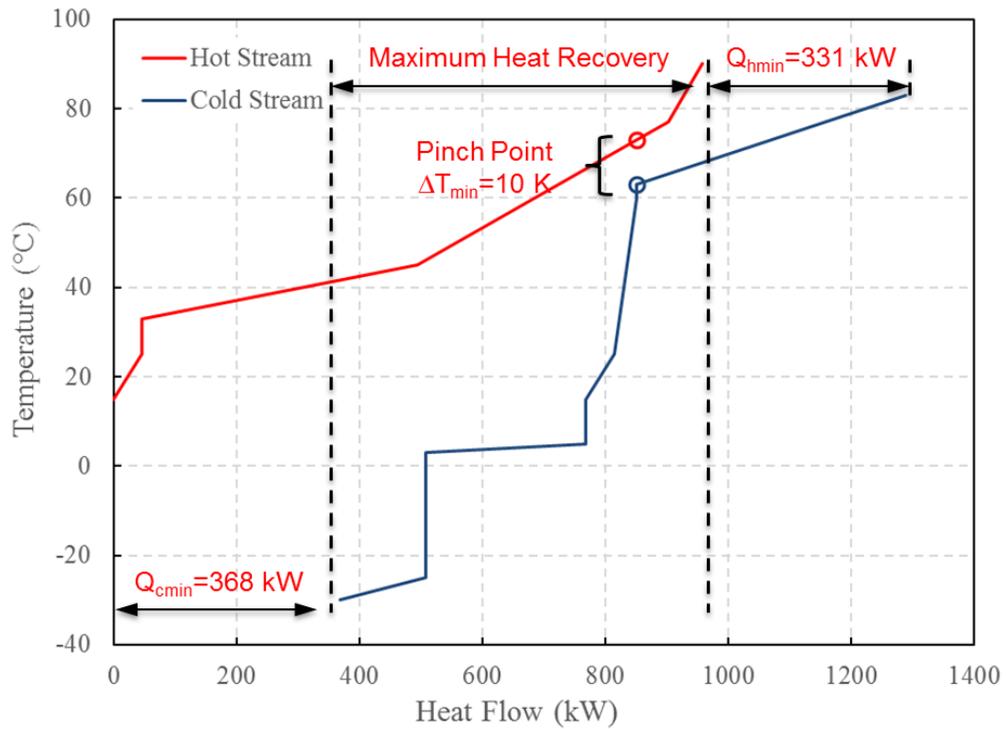
Figure 6-5: Composite curve analysis

To further identify heat recovery methods in detail, the grand composite curve was used. Figure 6-6 presents grand composite curve analysis. The grand composite curve combines hot and cold stream curves into one curve, composed with different segments. For each segment, it either needs heating supply (if goes upward along x axis direction) or cooling supply (if goes downward along x axis direction).
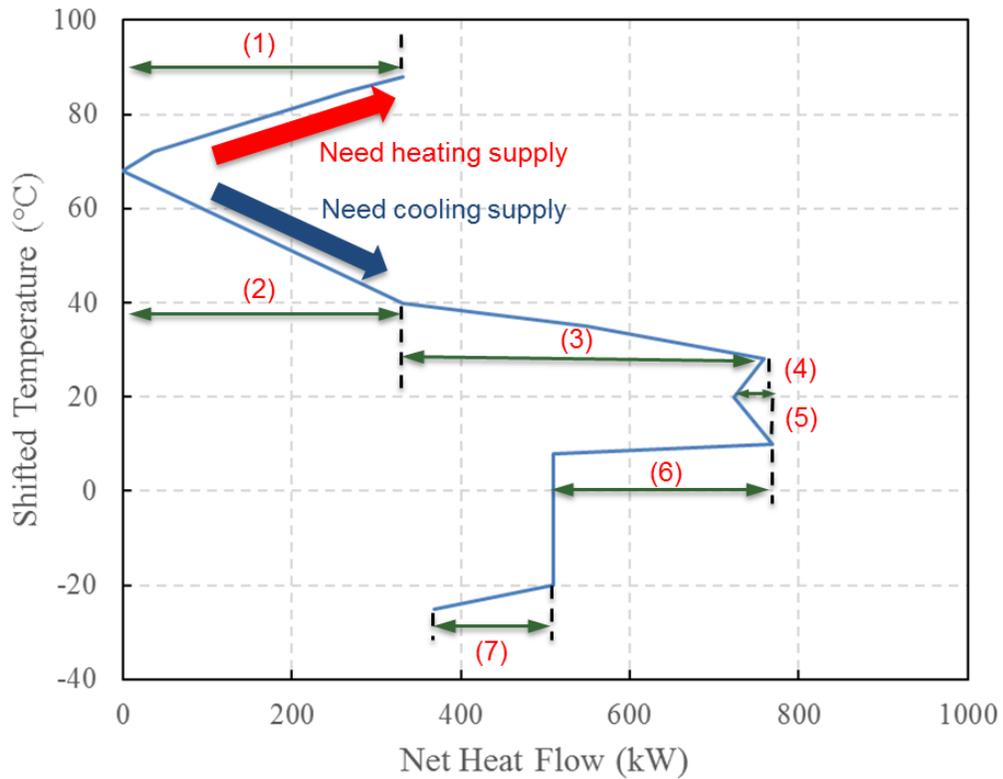
Figure 6-6: Grand composite curve analysis

Based on grand composite curve, heating and cooling supplies for all segments are defined, as shown in Table 6-3. For each segment, heat duty sources, fulfill methods and whether methods belong to internal heat recovery are listed. For fulfill methods, it means heating supplies with a plus mark and cooling supplies with a minus mark.

Table 6-3: Heating and cooling supplies based on grand composite curve analysis

No.	Generation	Fulfill	Internal Heat Recovery
1	Abs. generator	Exhaust gas (+)	No
2	Abs. condenser; VCC condenser	Heating coil (-); Abs. evaporator (-)	Yes; Yes
3	Abs. absorber	Heating coil (-)	Yes
4	Desiccant wheel; Heating coil	VCC condenser (+); Abs. condenser (+)	Yes; Yes
5	Cooling coil	Abs. evaporator (-)	Yes
6	Abs. evaporator	VCC condenser (+); Cooling coil (+)	Yes
7	VCC evaporator	External air (+)	No

Based on Table 6-3, all segments can be fulfilled with proper internal heat recovery methods except for absorption cycle generator and VCC evaporator. For the absorption cycle generator, external heating supplies are needed as no higher temperature internal stream existing. For VCC evaporator, it has to be cooled by external air due to closed air loop feature in refrigeration units. Regarding internal heat recovery, it can be accomplished mainly in two ways: a cascaded absorption-compression refrigeration system layout, utilizing rejected heat from absorption cycle and vapor compression cycle for other heating purposes. Note cascaded heat usage is the key to avoid inefficient heat recovery. For instance, high temperature heat from absorption cycle condensers and vapor compression cycle condensers should be prioritized for high temperature heating demands, such as desiccant wheel regeneration. Low temperature heat from absorption cycle absorbers should be used for low temperature heating demands, such as heating coils.

Note some of the internal heat recovery methods have been applied to the waste heat powered system, such as cascaded absorption-compression refrigeration system layout. Calculations were conducted to investigate energy saving potentials by applying all heat recovery methods. It is found 6% more fuel saving could be achieved beyond current waste heat powered system design, at 10K pinch point temperature difference. Applying waste heat recovery methods reduces usage of electric heater and boilers, however it increases pump and fan power due to more pipe and duct connections. One should also keep in mind that pinch analysis mainly aims to reduce hot and cold utilities. In this study, applying all heat recovery methods would greatly reduce system dependence on external waste heat and cooling source, therefore boosting system robustness.

6.3 Design Guideline

When designing an energy system for a ship application, there are lots of uncertainties need to be considered: route recourse, extreme weather and unexpected loading/unloading requirements, to name a few. A good design should be not only energy efficient and cost effective, but also reliable, particularly under unexpected scenarios. Previous studies paved approaches to energy efficient and cost effective designs based on dynamic modeling and optimization techniques. This chapter sheds some light on guidelines toward reliable designs.

The first step is to understand how different scenarios affects system designs. Usually all scenarios affect designs in two ways: changes in load profiles and changes in weather profiles (consequently equipment performances). For instance, route recourse leads to different sea route climates. As such, cooling and heating demands are different.

The weather conditions are also changing, so does equipment performance. Note the main engine performance is relatively stable, therefore the available waste heat supply is also stable.

The next step is to decide appropriate approaches to deal with such changes. Load profile changes can be dealt with equipment oversizing. Usually safety factors (larger than 1) are applied to nominal capacities. However, equipment cost also increases. To avoid necessary oversizing of all equipment, advanced system designs such as separate sensible and latent cooling system is preferred. For example, oversizing of desiccant wheels only can successfully address unexpected high humidity climates while not incur large capital investment increase.

Weather profile changes can affect equipment performance, though levels may differ for each equipment. Sensitivity analysis is necessary to reveal which equipment will be impacted most. Usually sea water cooled equipment is less impacted compared to air cooled equipment, as sea water temperature fluctuations are smaller.

6.4   Summary

In this study, two methods have been investigated to enhance microgrid system performance. The first method is applying separate sensible and latent cooling system to current waste heat powered system design. The separate sensible and latent cooling system fulfills sensible and latent cooling loads with two devices: air conditioning unit and desiccant wheel. Steady and transient simulations were conducted. Based on simulation results, applying separate sensible and latent cooling system would increase the system fuel saving potential further by 2.7%. It increases system indoor comfort level greatly.

Pinch analysis was applied to the waste heat powered system. Process streams were identified and used to generate composite and grand composite curves. Minimum hot and cold utilities were identified. Heat recovery methods were found for heat duties at different temperature levels. Applying all possible heat recovery methods would increase system fuel saving potential further by 6%. It also reduces system's dependence on external waste heat and cooling source.

7 List of Major Contributions and Future Work

7.1 Major Contributions

The major contributions of this research are the development of a generalized microgrid system analysis framework based on dynamic modeling of novel system configurations and advanced optimization based design framework. These contributions are summarized below:

1. Microgrid system component modeling and study with following contributions:

   a. A comprehensive and detailed ship model including engine, thermal zones and sea route weather sets the basis for dynamic system modeling and fills current research gap in ship applications.

   b. Novel component models expanding current microgrid system study domain by focusing on ship application design features: new material desiccant wheel study under high humidity climates, low temperature refrigerated container model and sea water cooled absorption cycle model with operation constraints.

2. Dynamic microgrid system modeling with following contributions:

   a. Dynamic modeling of a novel microgrid system design which is for the first time designed for container ships regarding cooling, heating and refrigeration demands.

   b. Comprehensive performance, payload, economic analysis and validations provide an advanced microgrid energy system analysis framework.

3. Microgrid system optimization with following contribution:

173

a. An advanced optimization based design framework holds the capability for equipment integrations for the first time, and a most comprehensive equipment coverage regarding cooling, heating, refrigeration and power generation cycles to date.

b. The framework is able to conduct both configuration and control strategy optimization for any applications. Therefore it extends current control strategy focused optimization studies to complete system optimization from scratch.

c. Thorough case studies through three different scenarios provide in-depth demonstrations of optimization framework for the first time.

4. Microgrid system enhancement study with following contribution:

a. Investigations on enhancement options deepen understanding of benefits and feasibilities of integrating these options into current microgrid system designs and allow more advanced designs.

7.2 List of Publications

The following peer-reviewed journal papers were published or submitted as outcomes of the research conducted in this dissertation.

- **T. Cao**, Y. Hwang, R. Radermacher, H. Chun. "Development of an Optimization Framework for Microgrid Energy Systems", Submitted to Energy.

- **T. Cao**, H. Lee, Y. Hwang, R. Radermacher, H. Chun. "Modeling of Waste Heat Powered Energy System for Container Ships", Energy, 2016, 106: 408-421.

- **T. Cao**, H. Lee, Y. Hwang, R. Radermacher, H. Chun. "Performance Investigation of Engine Waste Heat Powered Absorption Cycle Cooling System for Shipboard Applications", Applied Thermal Engineering, 2015, 90: 820-830.

- **T. Cao**, H. Lee, Y. Hwang, R. Radermacher, H. Chun. "Experimental investigation of thin polymer desiccant wheel performance", International Journal of Refrigeration, 2014, 44: 1-11.

The following peer-reviewed conference papers were published or accepted and resulted from this research conducted in this dissertation.

- **T. Cao**, Y. Hwang, R. Radermacher, H. Chun. "Development of an optimization framework for microgrid energy conversion systems", Proceedings of ASME 2016 International Mechanical Engineering Congress & Exposition. Phoenix, Arizona, 2016.

- **T. Cao**, J. Ling, Y. Hwang, R. Radermacher. "Development of a novel two-stage heat pump clothes dryer", Proceedings of ASME 2014 International Mechanical Engineering Congress & Exposition. Montreal, Canada, 2014.

- **T. Cao**, H. Lee, Y. Hwang, R. Radermacher. "Modeling of hybrid cooling systems for shipboard application", Proceedings of the ASME 2014 8th International Conference on Energy Sustainability & 12th Fuel Cell Science. Boston, Massachusetts, 2014.

- H. Lee, **T. Cao**, Y. Hwang, R. Radermacher. "Experimental investigations of a desiccant wheel cycle", 4th IIR Conference on Thermophysical Properties and Transfer Processes of Refrigerants. Delft, Netherlands, 2013.

7.3 Future Work

The research work presented in this thesis represents cutting edge modeling and optimization of microgrid energy systems. Following research tasks could further enrich microgrid energy system analysis framework:

- Introduce advanced cycle models into current microgrid system modeling framework, such as Kalina cycle, thermoelectric devices and adsorption cycles. This will enrich model versatilities to different system designs.

- Introduce more cycle models to current optimization based design framework, with a focus on cycles for other energy generations and on-grid applications. This will enable the design framework to be used for various microgrid applications.

- Perform detailed simulations on optimized system designs. This will set up connections between modeling and optimization framework, as well as enhance confidence on optimization results.

- Investigate methods to boost system reliability. In particular consider following aspects: impact of sea route recourse on optimal system designs; consider hedging effects in optimization under uncertainty.

8 Bibliography

[1] J. Vidal, "Shipping boom fuels rising tide of global CO2 emissions," The Guardian, United Kingdom, 2008 (13th February).

[2] "International Convention for the Prevention of Pollution from Ships (MARPOL)," International Maritime Organization, 2008. [Online]. Available: http://www.imo.org/About/Conventions/ListOfConventions/Pages/International-Convention-for-the-Prevention-of-Pollution-from-Ships-%28MARPOL%29.aspx. [Accessed 8 October 2014].

[3] "Second IMO GHG Study 2009, Update of the 2000 IMO GHG Study, Final report covering Phase 1 and Phase 2, IMO MEPC 59/INF.10," International Maritime, 2009.

[4] G. Shu, Y. Liang, H. Wei, H. Tian, J. Zhao and L. Liu, "A review of waste heat recovery on two-stroke IC engine aboard ships," *Renewable and Sustainable Energy Reviews,* vol. 19, pp. 385-401, 2013.

[5] P. S, H. J, Y. BS and P. SH, "Computational analysis of ship's exhaust-gas flow and its application for antenna location," *Applied Thermal Engineering,* vol. 31, pp. 1689-1702, 2011.

[6] M. B. D. LTD, "Thermo Efficiency System (TES)for reduction of fuel consumption and CO2 emission," MAN B&W Diesel A/S, Copenhagen, Denmark, July 2005.

[7] A. B. Little and S. Garimella, "Comparative assessment of alternative cycles for waste heat recovery and upgrade," *Energy,* vol. 36, pp. 4492-4504, 2011.

[8] J. Fernandez-Seara, A. Vales and M. Vazquez, "Heat recovery system to power an onboard NH3-H2O absorption refrigeration plant in trawler chiller fishing vessels," *Applied Thermal Engineering,* vol. 18, pp. 1189-1205, 1998.

[9] L. Wang, R. Wang, J. Wu, K. Wang and S. Wang, "Adsorption ice makers for fishing boats driven by the exhaust heat from diesel engine: choice of adsorption pair," *Energy Conversion and Management,* vol. 45, pp. 2043-2057, 2004.

[10] S. Garimella, A. M. Brown and A. K. Nagavarapu., "Waste heat driven absorption/vapor-compression cascade refrigeration system for megawatt scale, high-flux, low-temperature cooling," *International Journal of Refrigeration,* vol. 34, pp. 1776-1785, 2011.

[11] Y. Liang, G. Shu, H. Tian, X. Liang, H. Wei and L. Liu, "Analysis of an electricity–cooling cogeneration system based on RC–ARS combined cycle aboard ship," *Energy Conversion and Management,* vol. 76, pp. 1053-1060, 2013.

[12] Y. E.-G. Ahmed Ouadha, "Integration of an ammonia-water absorption refrigeration system with a marine Diesel engine: A thermodynamic study," *Procedia Computer Science,* vol. 19, pp. 754-761, 2013.

[13] J. Khan, W. Lear, S. Sherif, E. Howell, J. Crittenden and P. Meitner, "A novel pressurized CHP system with water extraction and refrigeration," *Applied Thermal Engineering,* vol. 30, no. 10, pp. 1081-1090, 2010.

[14] A. Mortazavi, C. Somers, A. Alabdulkarem, Y. Hwang and R. Radermacher, "Enhancement of APCI cycle efficiency with absorption chillers," *Energy,* vol. 35, no. 9, pp. 3877-3882, 2010.

[15] L. K. C. Tse, S. Wilkins, N. McGlashan, B. Urban and R. Martinez-Bota, "Solid oxide fuel cell/gas turbine trigeneration system for marine applications," *Journal of Power Sources,* vol. 196, no. 6, pp. 3149-3162, 2010.

[16] F. Ghirardo, M. Santin, A. Traverso and A. Massardo, "Heat recovery options for onboard fuel cell systems," *International Journal of Hydrogen Energy,* vol. 36, no. 13, pp. 8134-8142, 2011.

[17] A. Arsalis, "Modeling and simulation of a 100 kWe HT-PEMFC subsystem integrated with an absorption chiller subsystem," *International Journal of Hydrogen Energy,* vol. 37, no. 18, pp. 13484-13490, 2012.

[18] Z. Seyfouri and M. Ameri, "Analysis of integrated compression–absorption refrigeration systems powered by a microturbine," *International Journal of Refrigeration,* vol. 35, no. 6, pp. 1639-1646, 2012.

[19] K. Gommed and G. Grossman, "Investigation of an improved solar-powered open absorption system for cooling, dehumidification and air conditioning," *International Journal of Refrigeration,* vol. 35, no. 3, pp. 676-684, 2012.

[20] F. Calisea, G. Ferruzzia and L. Vanoli, "Transient simulation of polygeneration systems based on PEM fuel cells and solar heating and cooling technologies," *Energy,* vol. 41, no. 1, pp. 18-30, 2012.

[21] S. H. Mohammadi and M. Ameri, "Energy and exergy comparison of a cascade air conditioning system using different cooling strategies," *International Journal of Refrigeration,* vol. 41, pp. 14-26, 2014.

[22] S. Garimella, A. M. Brown and A. K. Nagavarapu, "Waste heat driven absorption/vapor-compression cascade refrigeration system for megawatt scale,

high-flux,low-temperature cooling," *International Journal of Refrigeration,* vol. 34, pp. 1776-1785, 2011.

[23] Z. Seyfouri and M. Ameri, "Analysis of integrated compressioneabsorption refrigeration systems powered by a microturbine," *International Journal of Refrigeration,* vol. 34, pp. 1639-1646, 2012.

[24] S. H. Mohammadi and M. Ameri, "Energy and exergy comparison of a cascade air conditioning system using different cooling strategies," *International Journal of Refrigeration,* vol. 41, pp. 14-26, 2014.

[25] V. Jain, S. Kachhwaha and G. Sachdeva, "Thermodynamic performance analysis of a vapor compression–absorption cascaded refrigeration system," *Energy Conversion and Management,* vol. 75, pp. 685-700, 2013.

[26] C. Horvath, Y. Hwang, R. Radermacher, W. Gerstler and C.-J. Tang, "Waste heat and electrically driven hybrid cooling systems for a high ambient temperature, off-grid application," *Energy,* vol. 66, pp. 711-721, 2014.

[27] Z. Sun, "Experimental investigation of integrated refrigeration system (IRS) with gas engine, compression chiller and absorption chiller," *Energy,* vol. 33, pp. 431-436, 2008.

[28] C. Cimsit and I. T. Ozturk, "Analysis of compressioneabsorption cascade refrigeration cycles," *Applied Thermal Engineering,* vol. 40, pp. 311-317, 2012.

[29] L. Kairouani and E. Nehdi, "Cooling performance and energy saving of a compression–absorption refrigeration system assisted by geothermal energy," *Applied Thermal Engineering,* vol. 26, pp. 288-294, 2006.

[30] J. Ferna´ndez-Seara, J. Sieres and M. Va´zquez, "Compression–absorption cascade refrigeration system," *Applied Thermal Engineering,* vol. 26, pp. 502-512, 2006.

[31] L. Wang, A. Ma, Y. Tan, X. Cui and H. Cui, "2012 International Conference on Future Energy, Environment, and Materials," *Energy Procedia,* vol. 16, pp. 1503-1509, 2012.

[32] V. C. Aute, "Single and Multiresponse Adaptive Design of Experiments with Application to Design Optimization of Novel Heat Exchangers," University of Maryland, College Park, 2009.

[33] D. A. Manolas, C. A. Frangopoulos, T. P. Gialamas and D. T. Tsahalis, "Operation optimization of an industrial cogeneration system by a genetic algorithm," *Energy Conversion Management,* vol. 38, pp. 15-17, 1997.

[34] J. Wang, Z. Zhai, Y. Jing and C. Zhang, "Particle swarm optimization for redundant building cooling heating and power system," *Applied Energy,* vol. 87, pp. 3668-3679, 2010.

[35] M. Liu, Y. Shi and F. Fang, "A new operation strategy for CCHP systems with hybrid chillers," *Applied Energy,* vol. 95, pp. 164-173, 2012.

[36] D. Buoro, P. Pinamonti and M. Reini, "Optimization of a Distributed Cogeneration System with solar district heating," *Applied Energy,* vol. 124, pp. 298-308, 2014.

[37] H. Sayyaadi, "Multi-objective approach in thermoenvironomic optimization of a benchmark cogeneration system," *Applied Energy,* vol. 86, pp. 867-879, 2009.

[38] A. Ghobeity, C. J. Noone, C. N. Papanicolas and A. Mitsos, "Optimal time-invariant operation of a power and water cogeneration solar-thermal plant," *Solar Energy,* vol. 85, pp. 2295-2320, 2011.

[39] A. Rong and R. Lahdelma, "An efficient linear programming model and optimization algorithm for trigeneration," *Applied Energy,* vol. 82, pp. 40-63, 2005.

[40] I. J. Esfahani and C. Yoo, "Exergy analysis and parametric optimization of three power and fresh water cogeneration systems using refrigeration chillers," *Energy,* vol. 59, pp. 340-355, 2013.

[41] W. Lianying, H. Yangdong and G. Congjie, "Optimum design of cogeneration for power and desalination to satisfy the demand of water and power," *Desalination,* vol. 324, pp. 111-117, 2013.

[42] D. A. MANOLAS, C. A. FRANGOPOULOS, T. P. GIALAMAS and D. T. TSAHALIS, "OPERATION OPTIMIZATION OF AN INDUSTRIAL COGENERATION SYSTEM BY A GENETIC ALGORITHM," *Energy Conversion Management,* vol. 38, pp. 15-17, 1997.

[43] M. Rodrı´guez-Toral, W. Morton and D. Mitchell, "Using new packages for modelling, equation oriented simulation and optimization of a cogeneration plant," *Computers and Chemical Engineering,* vol. 24, pp. 2667-2685, 2000.

[44] P. Mago and L. Chamra, "Analysis and optimization of CCHP systems based on energy, economical, and environmental considerations," *Energy and Buildings,* vol. 41, pp. 1099-1106, 2009.

[45] B. Wille-Haussmann, T. Erge and C. Wittwer, "Decentralised optimisation of cogeneration in virtual power plants," *Solar Energy,* vol. 84, pp. 604-611, 2010.

[46] J.-J. Wang, Y.-Y. Jing and C.-F. Zhang, "Optimization of capacity and operation for CCHP system by genetic algorithm," *Applied Energy,* vol. 87, pp. 1325-1335, 2010.

[47] J. Wang, Z. (. Zhai, Y. Jing and C. Zhang, "Particle swarm optimization for redundant building cooling heating and power system," *Applied Energy,* vol. 87, pp. 3668-3679, 2010.

[48] H. Sayyaadi, M. Babaie and M. R. Farmani, "Implementing of the multi-objective particle swarm optimizer and fuzzy decision-maker in exergetic, exergoeconomic and environmental optimization of a benchmark cogeneration system," *Energy,* vol. 36, pp. 4777-4789, 2011.

[49] J. Ortiga, J. Bruno and A. Coronas, "Selection of typical days for the characterisation of energy demand in cogeneration and trigeneration optimisation models for buildings," *Energy Conversion and Management,* vol. 52, pp. 1934-1942, 2011.

[50] J. Wang, Z. (. Zhai, Y. Jing, X. Zhang and C. Zhang, "Sensitivity analysis of optimal model on building cooling heating and power system," *Applied Energy,* vol. 88, pp. 5134-5152, 2011.

[51] J.-y. Wu, J.-l. Wang and S. Li, "Multi-objective optimal operation strategy study of micro-CCHP system," *Energy,* vol. 48, pp. 472-483, 2012.

[52] V. Zare, S. Mahmoudi, M. Yari and M. Amidpour, "Thermoeconomic analysis and optimization of an ammoniaewater power/cooling cogeneration cycle," *Energy,* vol. 47, pp. 271-283, 2012.

[53] M. Liu, Y. Shi and F. Fang, "Optimal power flow and PGU capacity of CCHP systems using a matrix modeling approach," *Applied Energy,* vol. 102, pp. 794-802, 2013.

[54] T. Wakui, T. Kinoshita and R. Yokoyama, "A mixed-integer linear programming approach for cogeneration based residential energy supply networks with power and heat interchanges," *Energy,* vol. 68, pp. 29-46, 2014.

[55] R. Soltani, P. M. Keleshtery, M. Vahdati, M. KhoshgoftarManesh, M. Rosen and M. Amidpour, "Multi-objective optimization of a solar-hybrid cogeneration cycle: Application to CGAM problem," *Energy Conversion and Management,* vol. 81, pp. 60-71, 2014.

[56] T. Wakui and R. Yokoyama, "Optimal structural design of residential cogeneration systems in consideration of their operating restrictions," *Energy,* vol. 64, pp. 719-733, 2014.

[57] R. Karaali and I. T. Oztürk, "Thermoeconomic optimization of gas turbine cogeneration plants," *Energy,* vol. 80, pp. 474-485, 2015.

[58] K. Herold, R. Radermacher and S. Klein, Absorption Chillers and Heat Pumps, Boca Raton, FL: CRC Press, 1996.

[59] Intel, *Intel® Parallel Studio XE 2015 Composer Edition for Fortran Windows,* 2014.

[60] ASHRAE, 2009 ASHRAE Handbook, Atlanta, GA: American Society of Heating, Refrigerating and Air-Conditioning Engineers, 2009.

[61] J. Patek and J. Klomfar, "A computationally effective formulation of the thermodynamic properties of LiBr-H2O from 273 to 500K over full composition range," *International Journal of Refrigeration,* vol. 29, pp. 566-578, 2006.

[62] ASHRAE, Handbook fo Fundamentals, Atlanta, GA: ASHRAE, 1997.

[63] S. e. a. Klein, "TRNSYS 17: A Transient System Simulation Program," Solar Energy Laboratory, University of Wisconsin, Madison, USA, 2010.

[64] G. SketchUp, *SketchUp 2014 - Maintenance Release 1, Version 14.1.1282,* 2014.

[65] T. E. GmbH, *TRNSYS 17, Volme 5 Multizone Building modeling with Type 56 and TRNBuild,* Madison, WI: Solar Energy Laboratory, University of Wisconsin-Madison, 2012.

[66] I. 7730, "Ergonomics of the thermal environment -- Analytical determination and interpretation of thermal comfort using calculation of the PMV and PPD indices and local thermal comfort criteria," International Organization for Standardization, 2009.

[67] N. U. C. f. A. R. E. S. R. L. National Climatic Data Center, "International Comprehensive Ocean-Atmosphere Data Set (ICOADS) Release 2.5, Individual Observations.," [Online]. [Accessed 14 July 2015].

[68] C. Jia, Y. Dai and J. Wu, "Experimental Comparison of two honeycombed desiccant wheels fabricated with silica gel and composite desiccant material," *Energy Conversino and Management,* vol. 47, pp. 2523-2534, 2006.

[69] M. G. R. R. T. S. A. G. D.-Y. L. Stephen D. White, "Characterization of desiccant wheels with alternative materials at low regeneration temperatures," *International Journal of Refrigeration,* vol. 34, pp. 1786-1791, 2011.

[70] D.-Y. L. Joohyun Lee, "Sorption characteristics of a novel polymeric desiccant," *International Journal of a novel polymeric desiccant,* vol. 35, pp. 1940-1949, 2012.

[71] K. G. Y. H. R. R. H.-H. C. Suxin Qian, "Cyclic steady performance of adsorption chiller with low regeneration temperature zeolite," *Energy,* vol. 60, pp. 517-526, 2013.

[72] M. Ahmed, K. N.M. and F. M, "Evaluation and optimization of solar desiccant wheel performance," *Renewable Energy,* vol. 30, pp. 305-325, 2005.

[73] N. Enteria, H. Yoshino, A. Satake, A. Mochida, R. Takaki, R. Yoshie, T. Mitamura and S. Baba, "Experimental heat and mass transfer of the seperated and coupled rotating desiccant wheel and heat wheel," *Experimental Thermal and Fluid Science,* vol. 34, pp. 603-615, 2010.

[74] U. Eicker, U. Schurger, M. Kohler, T. Ge, Y. Dai, H. Li and R. Wang, "Experimental investigations on desiccant wheels," *Applied Thermal Engineering,* vol. 42, pp. 71-80, 2012.

[75] A. G, F. Minichiello, C. Roselli and M. Sasso, "Experimental analysis on the dehumidification and thermal performance of a desiccant wheel," *Applied Energy,* vol. 92, pp. 563-572, 2012.

[76] G. Angrisani, C. Roselli and M. Sasso, "Effect of rotational speed on the performances of a desiccant wheel," *Applied Energy,* vol. 104, pp. 268-275, 2013.

[77] W. S. S. W. R. Narayanan, "A non-adiabatic desiccant wheel: Modeling and experimental validation," *Applied Thermal Engineering,* vol. 61, pp. 178-185, 2013.

[78] J. Wrobel, P. Morgenstern and G. Schmitz, "Modeling and experimental validation of the desiccant wheel in a hybrid desiccant air conditioning system," *Applied Thermal Engineering,* vol. 51, pp. 1082-1091, 2013.

[79] S. Yamaguchi and K. Saito, "Numerical and experimental performance analysis of rotary desiccant wheels," *International Journal of Heat and Mass Transfer,* vol. 60, pp. 51-60, 2013.

[80] S. D. Antonellis, C. M. Joppolo and L. Molinaroli, "Simulation, performance analysis and optimization of desiccant wheels," *Energy and Buildings,* vol. 42, pp. 1386-1393, 2010.

[81] R. G. P. J. M. Y. H. Christian Ghiaus, "Gray-box state-space model and parameter identification of desiccant wheels," *Applied Thermal Engineering,* vol. 51, pp. 742-752, 2013.

[82] D.-Y. L. Jae Dong Chung, "Effect of desiccant isotherm on the performance of desiccant wheel," *International Journal of Refrigeration,* vol. 32, pp. 720-726, 2009.

[83] M. M. Marcello Aprile, "Grey-box modelling and in situ experimental identification of desiccant rotors," *Applied Thermal Engineering,* vol. 51, pp. 55-64, 2013.

[84] A. C.-A. J. C. F. D.-M. C.R. Ruivoa, "Interpolation procedures for the effectiveness method to account for the influence of the inlet airflow states on the desiccant wheels performance," *Energy and Buildings,* vol. 55, pp. 380-388, 2012.

[85] D.-Y. L. S. M. Y. Jae Dong Chung, "Optimization of desiccant wheel speed and area ratio of regeneration to dehumidification as a function of regeneration temperature," *Solar Energy,* vol. 83, pp. 625-635, 2009.

[86] V. V. M. H. S. D. B. Muzaffar Ali, "Development and validation of a desiccant wheel model calibrated under transient operating conditions," *Applied Thermal Engineering,* vol. 61, pp. 469-480, 2013.

[87] J. Z. X. X. Nan Wang, "Desiccant wheel thermal performance modeling for indoor humidity optimal control," *Applied Energy,* vol. 112, pp. 999-1005, 2013.

[88] S. W. M. Goldsworthy, "Limiting performance mechanisms in desiccant wheel dehumidification," *Applied Thermal Engineering,* vol. 44, pp. 21-28, 2012.

[89] E. M. V. B. N. K. G. Panaras, "Experimental validation of a simplified approach for a desiccant wheel model," *Energy and Buildings,* vol. 42, pp. 1719-1725, 2010.

[90] N. Subramanyam, M. Maiya and S. Muthy, "Application of desiccant wheel to control humidity in air conditioning systems," *Applied Thermal Engineering,* vol. 24, pp. 2777-2788, 2004.

[91] E. N., Y. H, S. A., M. A., Y. R., T. R., Y. H., M. T. and T. Y., "Performance of solar-desiccant cooling system with Silica-Gel (SiO2) and Titanium Dioxide (TiO2) desiccant wheel applied in East Asian Climates," *Solar Energy,* vol. 86, pp. 1261-1276, 2012.

[92] M. B. B. N. Pietro Finocchiaro, "Advanced solar assisted desiccant and evaporative cooling system equipped with wet heat exchangers," *Solar Energy,* vol. 86, pp. 608-618, 2012.

[93] D.-Y. L. Jae Dong Chung, "Contributions of system components and operating conditions to the performance of desiccant cooling systems," *International Journal of Refrigeration,* vol. 34, pp. 922-927, 2011.

[94] Y. Z. N. D. L. F. J. N. L. M. Ying Shenga, "Experimental analysis on performance of high temperature heatpump and desiccant wheel system," *Energy and Buildings,* vol. 66, pp. 505-513, 2013.

[95] ASHRAE, Standard 41.2-1987 (RA 92) -- Standard Methods for Laboratory Airflow Measurement, 1992.

[96] S. Garimella, A. M. Brown and A. K. Nagavarapu, "Waste heat driven absorption/vapor-compression cascade refrigeration system for megawatt scale, high-flux, low-temperature cooling," *International Journal of Refrigeration,* vol. 34, pp. 1776-1785, 2011.

[97] Y. Liang, G. Shu, H. Tian, X. Liang, H. Wei and L. Liu, "Analysis of an electricity–cooling cogeneration system based on RC–ARS combined cycle aboard ship," *Energy Conversion and Management,* vol. 76, pp. 1053-1060, 2013.

[98] A. Ouadha and Y. El-Gotni, "Integration of an ammonia-water absorption refrigeration system with a marine Diesel engine: A thermodynamic study," *Procedia Computer Science,* vol. 19, pp. 754-761, 2013.

[99] "Royal Caribbean's Oasis of the Seas Installs PV Panels," 18 January 2010. [Online]. Available: http://www.solarpowerworldonline.com/2010/01/royal-caribbeans-oasis-of-the-seas-installs-pv-panels/. [Accessed 26 Feburary 2014].

[100] A. S. 62-2001, Ventilation for Acceptable Indoor Air Quality, 2001.

[101] "Approximate fuel consumption chart," [Online]. Available: www.dieselserviceandsupply.com. [Accessed 26 Feburary 2014].

[102] W. Wu, X. Li, Y. Hwang and R. Radermacher, "Absorption Cycle modeling in TRNSYS," in *Inernational Sorption Heat Pump Conference*, College Park, Maryland, 2014.

[103] "Find the energy contained in standard battery sizes," [Online]. Available: http://www.allaboutbatteries.com/Energy-tables.html.. [Accessed 27 Feburary 2014].

[104] "Evacuated Tube Solar Collectors," Apricus Solar Hot Water, [Online]. Available: http://www.apricus.com/htmal/solar_collector.htm#Uw1v94Uz02w. [Accessed 27 Feburary 2014].

[105] W. Moomaw, P. Burgherr, G. Heath, M. Lenzen, J. Nyboer and A. Verbruggen, "Special Report on Renewable Energy Sources and Climate Change Mitigation," IPCC, 2011.

[106] G. Smestad, "The Basic Economics of Photovoltaics," 25 June 2008. [Online]. Available: http://www.solideas.com/papers/OSA_Solar_Stanford_Smestad.pdf. [Accessed 27 Feburary 2014].

[107] J. Jacobi and R. Starkweather, "Solar Photovoltaic Plant Operating and Maintenance Costs," September 2010. [Online]. Available: http://www.scottmadden.com/insight/407/Solar-Photovoltaic-Plant-Operating-and-Maintenance-Costs.html. [Accessed 27 Feburary 2014].

[108] R. Taylor, "Solar Thermal Technology & Applications," June 2006. [Online]. Available: http://apps1.eere.energy.gov/tribalenergy/pdfs/course_solar_taylor_thermal.pdf.. [Accessed 27 Feburary 2014].

[109] "Quick Guide to Solar Thermal," 2009. [Online]. Available: http://cchrc.org/docs/articles_nonCCHRC/QuickGuide2SolarThermal.pdf. [Accessed 27 Feburary 2014].

[110] D. King, "Li-ion battery prices still headed way, way down, to $180/kWh by 2020," autobloggreen, 8 November 2013. [Online]. Available: http://green.autoblog.com/2013/11/08/li-ion-battery-prices-headed--down-180-kwh/. [Accessed 27 Feburary 2014].

[111] "Chiller Water Plant Costs Estimated," May 2000. [Online]. Available: http://www.trane.com/commercial/uploads/pdf/865/ctv-trt-001-en.pdf. [Accessed 27 Feburary 2014].

[112] "Wind Power vs. Diesel Power vs. Solar Power (Comparison)," Uprise Energy, [Online]. Available: http://upriseenergy.com/blog/2012/9/15/wind-power-vs-diesel-power-vs-solar-power-comparison. [Accessed 27 Feburary 2014].

[113] ASHRAE, "Standard 62.1-2007 Ventilation for Acceptable Indoor Air Quality," American Society of Heating, Refrigerating and Air-Conditioning Engineers, Atlanta, GA, 2007.

[114] H. a. R. I. AHRI (Air-Conditioning, *AHRI Standard 550/590 Performance Rating Of Water-Chilling and Heat Pump Water-Heating Packages Using the Vapor Compression Cycle,* Arlington, VA: AHRI, 2011.

[115] ASHRAE, "ASHRAE Standard 55-2004 Thermal Environmental Conditions for Human Occupancy," American Society of Heating, Refrigerating and Air-Conditioning Engineers, Atlanta, GA, 2004.

[116] "Commercial Buildings Energy Consumption Survey (CBECS)," U.S. Energy Information Administration, 2012. [Online]. Available: http://www.eia.gov/consumption/commercial/data/2003/. [Accessed 29 March 2015].

[117] D. S. &. S. Inc., "Approximate Diesel Generator Fuel Consumption Chart," [Online]. Available: http://www.dieselserviceandsupply.com/Diesel_Fuel_Consumption.aspx. [Accessed 9 October 2014].

[118] O. Edenhofer, R. P. Madruga and Y. Sokona, "Special Report of the Intergovernmental Panel on Climate Change," Cambridge University Press, New York, U.S.A, 2012.

[119] S. e. a. Klein, "TRNSYS 17: A Transient System Simulation Program," Solar Energy Laboratory, University of Wisconsin, Madison, USA, 2010. [Online]. Available: http://sel.me.wisc.edu/trnsys. [Accessed 14 July 2015].

[120] T. Cao, H. Lee, Y. Hwang, R. Radermacher and H.-H. Chun, "Performance investigation of engine waste heat powered absorption cycle cooling system for shipboard applications," *Applied Thermal Engineering,* vol. 90, pp. 820-830, 2015.

[121] ASHRAE, "Standard 62.1-2007 Ventilation for Acceptable Air Quality," American Society of Heating, Refrigeration and Air-Conditioning Engineers, Atlanta, GA, 2007.

[122] ASHRAE, *ASHRAE Standard 55-2004 Thermal Environmental Conditions for Human Occupancy,* Atlanta, GA: ASHRAE, 2004.

[123] D. S. &. Supply, "Approximate Diesel Generator Fuel Consumption Chart," [Online]. Available: http://www.dieselserviceandsupply.com/Diesel_Fuel_Consumption.aspx. [Accessed 14 July 2015].

[124] "Second IMO GHG Study 2009, Update of the 2000 IMO GHG Study, Final report covering Phase 1 and Phase 2, IMO MEPC 59/INF.10," International Maritime, 2009.

[125] ASHRAE, "ASHRAE Guideline Measurement of Energy and Demand Savings," ASHRAE, Atlanta, GA, 2002.

[126] C. Corporation, *Prodcut Data 30MPA, MPW015-045 Liquid Chillers with Scroll Compressors and ComfortLink Controls,* Syracuse: Carrier Corporation, 2014.

[127] C. Corporation, *Prodcut Data 16LJ Single-Effect, Low Temperature Hot Water Hermetic Absorption Liquid Chiller,* Syracuse: Carrier Corporation, 2005.

[128] Weil-McLain, "80 Commercial Gas Oil Boiler Manual," [Online]. Available: http://www.weil-mclain.com/en/weil-mclain/pd-80-commercial-gas-oil-boiler/. [Accessed 8 May 2015].

[129] Danfoss, *Technical brochure – EnFusionTM PHE B3-030 brazed plate heat exchanger,* Danfoss A/S, 2008.

[130] B. H. Exchangers, "Technical Specifications for Water to Air Heat Exchangers," [Online]. Available: http://www.brazetek.com/downloads. [Accessed 8 May 2015].

[131] A. F. Products, *Shell-and-Tube Heat Exchangers 30-Series Models 218, 525, and 1000,* Newark: AMETEK, 2010.

[132] G. W. Technology, *Technical Brochure 3656/3756LH Low Head, Cast Iron, Bronze Fitted, End-Suction Pumps,* Seneca Falls: xylem, 2012.

[133] C. Onan, *Marine generator set Quiet Diesel Series 80 QD 50 Hz Model MDDCJ,* Minneapolis: Cummins Power Generation, 2007.

[134] M. A.F., T. S.R. and H. D.A., Ship Resistance and Propulsion Practical Estimation of Ship Propulsive Power, Cambridge: Cambridge University Press, 2011.

[135] T. Khatib, A. Mohamed, K. Sopian and M. Mahmoud, "Optimal sizing of building integrated hybrid PV/diesel generator system for zero load rejection for Malaysia," *Energy and Buildings,* vol. 43, pp. 3430-3435, 2011.

[136] P. Waier, C. Babbitt, T. Baker, B. Balboni and R. Bastoni, RSMeans Building Construction Cost Data, Robert S Means Coperation, 2008.

[137] D. F. Cheddie and R. Murray, "Thermo-economic modeling of a solid oxide fuel cell/gas turbine power plant with semi-direct coupling and anode recycling," *International Journal of Hydrogen Energy,* vol. 35, pp. 11208-11215, 2010.

[138] A. Baghernejad and M. Yaghoubi, "Exergoeconomic analysis and optimization of an Integrated Solar Combined Cycle System (ISCCS) using genetic algorithm," *Energy Conversion and Management,* vol. 52, pp. 2193-2203, 2011.

[139] H.-M. Henning, "Solar assisted air conditioning of buildings – an overview," *Applied Thermal Engineering,* vol. 27, pp. 1734-1749, 2007.

[140] S. &. Bunker, "World Latest Bunker Prices," [Online]. Available: http://shipandbunker.com/prices. [Accessed 26 May 2015].

[141] D. J. Eyres and G. J. Bruce, Ship Construction, Waltham, MA: Elsevier Ltd., 2012.

[142] Y. T. Kang, A. Akisawa and T. Kashiwagi, "Experimental correlation of combined heat and mass transfer for NH3–H2O falling film absorption," *International Journal of Refrigeration,* vol. 22, pp. 250-262, 1999.

[143] S. Lee, B. Koroglu and C. Park, "Experimental investigation of capillary-assisted solution wetting and heat transfer using a micro-scale, porous-layer coating on horizontal-tube, falling-film heat exchanger," *International Journal of Refrigeration,* vol. 35, pp. 1176-1187, 2012.

[144] Y. Zhao, Z. Qi, Q. Wang, J. Chen and J. Shen, "Effect of corrosion on performance of fin-and-tube heat exchangers with different fin materials," *Experimental Thermal and Fluid Science,* vol. 37, pp. 98-103, 2012.

[145] L. Fedrizzi, F. Andreatta, L. Paussa, F. Deflorian and S. Maschio, "Heat exchangers corrosion protection by using organic coatings," *Progress in Organic Coatings,* vol. 63, pp. 299-306, 2008.

[146] T. Cao, H. Lee, Y. Hwang, R. Radermacher and H.-H. Chun, "Modeling of waste heat powered energy system for container ships," *Energy,* vol. 106, pp. 408-421, 2016.

[147] N. Fumo, P. J. Mago and L. M. Chamra, "Emission operational strategy for combined cooling, heating, and power systems," *Applied Energy,* vol. 86, pp. 2344-2350, 2009.

[148] T. Erhart, U. Eicker and D. Infield, "Part load characteristics of Organic-Rankine-Cycles," in *2nd European Conference on Polygeneration*, Tarragona, Spain, 2011.

[149] prEN14825:2011, "Air conditioners, liquid chilling packages andheat pumps, with electrically driven compressors, for space heatingand cooling Testing and rating at part load conditions and calculation of seasonal performance," 2011.

[150] T. Cao, H. Lee, Y. Hwang, R. Radermacher and H.-H. Chun, "Performance investigation of engine waste heat powered absorption cycle cooling system for shipboard applications," *Applied Thermal Engineering,* vol. 90, pp. 820-830, 2015.

[151] H. &. R. I. Air-Conditioning, "Standard for Absorption Water Chilling and Water Heating Packages," AHRI, Arlington, VA, 2000.

[152] D. Farrell, "Want Green? Want an Energy-Efficient system?," Indoor Comfort Marketing, November 2012. [Online]. Available: http://www.indoorcomfortmarketing.com/want-green-want-an-energy-efficient-system.html. [Accessed 24 August 2015].

[153] L. Chao-zhen, G. Jian-ming and H. Xing-hua, "Influence of energy demands ratio on the optimal facility scheme and feasibility of BCHP system," *Energy and Builidings,* vol. 40, pp. 1876-1882, 2008.

[154] P. Waier, C. Babbitt, T. Baker, B. Balboni and R. Bastoni, RSMeans Builiding Construction Cost Data, Robert S Means Coperation, 2008.

[155] T. Khatib, A. Mohamed, K. Sopian and M. Mahmoud, "Optimal sizing of buildings integrated hybrid PV/diesel generator system for zero load rejection for Malaysia," *Energy and Buildings,* vol. 43, pp. 3430-3435, 2011.

[156] G. Shu, Y. Liang, H. Wei, H. Tian, J. Zhao and L. Liu, "A review of waste heat recovery on two-stroke IC engine aboard ship," *Renewable and Sustainable Energy Reviews,* vol. 19, pp. 385-401, 2013.

[157] T. M. Inc., *MATLAB and Global Optimization Toolbox Release 2015a,* Natick, Massachusetts.

[158] K. Deb, Multi-Objective Optimization using Evolutionary Algorithms, JOHN WILEY& SONS, LTD, 2001.

[159] N. Sahinidis, The Optimization Firm, LLC, [Online]. Available: http://www.minlp.com/.

[160] G. D. Corporation, *General Algebraic Modeling System (GAMS) Release 24.7.4,* Washington, DC, USA, 2016.

[161] Bunker, "World Latest Bunker Prices," [Online]. Available: http://shipandbunker.com/prices.

[162] A. Ben-Tal, L. E. Ghaoui and A. Nemirovski, Robust Optimization, Princeton: Princeton University Press, 2009.

[163] J. Löfberg, "Automatic robust convex programming," *Optimization Methods and Software,* vol. 27, pp. 115-129, 2012.

[164] MATLAB, "MATLAB documentation for fmincon solver," MATLAB, 2016. [Online]. Available: http://www.mathworks.com/help/optim/ug/fmincon.html.

[165] IBM, "IBM ILOG CPLEX Optimization Studio," IBM, 2016. [Online]. Available: https://www-01.ibm.com/software/websphere/products/optimization/cplex-studio-community-edition/.

[166] J. Ling, O. Kuwabara, Y. Hwang and R. Radermacher, "Experimental evaluation and performance enhancement prediction of desiccant assisted separate sensible and latent cooling air-conditioning system," *International Journal of Refrigeration,* vol. 34, pp. 946-957, 2011.

[167] I. C. Kemp, Pinch Analysis and Process Integration: A User Guide on Process Integration for the Efficient Use of Energy, Burlington, MA, USA: Elsevier Ltd., 2007.